

Titulació:

Màster Universitari en Enginyeria Aeronàutica

Alumne (nom i cognoms):

Joan Coronado Escudero

Enunciat TFG / TFM:

Economics of the exploitation of the resources in celestial bodies

Director/a del TFG / TFM:

Stéphanie Lizy-Destrez

Codirector/a del TFG / TFM:

José de Sousa

Convocatòria de lliurament del TFG / TFM:

2n Quadrimestre curs 2018-2019



PROJET DE FIN D'ETUDES

JOAN CORONADO ESCUDERO

2018 - 2019

Economics of the exploitation of the resources in celestial bodies

Internship tutor

JOSÉ DE SOUSA

Internship and University manager

STÉPHANIE LIZY-DESTREZ

Internship duration

APRIL - OCTOBER 2019

*Name and address of the
organisation*

RITM

FACULTÉ JEAN MONNET

54, BOULEVARD DESGRANGES

92330 SCEAUX

Table of contents

| | | |
|-----|---|-----------|
| 1 | Introduction | 1 |
| 2 | The economic value of asteroids | 2 |
| 2.1 | Asteroid composition | 2 |
| 2.2 | Asteroid mass estimation | 7 |
| 2.3 | Market price | 7 |
| 3 | The economic distance of asteroids | 8 |
| 3.1 | Tsiolkovsky's rocket equation | 8 |
| 3.2 | The Earth-Moon Circular Restricted Three Body Problem | 9 |
| 3.3 | Δv optimisation algorithm | 17 |
| 4 | The gravity trade model | 33 |
| 5 | Conclusions | 34 |
| | Appendices | 42 |
| A | Economic value | 42 |
| A.1 | Meteorite elemental mass fractions | 42 |
| A.2 | Elemental market price | 43 |
| A.3 | Asteroid total economic sizes | 45 |
| B | Economic distance | 46 |
| B.1 | Optimal total Δv values | 46 |
| B.2 | Most optimal trajectories | 67 |
| C | Gravity model | 87 |
| C.1 | Favourability factor values | 87 |
| D | Matlab code | 88 |
| D.1 | Asteroid_deltav_calculator | 88 |
| D.2 | Lagrange_solver_adim | 94 |
| D.3 | preliminary_solver | 94 |
| D.4 | odezero_EARTHSOI | 96 |
| D.5 | syn2scECLIPJ2000 | 97 |
| D.6 | load_kernels | 99 |

| | | |
|-----|------------------------------|----|
| D.7 | load_kernels_alt | 99 |
| D.8 | unload_kernels_alt | 99 |

1 Introduction

In recent years, interest in the resources that can be found on the Earth's neighbouring celestial bodies has been slowly but steadily rising. This situation can be attributed to a series of factors: On the one hand, the realisation that humanity's access to certain materials might be compromised in the future as reserves in our planet's crust are depleted, causing increases in price as extraction moves to less favourable sources [38]. This problem is compounded by the rapid industrialisation of the developing world, which further strains the mining industry's capacity and accelerates the transition towards lower-grade, more energy-intensive ores. And on the other hand, advances in the fields of rocketry and planetary science are the causes, respectively, of a reduction in the cost of launching equipment to space [25] and of an increased understanding of the nature of celestial objects, the pillars of a future space-based economy where resources extracted from these bodies are competitive enough with those from Earth to, at first, replace them in the construction of orbital equipment and structures and, perhaps, remove the need for mining our planet altogether.

The objective of this project is to predict the volume of the trade flow between the Earth's orbit and the asteroids in the inner Solar System; both the ones in the main asteroid belt located between Mars and Jupiter and those whose orbits bring them closer to our planet, known as Near-Earth asteroids. To do that, a gravity model will be applied between all the analysed Earth-asteroid pairs. This empirical economics model describes the trade flow between two units (countries, cities...) as a function of their economic size and their bilateral distance:

$$T_{ij} = G \frac{M_i^\alpha M_j^\beta}{D_{ij}^\zeta} \eta_{ij} \quad (1)$$

Where G , α , β and ζ are empirical parameters that depend on the pair of economic units that are being studied, M_i and M_j are their economic sizes, D_{ij} is their distance, and η_{ij} is an error parameter. For most country pairs, α , β , ζ , $\eta \approx 1$ [10].

Part of the work in this project is, then, to find a way to extrapolate these variables to the context of interplanetary space. For the economic size of the asteroids, this is accomplished in section 2. As for the economic distance, the magnitude that most closely represents the energetic consumption of a spacecraft's engine has been identified, by going directly to the fundamental physics of rockets. This is discussed in subsection 3.1.

An additional goal of this project is to study the Moon's influence in the orbital mechanics involved in a spacecraft's trajectory between the Earth and the target asteroids, with the aim to help reduce the cost of launching a mining expedition. The details of these effects will be expanded on in subsection 3.2.

And finally subsection 3.3 implements an algorithm that studies the value of the magnitude associated with cost for each of the targeted asteroids over a period of three decades, so this analysis can be applicable for years after the completion of the study.

2 The economic value of asteroids

As it has been explained on section 1, the trade flow between two economic units is proportional to their economic size. In the case of asteroids, since the only economic activity that would be carried out on them is mining, this magnitude can be defined as the market value of the materials that can be harvested from them. Therefore, to accurately assess it both their composition and their total mass has to be known. This section documents how the procedure to do that was developed.

2.1 Asteroid composition

Unlike with the geology of Earth's different regions, asteroids cannot be directly prospected to evaluate their suitability as mineral sources. The only asteroid sample material that has been directly studied is that of (25143) Itokawa, which was visited by Japan's Hayabusa space probe in November 2005. What scientists on Earth have access to, however, is the countless meteorites that have been falling on our planet for billions of years.

A great deal of the theoretical information on the characteristics of meteorites and asteroids contained in this section has been extracted from [35].

2.1.1 The study and classification of meteorites

Most of the meteorites found on Earth are of a type called chondrites, named after the silicate bubbles, or chondrules, that are found in great abundance in their structure. Their origin can be traced back to the accretion of the protoplanetary disc, which is why their bulk chemical composition resembles so much that of the totality of the Solar System. Due to many different phenomena (collisions, etc.) the temperature of chondritic asteroids can rise to a point where some of their components melt while others remain solid. This can cause a segregation of these materials into different areas of the asteroid, or even a full separation into different bodies that will now have radically different chemical composition, a process known as differentiation. The melted components (or melts) can then recrystallise at different rates in what is known as fractional recrystallisation. The result of these processes is the diversity of types of asteroid and therefore of meteorites: from those who have lost their chondritic structure in the melting process (achondrites) to asteroids that are almost purely metallic (irons) or contain differentiated metal and silicate regions (stony irons).

Going back to chondrites, their physical make-up consists of a number of structures:

- Chondrules: They have already been mentioned. Their abundance in chondrites ranges from 70% of their composition to almost none.
- Refractory inclusions: They consist of minerals rich in refractory chemical elements, whose melting point is very high, while at the same time being depleted of volatile (low melting point) elements. They are the most ancient components of chondrites.
- Metals and sulfides: Pure metals can be found as nuggets of highly refractory elements inside the refractory inclusions, and as grains of iron-nickel-cobalt inside and

at the edges of chondrules. Finally, there are also grains of iron sulfide close to the former metallic grains.

- Matrix: Formed by a variety of minerals with very small grains, it fills the gaps between the other components.



Figure 1: A piece of the Allende meteorite, a carbonaceous chondrite. Source: [57]

Since chondrites are formed by the accretion of different components at different points of the Solar System's timeline and which therefore could be found in different physical and chemical states themselves, they can be organised in different categories depending on their primary classification: by their bulk chemical composition and the proportions of the different previously mentioned structures; and their secondary classification: by the metamorphic processes that have changed them since their accretion.

Primary classification of chondrites

- Ordinary chondrites are the most common type of meteorite. They are further divided by their concentration of iron and other metals into the H (high), L (low) and LL (very low) groups.
- Enstatite chondrites are notable because of their highly-reduced chemical state, with most of their iron in metallic form and small sulphide concentrations. They are also divided by their metallic concentration into the EH (high) and EL (low) groups.
- Carbonaceous chondrites are further subdivided into many groups with little in common with each other regarding either their chemical or physical composition, from those that do not form chondrules (CI), to those with a moderate number of chondrules and a high one of refractory elements (CV and CO).
- Rumaruti (R) chondrites are highly oxidised and are about 50% composed of matrix.
- Kalangari (K) chondrites are similar to carbonaceous chondrites.
- Certain meteorites are isolates and form their own groups.

Secondary classification of chondrites

Chondrites are classified into seven groups depending on the metamorphic processes that they have experienced:

- Types 2 to 1 represent an increasing amount of water-caused metamorphoses.
- Types 3 to 6 do the same for thermal metamorphoses, with 3 being the closest to an unaltered chondrite.
- Type 7 indicates an extreme amount of shock and thermal metamorphism, to the point that the chondrites' components become undifferentiated.

By combining the two classifications, one obtains the Van Schmus chondrite classification system.

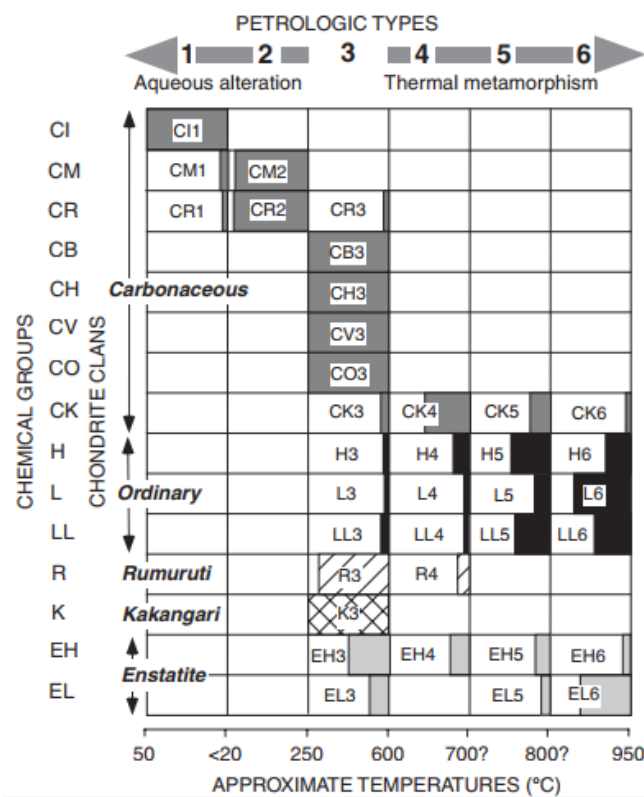


Figure 2: Chart of the Van Schmus chondrite classification system. Source: [35]

As for the non-chondritic meteorites, they can also be classified into their own families:

- Achondrites were chondrites that experienced a complete melting, losing all their internal structure and becoming undifferentiated. They are in turn classified into primitive achondrites, which occupy an intermediate stage between the two groups since they are formed after a partial melt; and magmatic achondrites, which are formed from complete melts, sometimes as a cumulate of different chondrite types, whose resulting composition is different from their parents'.
- Stony irons are formed by roughly equal amounts of metal and silicates, forming clearly separate aggregates. They are subdivided by the type of silicate that forms the rocky phase.

- Irons are majorly made of metal, most likely from the melting and complete differentiation of chondrites.

With all meteorites classified into their respective categories, their chemical composition can be defined. Annex A.1 contains table 2, sourced from [35], which displays the mass fractions of most naturally-occurring chemical elements for the different chondrite groups. In the future, to further develop the model, it would be interesting to find the elemental mass fractions for irons and stony irons which, while being much rarer, hold much more economic interest: They are much richer in valuable metals that, in theory, should also be easier to extract than the mixture of components found in chondrites.

Speaking of relative economic interest, the tabulated elemental mass fractions can be compared with those of the Earth's crust to study a meteorite group's enrichment of certain elements compared to our planet's. Figures 3 and 4 show that L chondrites were enriched with regards to Earth for metals like Fe, Ni, Cr, Co, Cu and Au; but were much poorer in rare earths.

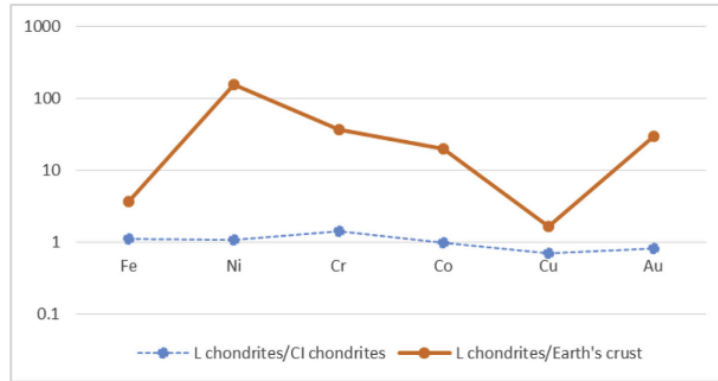


Figure 3: Enrichment/depletion of L chondrites in selected metals in comparison with CI chondrites and the Earth's crust. Source: [28]

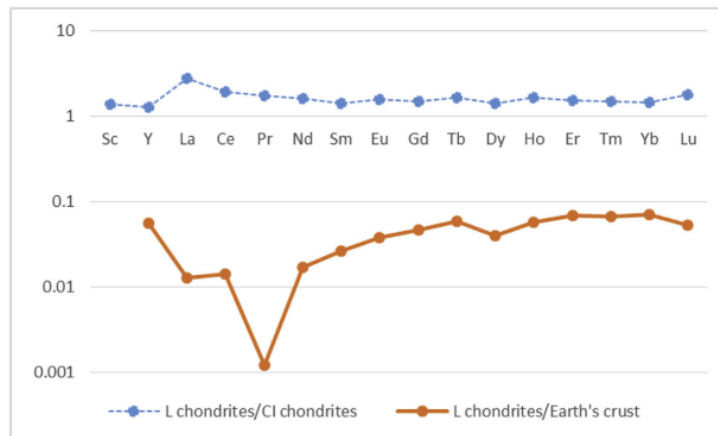


Figure 4: Enrichment/depletion of L chondrites in rare earth elements in comparison with CI chondrites and the Earth's crust. Source: [28]

2.1.2 Identifying asteroids with meteorite types

Like it was explained on the beginning of this section, asteroids cannot be directly surveyed nowadays, but they can be compared with the data that can be collected from

meteorites. The different groups of meteorites described in the previous subsection have been spectroscopically analysed in search for certain markers that would help distinguish them from one another. Once they were found, astronomers started searching for spectral coincidences in asteroids, since if they were made of the same material, the light that they reflect should feature the same radiation absorption bands. For instance, the amount of absorption in the near-infrared is an indicator of the relative percentages of minerals olivine and pyroxene in asteroids, which can be used to classify them as a certain type of chondrite [18]. Observatories have then engaged in massive surveys seeking to assign a meteorite analogue to all the known asteroids in the catalogues.

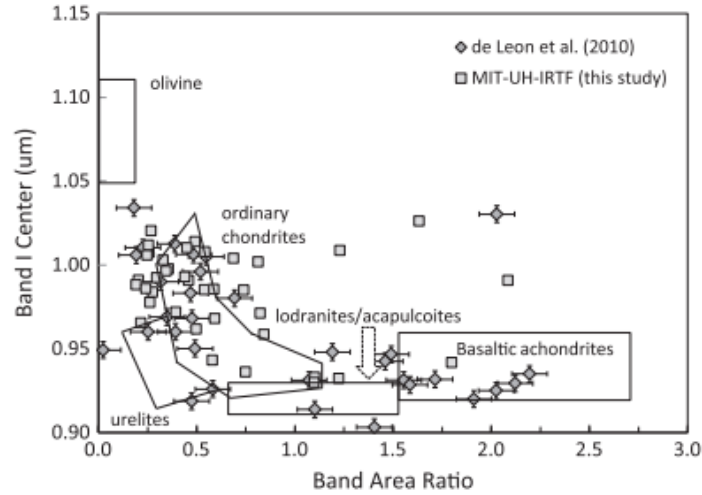


Figure 5: Classification of asteroids into meteorite types as a function of the peak of their band I Near-Infrared centre and its width. Source: [18]

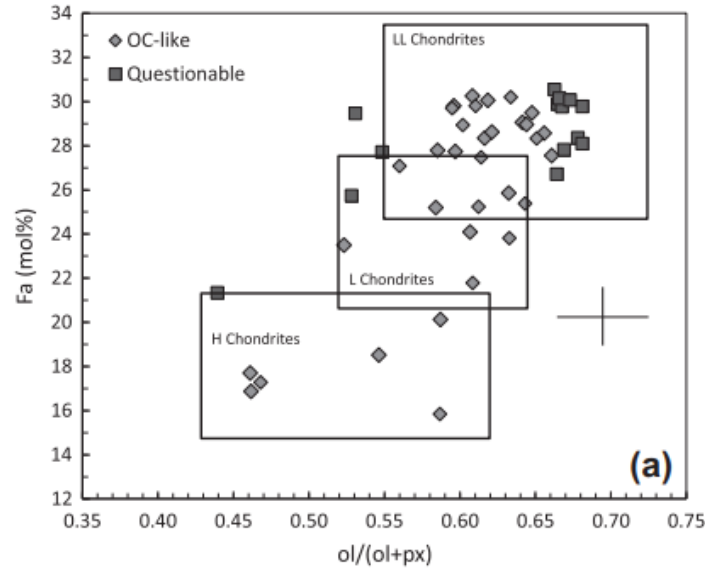


Figure 6: Classification of asteroids into ordinary chondrite classes as a function of the estimated total olivine and proportions of olivine and pyroxene. Source: [18]

2.2 Asteroid mass estimation

In order to completely characterise an asteroid for the purpose of this economic model, not only does its composition have to be known, but also its mass, to define the total amount of each element that can be found on it.

There exist several techniques that are used to evaluate an asteroid's mass [9]:

- By studying its orbital deflection during close encounters with other, more massive celestial bodies (see 3.2.4).
- By analysing the discrepancy between the predicted ephemerides of a planet and its real position and velocity, a variation of the previous point but studying the cumulative effect of a large number of bodies over one, which renders the estimations more imprecise.
- By tracking the perturbations that an asteroid creates on the orbit of a spacecraft that flies by it, a very precise technique but which has only been able to be used less than a handful of times.
- In the case of multiple-asteroid systems, by radar or optical imaging. Their mass can be derived just by observing their movement around each other using Newton's Third Law (see 3.2).

Since this project did not have access to observational equipment, all mass estimations have been obtained by means of bibliographical study, same as with the asteroids' chemical compositions. The most restricting issue during the research for the economic model has been that these two types of observations, mass and composition, are not generally undertaken simultaneously for each asteroid, resulting in a large amount of times where one of the two data points was known for it but not the other, causing it to be discarded from the list of possible targets. However, 41 asteroids have been found for which both conditions were fulfilled. A simple look at table 4, containing all these final chosen targets, confirms this situation: The sources for the two values rarely coincide in any of them.

2.3 Market price

Once the total mass of each element is defined for the targeted asteroids, by multiplying it by the elemental fractions of their corresponding meteorite type, knowing their market price per unit of mass results in the total monetary value of their resources. Table 3 in annex A.2 was elaborated using two sets of data: For common metals that are openly traded the price in the Shanghai Metals Market [54] was used as reference, using the data values of 12th June 2019, and considering the average USD/CNY exchange rate of the same day. For rarer metals, the average annual values in the U.S. Geological Survey [55]. Finally, a table 4 that combines all three sets of data to return the surveyed asteroids' economic sizes is included in annex A.3.

The only lacking part in this subsection is that it assumes that all the mass of the asteroid is available to be mined economically, which is not true. Unfortunately, no studies of the potential yield of space mining techniques for the different elements have been found that give clear answers to this question.

3 The economic distance of asteroids

On Earth, determining the distance between two economic units is a comparatively simple matter: Countries, companies and most families have fixed locations; so the relative distance between one another is constant over time. This is not true for celestial bodies, however: The Earth, together with the rest of planets and objects in the Solar System, orbits the Sun in periodic elliptical orbits. This orbital period is determined by the following formula, derived from the Third Law of Kepler and Newton's Law of Gravitation:

$$T = \sqrt{\frac{4\pi^2 a^3}{GM_s}} \quad (2)$$

Where a is the orbit's semi-major axis, $G = 6.674 \times 10^{-11} \frac{m^3}{kg \cdot s^2}$ is the universal gravitational constant, and $M_s = 1.9884 \times 10^{30}$ kg is the Sun's mass.

This means that all of the targeted asteroids will get closer and then away from the Earth at regular intervals, restricting the viable mission launch dates to short windows with months and maybe years between them. Another aspect to consider is the nature of movement on our planet and in outer space: On Earth, vehicles have to continuously spend energy to go from one place to another due to friction with the air, the ground or the sea; whereas in the void chemically-propelled spacecraft only have to carry out one-time manoeuvres to go from their current orbit to one that intercepts their target body, on which they coast without spending any more energy. This radically differs from the physics that inform the concept of economic distance used on Earth's trade gravity models.

3.1 Tsiolkovsky's rocket equation

The key to a space-based definition of economic distance, then, is found in the energy expenditure of orbital manoeuvres. During these, spacecraft spend their propellant to change the magnitude and direction of their velocity, resulting in an orbital change.

As it can be seen in 7, The velocity vector that is applied to the spacecraft during the manoeuvre is called a Δv . Its magnitude depends on the propellant mass expelled by the rocket engine according to the Tsiolkovsky equation:

$$\Delta v = v_e * \ln \frac{m_0}{m_f} \quad (3)$$

Where v_e is the propellant's exhaust velocity, which depends on the chemical or electric process used to expel it; and m_0 and m_f are the spacecraft's mass before and after the manoeuvre, respectively.

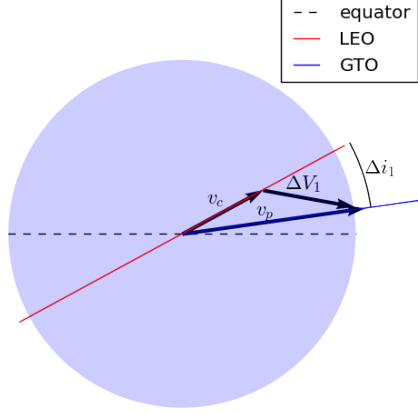


Figure 7: Vector diagram of a LEO-GTO orbital transfer. Source: [43]

This formula determines the amount of propellant that it will have to carry with itself in order to complete its mission, which when multiplied by its cost per kilogram would serve as a good metric for the expedition’s total cost, assuming reusable mining spacecraft whose construction cost can be spread over several campaigns. Like in other space probes the amount of propellant also would determine their dimensions and, in the case of a mining craft, it would restrict the amount of mineral that would be able to be harvested and carried back to Earth during an expedition, since its mass would have to be added to the spacecraft’s dry mass in both terms of the equation. Rearranging the terms of equation 3, the formula for the propellant mass m_p is derived:

$$m_p = \Delta m = m_0 - m_f = m_f * (e^{\frac{\Delta v}{v_e}} - 1) \quad (4)$$

Where in this case m_f is the spacecraft’s dry mass, and Δv represents the mission’s total. Noticing that m_f and v_e are characteristic of the spacecraft, $e^{\Delta v}$ is the only term that is mission-dependent. The exponential relationship between the amount of manoeuvring required to reach an asteroid and the necessary mass to do so becomes apparent. Considering all that has been previously said in this section, a mission’s exponential of its cumulative Δv is hypothesised to be a good metric for the costs of space transport, and a valid analogue to physical distance in the economic distance term of the gravity trade flow model.

For each of the target asteroids that were selected in section 2, then, an algorithm was created that calculates their mission Δv at each possible launch date.

3.2 The Earth-Moon Circular Restricted Three Body Problem

Before the algorithm itself can be properly described, one of its most notable features has to be explained: Its representation of an Earth-Moon system in which the action of both

of their gravitational accelerations influences the spacecraft's trajectory.

A three body problem is a physical phenomenon in which a point P with mass m is under the gravitational influence of two other punctual bodies (P_1 and P_2) called the primaries, whose masses (m_1 and m_2) are several orders of magnitude bigger than its own so their movement is not disturbed by it. Unlike the keplerian two body problem, this one cannot be solved analytically; however, adding the consideration that P_1 and P_2 describe circular orbits around their mutual barycenter, the situation can be characterised as a Circular Restricted Three Body Problem (CR3BP), which can be solved by numerical methods. This approximation is valid for systems where P_2 orbits around P_1 in a low-eccentricity ellipse, like the Moon does with the Earth.

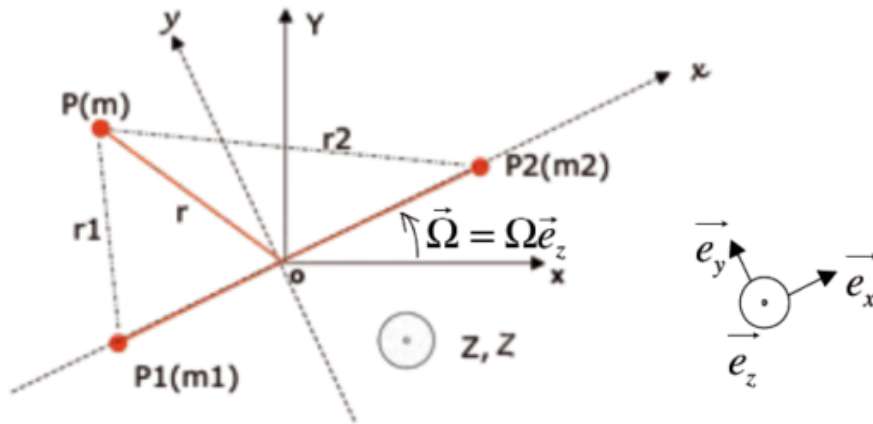


Figure 8: Diagram of a CR3BP. Source: [36]

3.2.1 Equations of movement

In the system's barycentric inertial frame (BCI), the global angular momentum is constant, and the same is true for P_1 's and P_2 's, who are also parallel to each other. This means that both bodies move on the same (O,x,y) plane.

$$\vec{H} = m_1 \vec{r}_1 \times \frac{d\vec{r}_1}{dt} + m_2 \vec{r}_2 \times \frac{d\vec{r}_2}{dt} = ctt, \text{ with } m_1 \vec{r}_1 + m_2 \vec{r}_2 = 0; \quad (5)$$

$$\vec{H}_1 = m_1 \vec{r}_1 \times \frac{d\vec{r}_1}{dt} = \frac{m_2}{m_1 + m_2} \vec{H} \quad \vec{H}_2 = m_2 \vec{r}_2 \times \frac{d\vec{r}_2}{dt} = \frac{m_1}{m_1 + m_2} \vec{H} \quad (6)$$

Where \vec{r}_1 and \vec{r}_2 are the primaries' distance to the barycenter. In the inertial system, the gravitational force that acts on P is:

$$\frac{d^2 \vec{r}}{dt^2} = -G \frac{m_1}{r_1^3} \vec{r}_1 - G \frac{m_2}{r_2^3} \vec{r}_2 \quad (7)$$

Where \vec{r}_1 and \vec{r}_2 are the particle's distances to each of the primaries.

However, since \vec{r}_1 and \vec{r}_2 move on their own, in order to fully characterise the system their movement equations would have to be taken into account, which increases its complexity and the processing power required. Therefore, in order to simplify it, the movement of P_1 and P_2 is nullified by changing to a non-inertial rotating frame around their barycenter in the angular momentum's direction such that the primaries are always on the x axis; also known in semat's literature as a synodic frame. Its angular velocity is:

$$n = \sqrt{\frac{G(m_1 + m_2)}{a_{12}^3}} \quad (8)$$

The equation of conservation of linear momentum can now be rewritten as:

$$-m_1x_1 + m_2x_2 = 0 \quad (9)$$

From which the positions of the primaries can be derived:

$$x_1 = \frac{m_2}{m_1 + m_2}a_{12} \quad x_2 = \frac{m_1}{m_1 + m_2}a_{12} = \left(1 - \frac{m_2}{m_1 + m_2}\right)a_{12} \quad (10)$$

These mass fractions can be rewritten as the CR3BP's μ parameter:

$$\mu = \frac{m_2}{m_1 + m_2} \quad \mu_1 = 1 - \mu \quad \mu_2 = \mu \quad (11)$$

The two systems of coordinates are connected by the transformation:

$$\begin{pmatrix} x \\ y \\ z \end{pmatrix}_{inertial} = \begin{pmatrix} \cos(nt) & -\sin(nt) & 0 \\ \sin(nt) & \cos(nt) & 0 \\ 0 & 0 & 1 \end{pmatrix} \begin{pmatrix} x \\ y \\ z \end{pmatrix}_{rotational} \quad (12)$$

Equation 7 can also be introduced to the new frame using the formula that connects the accelerations in inertial and a non-inertial reference systems:

$$\left. \frac{d^2\vec{r}}{dt^2} \right|_{in} = \left. \frac{d^2\vec{r}}{dt^2} \right|_{rot} + 2\vec{n} \times \left. \frac{d\vec{r}}{dt} \right|_{rot} + \vec{n} \times (\vec{n} \times \vec{r}) \quad (13)$$

Rearranging and developing the previous terms, the particle's equations of movement in the rotational frame of reference can then be described as [62]:

$$\begin{pmatrix} \ddot{x} \\ \ddot{y} \\ \ddot{z} \end{pmatrix} = \begin{pmatrix} n^2x + 2n\dot{y} - G \left(\frac{m_1}{r_1^3}(x + x_1) + \frac{m_2}{r_2^3}(x - x_2) \right) \\ n^2y - 2n\dot{x} - G \left(\frac{m_1}{r_1^3}y + \frac{m_2}{r_2^3}y \right) \\ -G \left(\frac{m_1}{r_1^3}z + \frac{m_2}{r_2^3}z \right) \end{pmatrix}, \quad (14)$$

with $r_1 = \sqrt{(x + x_1)^2 + y^2 + z^2}$ and $r_2 = \sqrt{(x - x_2)^2 + y^2 + z^2}$

These are the equations that the algorithm integrates to calculate the spacecraft's trajectory in the Earth-Moon system.

3.2.2 The integral of motion and Jacobi's constant

The expression for the components of the acceleration in the rotating system, equation 14, can be generalised as the sum of the gradient of a "pseudo-potential" and a velocity term:

$$\left. \frac{d^2 \vec{r}}{dt^2} \right|_{rot} = -\vec{\nabla} U - 2\vec{n} \times \left. \frac{d\vec{r}}{dt} \right|_{rot}, \quad \text{with } U = -G \left(\frac{m_1}{r_1} + \frac{m_2}{r_2} \right) - \frac{1}{2}n^2(x^2 + y^2) \quad (15)$$

U is called a pseudo-potential because it combines the gravitational potential with a centrifugal term, so P 's motion cannot be purely defined by an exchange between kinetic and potential energy. However, U still is a good measure of the system's total energy: Projecting each of the acceleration terms on the non-inertial velocity and adding them [36] results in the expression:

$$\dot{x}\ddot{x} + \dot{y}\ddot{y} + \dot{z}\ddot{z} = -U_x\dot{x} - U_y\dot{y} - U_z\dot{z} = -\frac{dU}{dt} \quad (16)$$

Where the subscript indicates each derivative of the pseudo-potential. Finally, this expression can be integrated into:

$$\dot{x}^2 + \dot{y}^2 + \dot{z}^2 = V^2 = -2U - C_J \rightarrow C_J = n^2(x^2 + y^2) + 2G \left(\frac{m_1}{r_1} + \frac{m_2}{r_2} \right) - (\dot{x}^2 + \dot{y}^2 + \dot{z}^2) \quad (17)$$

C_J is conserved along the particle's motion in the system and is called Jacobi's constant. As such, it is a function of the particle's initial conditions of position and velocity. This has important consequences for its possible trajectories: Due to the energy exchange between the kinetic and pseudo-potential terms, P 's velocity will be zero at all points that fulfil the condition:

$$2U + C_J = 0 \quad (18)$$

The ensemble of all those points is called a Hill surface or null-velocity surface and it limits the areas of the three-body system that are reachable by the particle depending on its initial energy level.

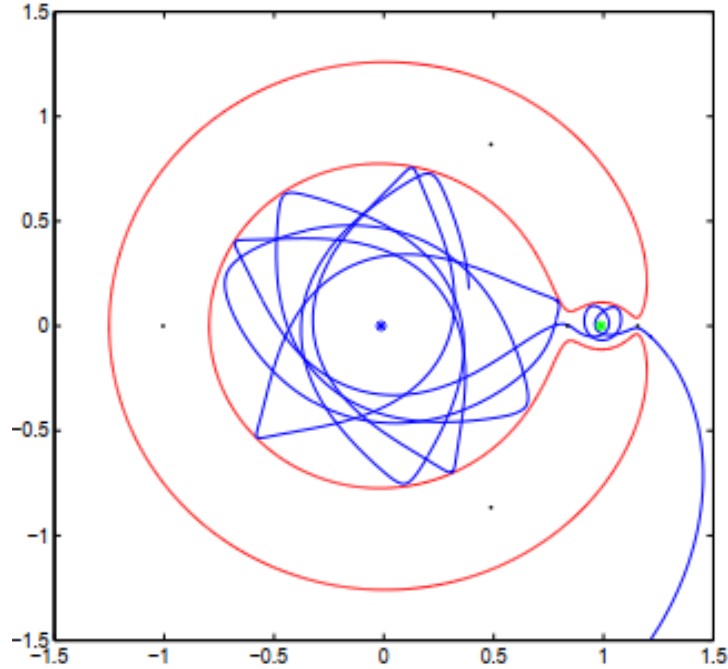


Figure 9: Trajectory of a particle in the Earth-Moon system's x-y plane. Its Hill surfaces are shown in red, and the Lagrange points are also highlighted. Distances in multiples of the Earth-Moon semi-major axis. Source: [37]

3.2.3 Lagrange points

In every CR3BP there are 5 points, known as its Lagrange points, in which the gravitational and the centrifugal forces are balanced against each other, which results in a null gradient of the pseudo-potential.

$$\vec{\nabla}U = 0 \quad (19)$$

Their positions are as follows:

- L_1 and L_2 are located on the axis of the primaries, close to P_2 : The first one on the side between P_1 and P_2 , and the second one on the opposite side of P_2 .
- L_3 is also located on the same axis, but behind P_1 , and at the same distance as P_2 .
- L_4 and L_5 form an equilateral triangle with the primaries, each one located on one side of the axis of the primaries, symmetrically to each other.

In theory, a particle at rest (in the rotating frame of reference) at any of these points would experience no net forces and as such should stay motionless in its vicinity. This is not true, however, due to the nature of this equilibrium: L_1 , L_2 and L_3 are located on the non-inertial x-axis in which, while the forces are in equilibrium, the forces in the y axis are just null. This causes that, if P moves even slightly from the point, it will start experiencing this perpendicular component, destabilising it and causing it to fall out of orbit over time. L_4 and L_5 , on the other hand, are geometrically stabilised by the equilibrium between the centrifugal and gravitational forces in all directions: The Coriolis force will keep P around these points after a perturbation. All five points represent a flattening of the pseudo-potential field, however the unstable ones are located at the top of a slope whereas the stable ones are at the bottom of a well.

Perturbations in the unstable equilibrium points take a long time to propagate, however, and spacecraft can remain in orbit around them with just some periodic station keeping. These orbits can be grouped into a series of families [21] [36]:

- Lyapunov orbits lie in a plane between the two primaries. As such, they are classified in two families: planar and vertical, depending on whether they are contained in the same orbital plane as the primaries or perpendicularly to it.
- Lissajous orbits are quasi-periodic orbits that are not contained in a plane of the primaries, instead forming 2-D Lissajous curved shapes. They connect the Lyapunov orbits of the same energy level.
- Transit orbits go directly through the Lagrange points to either the interior or the exterior of the system. In their trajectory, they have to cross a Lyapunov orbit.

All of these orbits are grouped in stable and unstable tube-shaped manifolds: The former remain in orbit around the libration points while the latter end up leaving their orbit. In fact, it would be more precise to call the L_1 - L_3 points meta-stable. Station keeping ensures that spacecraft orbiting them remain in their stable manifolds against the effect of perturbations, which if nothing is done to counteract them can cause a switch to an unstable manifold that would cause the spacecraft to escape from the point. However, these unstable manifolds can also be useful: Since they connect the Lagrange points between each other, and link to other zones in the Earth-Moon system or beyond, by taking them the spacecraft can travel to these areas at a very low energy cost.

A large part of semat's code, whose purpose is explained in 3.3.1, is dedicated to calculating these orbits' dynamics.

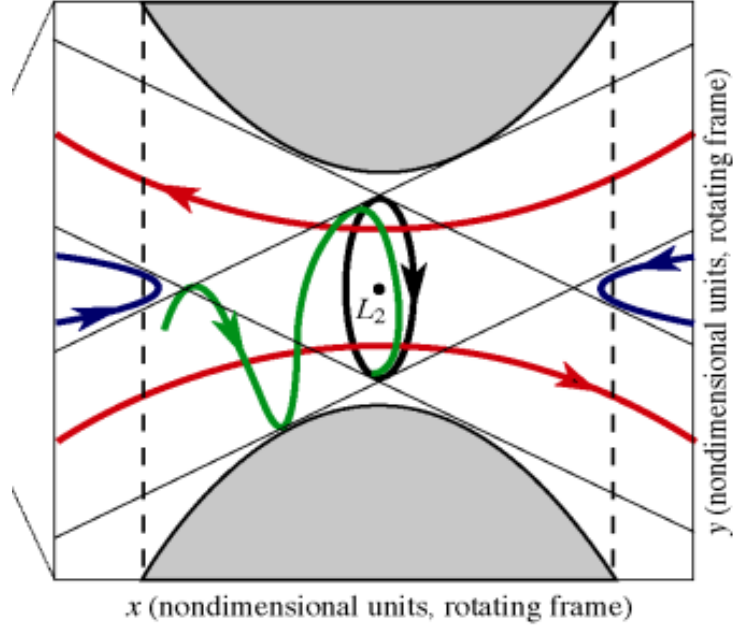


Figure 10: Different types of orbits about the L_2 Lagrange point: planar Lyapunov (blue), vertical Lyapunov (black), Lissajous (green), transit (red). Source: [36]

3.2.4 Gravity assists

In a CR3BP, the definition of Jacobi's constant can be written in the adimensionalised inertial system as:

$$\dot{x}^2 + \dot{y}^2 + \dot{z}^2 - 2(x\dot{y} - \dot{x}y) = 2\left(\frac{\mu_1}{r_1} + \frac{\mu_2}{r_2}\right) - C_J \quad (20)$$

Where the position parameters have been divided by the distance between the primaries and the velocities, by the latter's product with their mean angular velocity.

Now, considering a body that follows a keplerian orbit inside the system, close to P_1 (so $r_1 \simeq r$ and $\frac{1}{r_2} \simeq 0$). It will have to follow these criteria:

- Conservation of energy:

$$v^2 = \dot{x}^2 + \dot{y}^2 + \dot{z}^2 = \frac{2}{r} - \frac{1}{a} \quad (21)$$

- Projection of the angular momentum:

$$\dot{x}y - x\dot{y} = \sqrt{a(1-e^2)}\cos i \quad (22)$$

By combining the three previous formulas and adding the criteria of proximity to P_1 , the definition of Tisserand's constant is obtained:

$$\frac{1}{a} + 2\sqrt{a(1-e^2)}\cos i = \text{constant} \quad (23)$$

This constant suggests that a celestial body that flies by another much more massive one will have its orbital parameters modified. It is the cornerstone of the concept of gravity assists.

In these manoeuvres, a spacecraft enters a planet's sphere of influence in a hyperbolic trajectory with an initial velocity \vec{v}_{∞}^- , the result of subtracting its velocity with regards to the sun to that of the planet's:

$$\vec{v}_{\infty}^- = \vec{v}_{sc/sun} - \vec{v}_{planet/sun} \quad (24)$$

A planet's sphere of influence (SOI) is the volume around which it acts as the main gravitational attractor. To put it another way, when a third body enters it, its orbit goes from being defined by a keplerian two-body problem around the Sun to a three-body problem that fulfils the conditions for the application of Tisserand's constant. The algorithm uses the following definition for its radius:

$$r_{SOI} = a \left(\frac{m}{M} \right)^{2/5} \quad (25)$$

Where a is the semi-major axis of the planet's orbit around the Sun, m is its mass and M is the Sun's.

After the spacecraft performs its hyperbole around the planet, it will leave its SOI with a planetocentric velocity \vec{v}_{∞}^+ , with the same module as when it entered but different direction due to the planet's deflection. When added to the planet's heliocentric velocity, results in a different spacecraft heliocentric velocity than the one before the approach.

Gravity assists reduce the necessary Δv for interplanetary missions and allow for faster travel between celestial bodies. Their efficiency will depend on the planet's mass, the radius of the fly-by hyperbole's periapsis and the angle with which the spacecraft intercepts it. Flying behind the planet increases the spacecraft's heliocentric velocity, while flying in front of the planet reduces it.

This subsection has described the gravity assist procedure in terms of orbits around the Sun, but the Earth-Moon system can also be used to carry out this manoeuvre. If a spacecraft flies close enough to the Moon, the conditions for the application of Tisserand's constant are fulfilled and the satellite deflects its velocity from the geocentric frame of reference. This effect is used in the algorithm to increase its escape velocity and orient

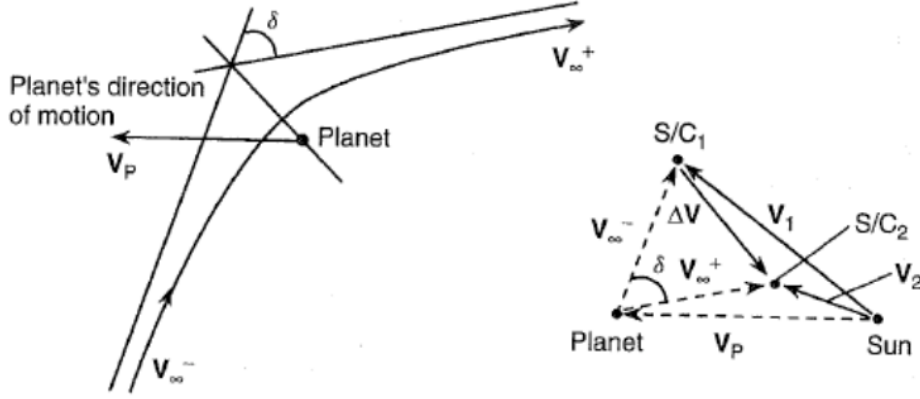


Figure 11: Diagram of a planetary fly-by and its associated velocity change. Source: [36]

it in a more favourable direction for the interception of the target asteroids, reducing the mission's total Δv and therefore decreasing the economic distance between them and the Earth-Moon system.

3.3 Δv optimisation algorithm

In this subsection, a step by step commentary of the Δv optimiser for trajectories between the Earth-Moon system and the targeted asteroids is provided, detailing its objectives, its structure and the decision process that led to its current design, including flaws in previous approaches and issues that are still open to improvement.

At its most general level, the algorithm aims to find the most favourable conditions under which resource mining expeditions to the different target asteroids would be launched during the next 30 years. For each day between 1st January 2020 and 1st January 2050, the algorithm finds the most optimal combination of conditions to minimise the total Δv of an expedition launched that day. The results will show both the most favourable launch windows for each asteroid, and they will provide a means to compare their reachability in order to find the most favourable targets.

The algorithm was developed in the MATLAB programming environment, with the aid of the SEMAT toolkit. This library has been developed by Supaero for use in orbital calculations, primarily in the Earth-Moon system. In order to run some of its routines, it also uses kernels from NASA's SPICE toolkit. Their design and functionalities will now be explained:

3.3.1 The SEMAT toolkit

In the computer's hard drive the library's functions' files are organised in a series of folders, depending on their general purpose. These are:

- C: Contains the files of a number of functions that have been coded in the C programming language, as well as those of their headers.

- `coc`: Contains the functions that transform a spacecraft's state vector from its original frame of reference to another, from generic changes to those of specific frames: The Earth-Moon synodic frame, The Earth-Moon barycentric Inertial frame (BCI), the Earth-centric inertial frame (ECI)... To perform these tasks it also contains functions that calculate both bodies' position and velocity at certain instants.
- `computation`: Includes different kinds of functions necessary for orbital analysis: from more changes of frame of reference, to Hohmann transfer calculations, obtaining an orbit's elements from its state space and vice versa... As well as more general tools for matrix and vectorial calculus.
- `data`: Contains a series of .mat repositories that can be read by MATLAB, with data related to a number of orbits around the Earth-Moon Lagrange points (see 3.2.3).
- `diffcorr`: Includes various differential corrections for the different types of orbits mentioned before.
- `init`: Starts the `semat` toolbox in MATLAB, loading its folders and running a series of processes that are described in more detail later.
- `inpolyhedron`: An external function that tests if a point is in a 3D triangular surface.
- `lib`: Includes a series of external libraries that are necessary to run `semat`.
- `mex`: Contains the MATLAB-compatible files written in C, also known as MEX files, of a Runge-Kutta 7/8 integrator of the spacecraft's state vector using the Earth-Moon 3-body problem movement equations, which were explained in 3.2.1.
- `mice_kernels`: Includes SPICE's data files, known as kernels.
- `nro_script_sara`: Contains the scripts that simulate a Near-Rectilinear Orbit (NRO) around the Moon.
- `ode`: Contains the files for another two integrators of the Earth-Moon 3-body problem vector field: One with just the first-order derivatives and another one that adds a state transition matrix with an additional 36 terms for a higher integration precision.
- `plot`: Includes a series of functions with plots that are of interest in the study of orbits in the Earth-Moon system, like trajectories over the two bodies, orbital manifolds, etc.
- `pyTest`: Solves the position of the L_1 , L_2 and L_3 Lagrange points via polynomial equations.
- `rdv`: Contains functions that change the frame of reference to a Lunar-centric one and integrate the 3 body problem in it.
- `Relative Dynamics EB`: Includes functions that study the relative motion of two bodies orbiting in the Earth-Moon system, called the chaser and the target.
- `richardson`: Contains the functions that calculate a third-order approximation of the state vector of the initial conditions for different types of orbits.

- scripts: Includes different scripts that test the rest of the toolkit's functions.
- scripts EB: Similar to the previous folder.
- Third Party: Contains more third party modules that add further capabilities to the toolbox. The new external functions used by the algorithm have been added here.

semat was provided by the university tutor, including a flowchart that details the work of the toolkit's main functions. After becoming familiar with how it works, the algorithm's modules that were already written were integrated as much as possible with it. Sometimes this integration is not as efficient as possible and in other cases the existing functions were preferred over semat's even when the latter offered more precise results, something that should be changed later in the project. This will be further discussed in 3.3.4.

3.3.2 The SPICE toolkit

SPICE is a toolkit developed by NASA's Navigation and Ancillary Information Facility (NAIF) for use by the space scientific community in the modelling and planning of missions, including the agency's own. Its main component are a series of data files called *kernels* that contain the following information, compiled from the most reliable sources available:

- Spacecraft, planet, satellite and asteroid ephemerides.
- Physical, dynamical and cartographic properties of these bodies.
- Specifications of scientific instruments and spacecraft structures.
- Space event information.
- Frames of reference used in space missions, including for positioning instruments.
- Time transformations between different measurement systems.

The kernels are regularly updated, and users can create their own and release them for use by the rest of the community.

The second piece of the toolkit are the functions that access the kernels. These can be added to the user's programmes, and for increased flexibility the entire toolbox is available in a variety of programming environments and languages. This algorithm uses *mice*, SPICE's MATLAB implementation. A detailed explanation of the routines it runs and the tasks they carry out in the programme is provided in the next sections.

SPICE is available for free on its official webpage [41], which also features extensive documentation and a considerable amount of tutorials for all aspects of the toolkit, usually in sections especially dedicated to each of its different language implementations. Programming examples are also provided with the code.

3.3.3 Referenced algorithms

The algorithm's operation is based on those proposed in [4] and [23]. Both are feasibility studies on the exploration of Near-Earth Asteroids in both unmanned and man-rated missions: Their objective was finding which of these asteroids had the most favourable Δv . To do that, they iterated over different values of a spacecraft launch's initial conditions until finding the one that yielded the lowest Δv at each possible launch date. The studied initial parameters were:

- Launch dates: Both the total studied time-span and the time step between each one.
- Flight time: Both the mission's minimum and maximum possible flight times and the studied time step, for the departure and return trips.
- Stay time at the asteroid: Same considerations as the previous variable.
- Total mission time: Limited to an amount considered acceptable for manned interplanetary missions.
- Hyperbolic excess velocity: The minimum and maximum v_∞ that the launch vehicle is able to provide, as defined by the parameter $C_3 = v_\infty^2$.
- Maximum reentry velocity: Limited due to structural considerations of the vehicle.

The approach taken by the algorithm in [4] to calculate the mission's Δv is as follows: First, for each launch date and flight time, it calculates their ephemerides at the start and end of the departing trip and solves its corresponding Lambert's problem. Its solution are the velocities that the spacecraft should have at the start of the trip, when it leaves the planet's position, and at the end when it intercepts the target asteroid, in order to describe an heliocentric elliptical orbit that connects these two points in the desired flight time. Since the celestial bodies' velocities are also known, the necessary departure and arrival Δv values can be easily obtained:

$$\Delta v_{DEP} = v_\infty = \|\vec{v}_1 - \vec{v}_{EARTH,DEP}\| \quad (26)$$

$$\Delta v_{ARR} = \|\vec{v}_{AST,ARR} - \vec{v}_2\| \quad (27)$$

Where \vec{v}_1 and \vec{v}_2 are the solutions to Lambert's problem, $\vec{v}_{EARTH,DEP}$ is Earth's velocity at departure and $\vec{v}_{AST,ARR}$ is the asteroid's at arrival.

From there, the algorithm would calculate if the calculated v_∞ was within the acceptable bounds. If so, it would then calculate the return trip's Δv for all possible combinations of stay time at the asteroid and return flight time. The restrictions at these stage are whether the sum of both flight times and the stay time exceeds the maximum possible mission time, and whether after returning to the Earth's SOI on a hyperbolic Earth-centric orbit its velocity at the perigee exceeds the maximum reentry velocity. Finally, if the mission is

viable, the algorithm adds all the impulses to calculate the mission's total Δv , iterating over all possible parameters for each launch date until finding the combination that yields the minimum one.

The algorithm shown in [23] is an attempt to improve the previous one by introducing the effects of a Lunar fly-by in the spacecraft's initial trajectory, as seen in 3.2.4. In this case, the C_3 parameter is not provided as a function of the launch vehicle's capabilities, instead v_∞ is defined by the initial conditions: The spacecraft starts in a circular LEO orbit with an altitude of 185 km. At launch, its engines send it on a Lunar fly-by trajectory via a Hohmann transfer, with an initial Δv :

$$\Delta v_{LEO} = \sqrt{2Gm_e \left(\frac{2}{r_{LEO}} - \frac{1}{a_M} \right)} - \sqrt{\frac{Gm_e}{r_{LEO}}} = 3.1352 \text{ km/s} \quad (28)$$

Where m_e is the Earth's mass, r_{LEO} is the initial orbital radius and a_M is the Earth-Moon semi-major axis of the Hohmann transfer. With the appropriate angle between the spacecraft and the Moon, that the authors quantify at between 110° and 125° , the spacecraft gets close enough to the Moon for it to perform a gravity assist, which launches it in a hyperbolic geocentric trajectory outside of the planet's SOI, whose radius it reaches with a C_3 parameter of:

$$C_3 = 2E = -\frac{Gm_e}{a_M} = -2.3090 \text{ km}^2/\text{s}^2 \quad (29)$$

Using the Earth's ephemerides, the spacecraft's position and velocity are then transformed to a heliocentric frame of reference, and act as the initial state of the departure Lambert problem. The rest of the process is carried out as in [4] from that point forward.

The differences between the approach taken by those algorithms and the one created for this project are the following:

- The cited papers analysed the feasibility of reaching the NEAs that they studied using a defined spacecraft, whose performance capabilities (engine specific impulse, dry mass...) were based on those known at the time of their writing for the Orion Multi-Purpose Crewed Vehicle. There are no feasibility considerations in terms of maximum possible Δv or flight time for this algorithm. This is due to the fact that the values used in those papers were too limiting, since they had to consider the restrictions involving manned missions, while this is not the aim of this project.
- The cited papers calculated the total Δv for a return trip mission to the studied NEAs, whereas this algorithm only considers the departure trip. Even though that might seem limiting, the reasons are due to the differences in mission purposes that have been previously described. Those papers expected a relatively short stay on



Figure 12: The Orion spacecraft. Its capabilities were used to constrain the cited algorithms. Source: [58]

the asteroids before returning to Earth due to the nature of manned exploratory missions, whereas mining expeditions would require a long time to extract all the desired resources before going back. However, since during the study of the literature no conclusive value of the length of that stay has been found, it was decided that it was preferable not to use a speculative value that might greatly differ from that of reality, rendering this study useless. If a reliable time-frame can be found, the return part of the algorithm could be implemented. However, it should be considered whether the spacecraft would re-enter the Earth's atmosphere or if instead would aim to return to its starting position, maybe slowing it down via aerobraking as it has been suggested in [56] for the capture of asteroids.

There are also differences in their implementation that will be discussed in the description of the corresponding sections of the code.

3.3.4 Description of the code

All functions that were developed for this project can be found in annex D.

First of all, the code clears all the variables in the workspace and all the commands and messages in the console in order to avoid possible conflicting data from previous scripts when running the algorithm anew. Then, it starts the *semat* environment by calling the *init* function. This loads different types of data that *semat* needs to work:

- Pre-defined coordinate systems.
- Different frameworks, aimed at varying types of mission.
- Two dynamic models: the CR3BP that has already been discussed in 3.2 and the Quasi-Bicircular model, which adds a fourth body to the system.
- Types of manifold for the computation of orbits around the Lagrange points (see 3.2.3).

- Environment data, which ranges from definitions for certain physical constants and ephemeris time values to physical properties of the Earth, the Sun and the Moon.
- Options for selecting the different types of orbit discussed in 3.2.3.
- Instructions to call different plotting scripts, as well as whether to show the depicted units in dimensional or adimensional form.
- Selector for using the environment's routines in Matlab or MEX form (see 3.3.1).

The function then selects the user's specific preferences among those categories for the problem that they want to study and stores them in a struct file. For this algorithm the default values were picked, resulting in the eponymous data structure.

However, *semat* does not use the SPICE kernels (discussed in 3.3.2) by default. To do so, the *load_kernels* function is called, which adds the ones stored in the *mice_kernels* folder to the algorithm's project, making them available for use, and modifies the *default* struct to reflect this change.

Next, the environment for the study of the Earth-Moon three-body problem is loaded by calling the *init_CR3BP* function, which adds the *cr3bp* struct to the workspace. It contains relevant physical parameters for calculations related to the problem in a way that is easy to reference and to export to nested functions. However, since typing their entire name is a bit inconvenient for some of them, especially those that are repeatedly used in the algorithm, the following step was to directly add them to the workspace with shorter names. For example, the Earth's mass can be called by *cr3bp.m1.M* or just *m_1*. In this section certain magnitudes derived from these are also calculated, like the mean angular velocity of the primaries around their common barycenter or their position in the synodic frame of reference. Finally, the vector with all the studied launch dates is introduced: It goes in 6-day increments from 0:00:00 1st January 2020 to 0:00:00 1st January 2050 in the Coordinated Universal Time (UTC) time scale. The initial date was selected to provide relevant data immediately from the deposition of this document, while the final one is the same as in the case studies presented in [4] and [23]. The time step is also the same as in the referenced algorithms. The dates are written in their Julian Date format due to its greater ease of numerical manipulation. However, when carrying out orbital calculations these are transformed into their corresponding Barycentric Dynamical Time (TDB) value, since that is the time scale used by the SPICE toolkit.

Afterwards, the position of the Earth-Moon system's Lagrange points is determined by the *Lagrange_solver_adim* function. While these values can already be found in the *cr3bp* struct, this function had already been written before receiving the *semat* toolbox, so since the work was already done in its runtime is very short it was kept. *Lagrange_solver_adim* takes the the Earth-Moon μ_1 and μ_2 parameters and introduces them in the formulas for the components of the gradient of the pseudo-potential defined in 3.2.2. A non-linear solver then finds the values of the (x,y) coordinates in which that gradient is zero (the definition of a Lagrange point, per equation 19). Finally, the null values in the z coordinate are added and the result is sent back to the main function as a 5×3 matrix. Note that the values of the Lagrange point coordinates, like those of the primaries that were obtained

in the previous section, are given in their adimensional form due to the greater ease of calculating the CR3BP problem in that way, as it will be seen in the following paragraphs.

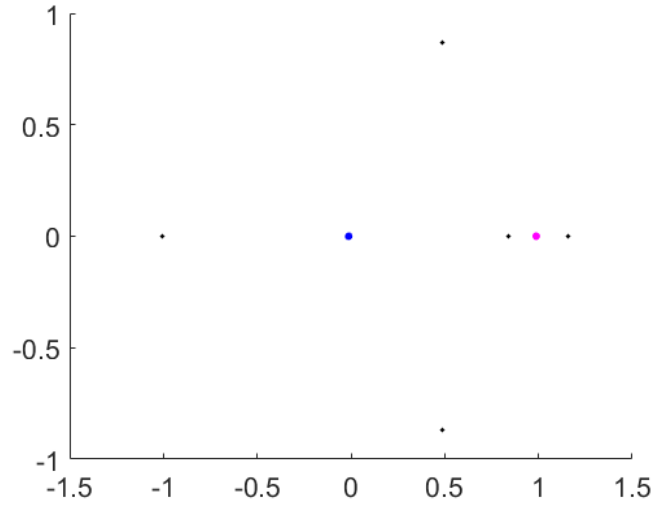


Figure 13: Lagrange points of the Earth-Moon system obtained by *Lagrange_solver_adim* in black, with the two primaries in blue and magenta respectively

Later, the target asteroid's orbital parameters are added to the workspace by inputting its official number and name. These are extracted from the Jet Propulsion Laboratory's Small-Body Database Browser [26]. Their ephemerides have been downloaded from HORIZONS upon request in the form of the custom *wld86210.15* and *wld1156302.15* SPICE kernel files, which have then been added to *load_kernels* so that they are available to mice, since the ones that were previously in the *mice_kernels* folder did not contain these asteroid ephemerides. These files have also been deposited there. This approach increases the precision of the computed position and velocity of the targets, since their future ephemerides are calculated by integrating the Solar System's n-body problem instead of just extrapolating from the current ones over time while assuming they follow unperturbed keplerian orbits around the Sun, the approach that the algorithm previously used.

| Orbital Elements at Epoch 2458600.5 (2019-Apr-27.0) TDB Reference: JPL 783 (heliocentric ecliptic J2000) | | | |
|---|--|-----------------------|-------|
| Element | Value | Uncertainty (1-sigma) | Units |
| e | .533234731246704 | 2.4281e-08 | |
| a | 2.664145333304944 | 2.3786e-09 | au |
| q | 1.243530512497922 | 6.4758e-08 | au |
| i | 26.68761298568435 | 4.0549e-06 | deg |
| node | 215.5575046748637 | 7.1897e-06 | deg |
| peri | 132.3963555750316 | 7.6041e-06 | deg |
| M | 274.1561977877303 | 2.3105e-06 | deg |
| t _p | 2458979.240493073043 (2020-May-09.74049307) | 1.0548e-05 | TDB |
| period | 1588.310093361722 | 2.1271e-06 | d |
| | 4.35 | 5.824e-09 | yr |
| n | .2266559921167822 | 3.0354e-10 | deg/d |
| Q | 4.084760154111966 | 3.6469e-09 | au |

Figure 14: Orbital elements of (1036) Ganymed. Source: [26]

Next, the vectors of the different optimisation parameters are selected. Like with the referenced algorithms, the outward flight time is one of the chosen ones. In their case, the other variables were also time-based, which were then constrained by the limitations of manned space missions and the capsule's characteristics. This algorithm, instead, attempts to achieve the lowest possible mission Δv by finding the most optimal initial flight conditions via the use of a Lunar gravity assist. Instead of regarding the launch velocity as a constrain like in [4] or considering it fixed like in [23], the algorithm studies different values of:

- The initial Δv norm, Δv_0 (variable *delta_v_0*): The spacecraft starts at the L_1 Lagrange point, in a static position from the synodic frame of reference. The initial kick-off is therefore necessary to set it in a escape orbit from the Earth-Moon system.
- The initial Δv deflection angle, α_0 (variable *alpha_0*): This will affect the direction in which the spacecraft's velocity is deflected.

This approach attempts to improve the results of the gravity assist presented in [23] by taking more advantage of its possibilities: In that algorithm the spacecraft's position and velocity were restricted to the Earth-Moon orbital plane until it left the system's SOI, at which point the Lambert problem's solution resulted in a Δv that might involve a big change of orbital plane, one of the most costly manoeuvres. By heading towards the Moon at an angle, the satellite sends the spacecraft out of plane at no extra energetic cost, potentially reducing the magnitude of the SOI impulse and by consequence the mission's total Δv .

To explain how that angle is defined, first of all it was ensured that the spacecraft would never be sent in a collision course with the Moon by the initial Δv , while getting it close enough to the satellite for the gravity assist to be effective. To achieve that, the initial Δv should be tangential to the Moon, and so it was divided into a normal and a tangential component by the angle θ_{L1M} (variable *theta_L1M*), the angle of a right triangle whose vertices are the L_1 Lagrange point, the centre of the Moon and a perpendicular point on the Moon's surface:

$$\begin{pmatrix} v_{n0} \\ v_{t0} \end{pmatrix} = \begin{pmatrix} \Delta v_0 \cos(\theta_{L1M}) \\ \Delta v_0 \sin(\theta_{L1M}) \end{pmatrix}, \text{ with } \theta_{L1M} = \arctan\left(\frac{R_M/a_{EM}}{x_M - x_{L1}}\right) = 0.029 \text{ rad} \quad (30)$$

Where R_M is the Moon's radius, a_{EM} is the Earth-Moon semi-major axis and x_M and x_{L1} are the x coordinates of its centre and the L_1 Lagrange point in the synodic frame of reference.

The normal component is equivalent to the x component in the synodic frame of reference, while the tangential one is the sum of the y and z components. The initial Δv deflection angle, α_0 , is added in order to separate them. This angle is defined by projecting the Moon on the y-z synodic plane, with the origin point at its centre. Its null angle is that of a vector aiming in the positive z direction, and it increases in value clockwise. Thus,

the y and z components of the initial velocity are defined as:

$$\begin{pmatrix} v_{y0} \\ v_{z0} \end{pmatrix} = \begin{pmatrix} -v_{t0} \sin(\alpha_0) \\ v_{t0} \cos(\alpha_0) \end{pmatrix}, \text{ with } \alpha_0 = [0, 2\pi] \text{ rad} \quad (31)$$

In practice, the only values of α_0 that are of interest to the project are between 0 and π rad, since those between π and 2π rad cause the spacecraft to do a fly-by in front of the Moon, losing velocity in the process. The components of the initial Δv can then be written as a function of the optimisation parameters:

$$\begin{pmatrix} v_{x0} \\ v_{y0} \\ v_{z0} \end{pmatrix} = \begin{pmatrix} \Delta v_0 \cos(\theta_{L1M}) \\ -\Delta v_0 \sin(\theta_{L1M}) \sin(\alpha_0) \\ \Delta v_0 \sin(\theta_{L1M}) \cos(\alpha_0) \end{pmatrix} \quad (32)$$

However, the magnitude of these variables has to be defined. A problem that arose during the development of the algorithm was the difficulty of properly calibrating these for each target asteroid. A very wide margin of initial Δv caused its total run-time to skyrocket to more than a day, while narrowing it down too much diminished the maximum possible degree of optimisation. And even when a reasonable margin width and Δv step size had been found, its minimum value was also dependent on each target's orbital characteristics: Those with large semi-major axes or high inclination angles had a higher minimum possible Δv than NEA asteroids with an orbital plane close to the ecliptic. Furthermore, the only way to know if the selected initial Δv range had been well-fit was to let the simulation run until completion and analyse the results, and if they were negative the only way to find a better fit was guesswork. Furthermore, even what the most optimised trajectories for each asteroid looked like was unknown. All of this caused the project's advancement to stop almost completely, delaying both the collection of accurate results for the creation of the economic model and even the composition of this report.

The solution to this issue was to develop a method to obtain a first approximation of the desired results: This is the objective of *preliminary_solver*. This function solves the optimisation problem, but with a significant difference: It neglects the gravitational effects of the Earth-Moon system and operates just in the heliocentric one. For each possible launch date, the spacecraft starts at rest in the Earth-Moon synodic frame at the L_1 Lagrange point. However, instead of then propelling itself to leave its SOI, and once it has done that solve the Lambert problem towards the target, the function transforms that initial state into the heliocentric frame of reference and solves it from there, neglecting both the Earth's pull as it leaves its SOI and any possible assistance that the Moon might offer. The way its nested structure works specifically will be explained in the rest of the main function's description, since *preliminary_solver* is derived from it and thus are very similar, so it will not be repeated here. What matters is that it outputs the value of the minimum departure Δv it finds, as well as its associated trip time between the starting point and the target. The entire function is solved in mere minutes, even with a very wide range of possible flight times.

This large number of flight times, however, generated an unexpected problem: The solver refused to work beyond 9 October 2053, which limited the number of available solutions at the end of the studied period. At first, the issue was thought to be an error in translating between UTC and TDB dates, prompting a modification in the way the start date vector is computed. However, that did not solve the error. The asteroid ephemeris kernels were re-downloaded multiple times, but the problem persisted. Finally, the source of the issue was found: To calculate the planets ephemerides, *semat* used the DE 421 ephemeris catalogue, which is indeed limited to that date. The error was then solved by downloading the more up-to-date DE 438 version, which goes up to 2100, and modifying *load_kernels* to use it instead of the older one.

With those two preliminary values in the main function, the optimisation parameter vectors are generated from them: The initial Δv_0 ranges from 0.4 km/s, the minimum necessary to escape the Earth-Moon system, to more than 2 km/s from the preliminary optimal departure value; while the possible flight times are studied over 750 days in 6-day increments, from 30 less to 2 years more than the preliminary value, and a minimum value of 4 days as seen in [23]. The deflection angle α_0 , which is not subject to this first estimation, ranges from 0 to π rad in 22.5 degree steps.

Finally, the CR3BP integrator configuration options are added in. First of all, the integration timespan: It ranges from the starting point to a maximum of a sidereal period, enough for a spacecraft in a escape trajectory to leave Earth’s SOI. This is expressed adimensionally as 2π .

Then, the integrator’s events at which it should stop even if the timespan was not over were defined in the *odezero_EARTHSOI* function, stored in the *ode* folder. These are:

- The asteroid crashes against the Earth.
- The asteroid crashes against the Moon.
- The asteroid escapes the Earth’s SOI.

With all the parameters in place, the optimisation process can start. This consists of four nested levels of for loops, which look for the most optimal combination of their variables’ values. The order in which they are executed conditions the algorithm’s overall performance and run-time, so a lot of consideration went into it. The definitive choice will now be explained, together with the issues that the alternatives caused.

The first level is the selection of the different values of the initial Δv norm, Δv_0 .

The second level is the choice of the initial Δv deflection angle, α_0 . With that and the previous variable, the spacecraft’s initial velocity is obtained. By combining its initial position with it, the six-variable initial state vector is composed. This vector is then concatenated with the default initial value of the state transition matrix (STM).

Finally, these parameters are sent into the integration function. Initially, it was a custom one written for the project; however the new version of the algorithm uses `se-mat's cr3bp_derivatives_42` function. `cr3bp_derivatives_42` is a variable order Adams-Bashforth-Moulton `ode113` integrator that contains the formulas of the state vector magnitudes' derivatives: for the positions, these are the velocities, and for the velocities, they are the accelerations in the synodic frame of reference, whose formulas can be found in equation 14. To increase precision, to the 6 first-order derivatives it adds a 36-term state transition matrix (STM) calculated with the second-order derivatives, that allows for an extra order of precision when modelling the system's behaviour. The integrator concludes by returning to the main function the adimensional time value and the state vector at the instant where the spacecraft reaches the limit of the Earth's SOI.

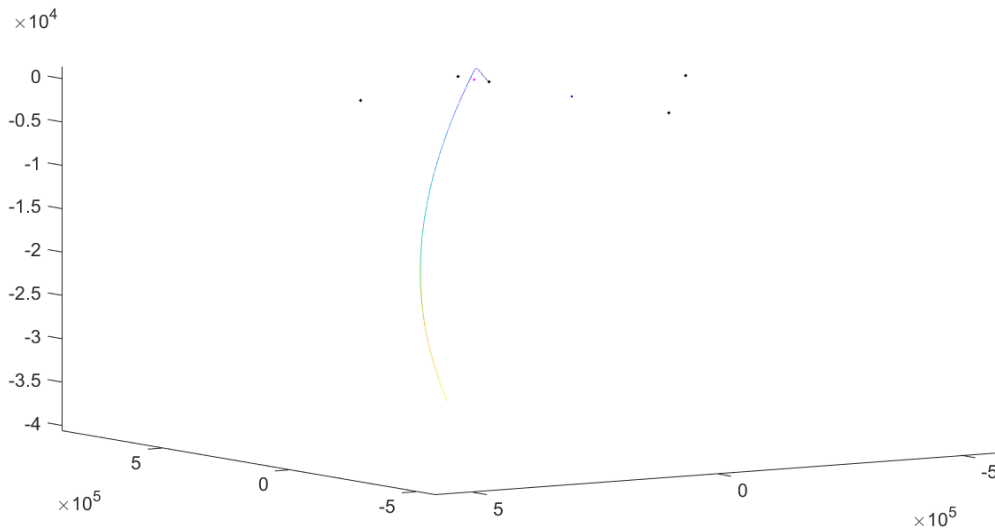


Figure 15: Trajectory in the synodic frame of reference for $\Delta v_0 = 2.5$ km/s and $\alpha_0 = 30^\circ$. The Earth and the Moon are shown as blue and magenta dots, respectively. Axes not to scale

The time value and state vector at SOI then go to the next level of the optimisation. The iterative variable this time is the mission's start date. At first, this step was executed in a regular for loop like the others, but since the aim of the optimiser is to find the least Δv -intensive combination of parameters for each start date, it was set up as a parfor loop instead: Since the results for each launch date are independent from each other, the analysis for each start date can be run in parallel without interfering with one another. That way, each of the computer's processor cores is running its own separate iteration of the loop, a significant increase of processing capacity from that of standard Matlab scripts, which only make use of one core save for in the case of some functions that come pre-programmed with parallel computing capabilities. The first consideration was to put this loop in first place, but that way all permutations of the CR3BP trajectory integration had to be iterated for each launch date, which is extremely wasteful for two reasons:

- The integration is a relatively time-intensive process, so repeating it should be avoided as much as possible.
- The integration results in the synodic frame are the same for all launch dates, making obtaining them separately for each one pointless.

Running a parfor loop comes with its own set of requirements, however:

- Matlab’s Parallel Computing Toolbox has to be installed in the computer that is running the algorithm.
- Certain variables do not transfer well from the general workspace to the parfor loop’s as it will be explained next.

This is the case for the mice kernels that had been loaded at the start of the algorithm. The cause for that might be that parfor does not recognise them since technically they are not part of either semat or the regular Matlab environment. At any rate, that initial *load_kernels* function has to still be called to modify the *default* struct, but now a new version has to also be run at the start of each parfor iteration that loads the kernels without affecting the struct. This modified function is called *load_kernels_alt*, and unlike the original one it does not require any input variables. Before ending the parfor loop, the kernels that were loaded at its start are cleared out using the new *unload_kernels_alt* function. This is caused by the fact that despite having to start them manually at the beginning of each parfor loop, they are not stopped at its end, so with each iteration SPICE’s memory buffer gets added new data until it overflows.

With the SPICE kernels activated, the time and state vector at SOI are sent, with the parfor loop’s start date, the *cr3bp* struct and the Earth-Moon system’s characteristic time, into the *syn2scECLIPJ2000* change of frame of reference function. Like its name says, it changes the state vector’s position and velocity from the Earth-Moon synodic one to the J2000 inertial heliocentric ecliptic one, while dimensionalising them. This function is a modification of the default semat *syn2J2000* change of reference, which transforms the state vector to the inertial geocentric equatorial J2000 frame. To do so, it obtains the ephemerides of the Sun, the Earth and the Moon at the time of escaping the Earth’s SOI from the chosen launch date using SPICE’s *spkezr* function, and then uses these to perform the necessary translations and rotations. Once it is finished, it sends the values back to the main function. The result is that the time and state vector at SOI are transformed into the number of seconds between it and J2000 TDB, and into the same frame of reference as the asteroid ephemerides, respectively.

When both frames of reference are inertial, to go from a geocentric to an heliocentric one only requires adding a simple Earth/Sun position and velocity translation. Changing from the equatorial to the ecliptic reference plane is just a matter of modifying a variable in the *spkezr* calls. However, it is an important factor that was not found out about until late in development, when a 23.4° inclination discrepancy was noticed, and it was realised that the planetary and asteroid ephemerides had been using different reference planes.

Another matter that should be taken into account is that this transformation applies the Earth and Moon’s true positions and velocities at the corresponding instant instead of the idealised ones used in the CR3BP, so the spacecraft’s position and velocity components differ noticeably in value due to using the *syn2J2000* function instead of *syn2eci*, when in theory they are performing the same change of reference frame. This is also an argument in favour of also using SPICE kernels to obtain the target asteroids’ ephemerides, as it

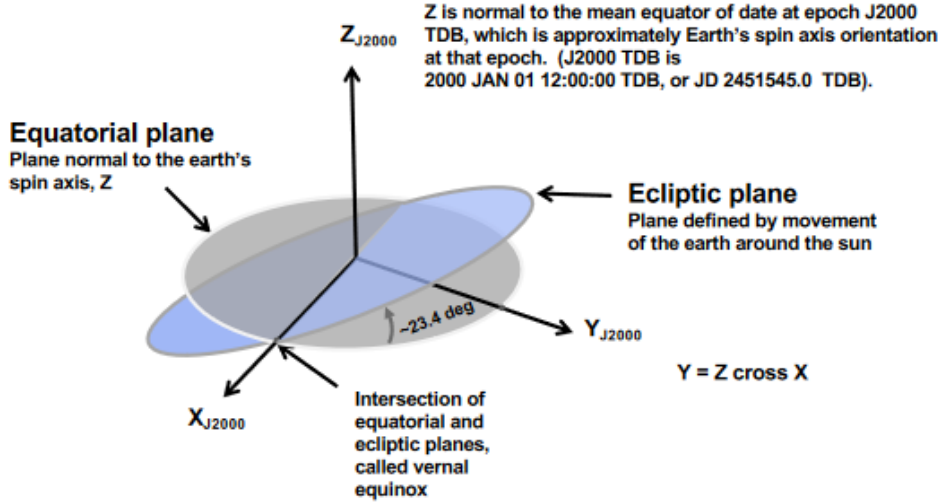


Figure 16: Inclination differences between equatorial and ecliptical inertial frames. Source: [42]

has finally been done.

The variable in the final for loop is the flight time. For each one of its possible values, it finds the target's ephemerides at the corresponding rendezvous date and then solves the ensuing Lambert problem. With the resulting spacecraft velocities at SOI and target rendezvous, it calculates the norms of the departure and arrival Δv s, and after adding them to the initial Δv norm of the first level of the iteration, it obtains the total mission Δv for that combination of values of the parametric variables. It then compares its value to the minimum one for that start date. If it is smaller, it becomes the new minimum value, and the corresponding parameters are also overwritten. At the end of all iterations, the result are 5 vectors of optimised variables for each start date: the three parameters, the total mission Δv and the Δv at departure from SOI. This last one serves as a measure for the effectiveness of the Lunar gravity assist: The lower its value, the more it is capable of deflecting the spacecraft's velocity in the right direction and the less it has to be corrected towards the target at SOI, which should in principle contribute to a reduction in the total Δv .

Lastly, in order to provide a visual representation of the optimised results, the programme takes the vector of optimised total mission Δv over all the possible launch dates and picks the mission with the lowest one of them all. From there, it takes its parameters and it computes the whole mission from launch to rendezvous, calculating the state spaces of the spacecraft, the target asteroid, the Earth and Mars over time, and finally plotting their trajectories.

3.3.5 Discussion of the results

The implementation of the first estimation has corrected many of the previously mentioned issues with the algorithm: Its total run-time has been massively decreased to an estimated average of between 30 minutes and 3 hours, depending on the target; a significant improvement to previous versions that lasted more than a day. However, a large part

of the reduction has been achieved by enlarging the start date and flight time step sizes from 1 to 6 days, abandoning improvements in that area with regards to the referenced algorithms. Still, the optimisation parameters are much better fit to each target than before, and the optimised results can be validated.

To check their consistency, the trajectory towards NEA 2003 LN6 was calculated. This asteroid was used as the example in [23], so numerical results can be compared between them. Since that algorithm takes into account the return trip to Earth, the total Δv cannot be used for this purpose; however, there is a metric that is available in both cases: The Earth SOI departure Δv that sets the spacecraft in its trajectory towards the target asteroid, which is obtained by solving the Lambert problem. Its value for the minimum total Δv case is shown for the most optimal case in the reference and the two most optimal ones for this one:

| 2003 LN6 optimal Δv_{SOI} | km/s |
|--------------------------------------|--------|
| Reference: Most optimal case | 0.1122 |
| New algorithm: Most optimal case | 0.0750 |
| New algorithm: 2nd most optimal case | 0.1426 |

Table 1: Comparison of Δv at SOI values between the referenced and developed algorithms

The results are coherent with those in [23], while at the same time showing an improvement for the most optimal case, as it was the objective for this project. In general, when compared with the performance of the referenced algorithms, especially that of [23], this one shows significant improvements: It successfully implements the Moon’s true ephemerides instead of using a simplified model that assumes it is located in the ecliptic plane. Using the gravity assist to aid in the spacecraft’s change of plane is also a consideration that had been made in that study but not implemented. For that matter, the initial Δv there had a fixed value, with most of the change in trajectory provided by the unassisted manoeuvres at the Earth’s SOI and at rendez-vous with the target; the authors expressed the desire to implement a system to reduce their contribution and maximise the former’s: This has been successfully implemented in this project. On the other hand, the fact that it currently only considers the outbound part of a mining expedition, with no consideration for the return trip, shows that there are still further areas of improvement in the future.

The plots of the total mission Δv values for each launch date can be found in annex B.1, while those of the most favourable trajectories towards each target are in B.2. When analysing the results, the first thing one notices is the large variability in the total trip Δv value over time: There are narrow periodical windows in which the trip cost is minimised, separated by large time-spans in which it increases massively. This behaviour coincides with that of real-life interplanetary missions, and Hohmann transfers in general. Regarding the minimums, two trends in their distribution of values can be observed, depending on the region of the Solar System where the targets are found: Main Belt Asteroids tend to display a smaller amount of variability in their values, while their lowest ones are relatively high: This is due to both their larger semi-major axis and their lower orbital inclination and eccentricity. Near-Earth Asteroids, on the other hand, are much more diverse in their orbital characteristics, resulting in either the cheapest targets to attain, the

most expensive, or the ones with the highest amount of variability between the minimum Δv 's values, due to their diversity in the three previously-mentioned orbital parameters.

A noticeable increase in precision was achieved in the calculations of certain targets thanks to the use of JPL's Small Body Database ephemerides integrated using the Solar System's n-body problem over the entire range of possible launch dates, instead of using the orbital parameters at the reference epoch and extrapolating them over time while considering only a 2-body problem. This is especially true for (99942) Apophis, whose close approach to the Earth in 2036 will modify its orbit around the Sun due to the same principles that would be used in the Earth-Moon gravity assist, as seen in 3.2.4. The previous approach would not have been able to take it into account, while the new one does.

With the economic distances towards the studied targets, all the data was in place to implement the gravity trade model in the following section.

4 The gravity trade model

After the trajectory algorithm's simulations were carried out on the targets, Δv plots for each of the asteroids were generated. In order to obtain results that were valid for the entire 30-year launch window, instead of just using the lowest Δv window, since the values of the bottoms of the periodic minimums can vary a lot at each approximation between the Earth and an asteroid, the average value of the five least expensive windows is used instead. Naturally, only the minimums were used instead of the whole data set because it does not make sense to launch the mission at a less favourable time from an energetic, and therefore economic cost, point of view. Once that part was complete, each asteroid's "favourability factor" was calculated. Its formula, derived from that of the trade flow seen in 1, is:

$$F_j = \frac{M_j}{D_j} \quad (33)$$

Where M_j is its economic size and D_j is the exponential of the averaged minimum Δv , in km/s. This factor, multiplied by the Earth's economic size, would result in the trade volume between the two bodies, but since the value of the planet's economy is the same with regards to all of the targets, the factor can be used to find which asteroid would have a higher volume of commerce with Earth, and consequently will be more economically attractive. Due to the large magnitude of the results, the decimal logarithm of the favourability factor is presented instead. The values for each studied target can be found in C.1.

The results show that the current model is most weighted towards the asteroids' total economic size, displaying a higher degree of favourability for the largest asteroids that have been analysed over those that are easiest to reach from the Earth: See how the most massive asteroids in the Main Belt appear to be 5 or 6 orders of magnitude more interesting to exploit than NEAs that have actually been visited by probes, like (25143) Itokawa, which should be proof of their higher viability. This suggests that the model is most appropriate for evaluating the commercial flow between our planet and other celestial bodies over very long periods of time, so the benefit of having more material available for extraction becomes more prominent, and for an scenario where propellant consumption is not such a big concern, like one where orbital refueling stations or propellant generation on the asteroids themselves are available. Attempts to correct this tendency by adding more weight to the economic distance term did not yield a model that is more accurate to the fact that not all the material from an asteroid can be harvested at once, or that the largest obstacle to interplanetary economic development, at least with humanity's current technological capabilities, lies in the exponential increase of the mass required to visit a celestial body the harder it is to reach, and its associated cost. A different concept for the economic size of the asteroids, based on humanity's annual capacity of resource extraction from them instead of the total available resources, would also produce a more accurate substitute for GDP in the Earth-based gravity trade model, but until the technology for large-scale space mining is not implemented or at least better conceptually defined such a model will not be available.

5 Conclusions

In summary, this project was successful at developing a tentative approach to exporting the concepts of Earth-based gravity trade models to the interplanetary environment, developing the ideas of economic size and distance in this context using a new model that is innovative but shows clear conceptual gaps that can be improved and expanded upon.

For the economic size of asteroids combining cosmochemical, spectroscopic and orbitographic observations to estimate their total value is an original approach, however the number of studied types can be increased to include the parent bodies of iron and stony iron meteorites, which are potentially much more economically attractive than chondrites. Speaking of which, the current model does not take into consideration their mineralogical properties and the ease with which valuable materials can be extracted from them, and what the real capacity for extraction over a set period of time would be.

For the economic distance, the new trajectory algorithm improves on those in the referenced literature by providing a more robust and precise approach to adding a lunar gravity assist that reduces the trip cost to the targeted asteroids, in a work that also serves to expand the capabilities of the SEMAT toolkit for studying interplanetary missions. The main area of improvement in this side of the project would be defining the amount of time required for mining operations so that the return trip and therefore the total mission cost can be more accurately studied.

Bibliography

- [1] M. Abe et al. “Near-Infrared Spectral Results of Asteroid Itokawa from the Hayabusa Spacecraft”. In: *Science* 312.5778 (2006), pp. 1334–1338. ISSN: 0036-8075. DOI: 10.1126/science.1125718. eprint: <https://science.sciencemag.org/content/312/5778/1334.full.pdf>. URL: <https://science.sciencemag.org/content/312/5778/1334>.
- [2] Shinsuke Abe et al. “Mass and Local Topography Measurements of Itokawa by Hayabusa”. In: *Science* 312.5778 (2006), pp. 1344–1347. ISSN: 0036-8075. DOI: 10.1126/science.1126272. eprint: <https://science.sciencemag.org/content/312/5778/1344.full.pdf>. URL: <https://science.sciencemag.org/content/312/5778/1344>.
- [3] P. A. Abell et al. “Compositional Investigation of Binary Near-Earth Asteroid 66063 (1998 RO1): A Potentially Undifferentiated Assemblage”. In: *36th Annual Lunar and Planetary Science Conference*. Ed. by S. Mackwell and E. Stansbery. Vol. 36. Lunar and Planetary Science Conference. Mar. 2005.
- [4] Brent Barbee et al. “A Comprehensive Ongoing Survey of the Near-Earth Asteroid Population for Human Mission Accessibility”. In: *AIAA/AAS Astrodynamics Specialist Conference*. DOI: 10.2514/6.2010-8368. eprint: <https://arc.aiaa.org/doi/pdf/10.2514/6.2010-8368>. URL: <https://arc.aiaa.org/doi/abs/10.2514/6.2010-8368>.
- [5] L. Beauvalet and F. Marchis. “Multiple asteroid systems (45) Eugenia and (87) Sylvia: Sensitivity to external and internal perturbations”. In: *Icarus* 241 (2014), pp. 13–25. ISSN: 0019-1035. DOI: <https://doi.org/10.1016/j.icarus.2014.06.004>. URL: <http://www.sciencedirect.com/science/article/pii/S0019103514003157>.
- [6] Behrend, R. et al. “Four new binary minor planets: (854) Frostia, (1089) Tama, (1313) Berna, (4492) Debussy”. In: *A&A* 446.3 (2006), pp. 1177–1184. DOI: 10.1051/0004-6361:20053709. URL: <https://doi.org/10.1051/0004-6361:20053709>.
- [7] THOMAS H. BURBINE. “Could G-class asteroids be the parent bodies of the CM chondrites?” In: *Meteoritics & Planetary Science* 33.2 (1998), pp. 253–258. DOI: 10.1111/j.1945-5100.1998.tb01630.x. eprint: <https://onlinelibrary.wiley.com/doi/pdf/10.1111/j.1945-5100.1998.tb01630.x>. URL: <https://onlinelibrary.wiley.com/doi/abs/10.1111/j.1945-5100.1998.tb01630.x>.
- [8] Carry, B. et al. “Homogeneous internal structure of CM-like asteroid (41) Daphne”. In: *A&A* 623 (2019), A132. DOI: 10.1051/0004-6361/201833898. URL: <https://doi.org/10.1051/0004-6361/201833898>.

- [9] B. Carry. “Density of asteroids”. In: *Planetary and Space Science* 73.1 (2012). Solar System science before and after Gaia, pp. 98–118. ISSN: 0032-0633. DOI: <https://doi.org/10.1016/j.pss.2012.03.009>. URL: <http://www.sciencedirect.com/science/article/pii/S0032063312000773>.
- [10] Thomas Chaney. “The Gravity Equation in International Trade: An Explanation”. In: *Journal of Political Economy* 126.1 (2018), pp. 150–177. DOI: 10.1086/694292. eprint: <https://doi.org/10.1086/694292>. URL: <https://doi.org/10.1086/694292>.
- [11] Steven R. Chesley et al. “Orbit and bulk density of the OSIRIS-REx target Asteroid (101955) Bennu”. In: *Icarus* 235 (2014), pp. 5–22. ISSN: 0019-1035. DOI: <https://doi.org/10.1016/j.icarus.2014.02.020>. URL: <http://www.sciencedirect.com/science/article/pii/S0019103514001067>.
- [12] Beth Ellen Clark et al. “Spectroscopy of B-type asteroids: Subgroups and meteorite analogs”. In: *Journal of Geophysical Research: Planets* 115.E6 (2010). DOI: 10.1029/2009JE003478. eprint: <https://agupubs.onlinelibrary.wiley.com/doi/pdf/10.1029/2009JE003478>. URL: <https://agupubs.onlinelibrary.wiley.com/doi/abs/10.1029/2009JE003478>.
- [13] E.A. Cloutis et al. “Spectral reflectance properties of carbonaceous chondrites: 2. CM chondrites”. In: *Icarus* 216.1 (2011), pp. 309–346. ISSN: 0019-1035. DOI: <https://doi.org/10.1016/j.icarus.2011.09.009>. URL: <http://www.sciencedirect.com/science/article/pii/S001910351100354X>.
- [14] E.A. Cloutis et al. “Spectral reflectance properties of carbonaceous chondrites 4: Aqueously altered and thermally metamorphosed meteorites”. In: *Icarus* 220.2 (2012), pp. 586–617. ISSN: 0019-1035. DOI: <https://doi.org/10.1016/j.icarus.2012.05.018>. URL: <http://www.sciencedirect.com/science/article/pii/S001910351200200X>.
- [15] G.J. Consolmagno, D.T. Britt, and R.J. Macke. “The significance of meteorite density and porosity”. In: *Geochemistry* 68.1 (2008), pp. 1–29. ISSN: 0009-2819. DOI: <https://doi.org/10.1016/j.chemer.2008.01.003>. URL: <http://www.sciencedirect.com/science/article/pii/S0009281908000044>.
- [16] Jenna L. Crowell et al. “Radar and Lightcurve Shape Model of Near-Earth Asteroid (1627) Ivar”. In: *Icarus* 291 (2017), pp. 254–267. ISSN: 0019-1035. DOI: <https://doi.org/10.1016/j.icarus.2016.11.008>. URL: <http://www.sciencedirect.com/science/article/pii/S001910351630166X>.
- [17] de León, J. et al. “New observations of asteroid (175706) 1996 FG3, primary target of the ESA Marco Polo-R mission”. In: *A&A* 530 (2011), p. L12. DOI: 10.1051/0004-6361/201117041. URL: <https://doi.org/10.1051/0004-6361/201117041>.
- [18] Tasha L. Dunn et al. “Mineralogies and source regions of near-Earth asteroids”. In: *Icarus* 222.1 (2013), pp. 273–282. ISSN: 0019-1035. DOI: <https://doi.org/10.1016/j.icarus.2012.11.007>. URL: <http://www.sciencedirect.com/science/article/pii/S0019103512004538>.
- [19] Julia Fang and Jean-Luc Margot. “NEAR-EARTH BINARIES AND TRIPLES: ORIGIN AND EVOLUTION OF SPIN-ORBITAL PROPERTIES”. In: *The Astrophysical Journal* 143.1 (Dec. 2011), p. 24. DOI: 10.1088/0004-6256/143/1/24. URL: <https://doi.org/10.1088/0004-6256/143/1/24>.

- [20] Julia Fang et al. “ORBITS OF NEAR-EARTH ASTEROID TRIPLES 2001 SN263 AND 1994 CC: PROPERTIES, ORIGIN, AND EVOLUTION”. In: *The Astronomical Journal* 141.5 (Mar. 2011), p. 154. DOI: 10.1088/0004-6256/141/5/154. URL: <https://doi.org/10.1088/0004-6256/141/5/154>.
- [21] G. Gómez and E. Barrabés. “Space Manifold dynamics”. In: *Scholarpedia* 6.2 (2011). revision #137032, p. 10597. DOI: 10.4249/scholarpedia.10597.
- [22] V. E. Hamilton et al. “Evidence for widespread hydrated minerals on asteroid (101955) Bennu”. In: *Nature Astronomy* 3.4 (2019), pp. 332–340. ISSN: 2397-3366. DOI: 10.1038/s41550-019-0722-2. URL: <https://doi.org/10.1038/s41550-019-0722-2>.
- [23] S. Hernandez and B. Barbee. “Design of Round-trip Trajectories to Near-Earth Asteroids Utilizing a Lunar Flyby”. In: *21st AAS/AIAA Space Flight Mechanics Meeting*. (New Orleans, Louisiana, USA). Feb. 13, 2011. URL: <https://ntrs.nasa.gov/search.jsp?R=20110008138>.
- [24] T. Hiroi et al. “Possible thermal metamorphism on the C, G, B, and F asteroids detected from their reflectance spectra in comparison with carbonaceous chondrites”. In: *Antarctic Meteorite Research* 7 (Mar. 1994), p. 230.
- [25] Harry Jones. “The Recent Large Reduction in Space Launch Cost”. In: 48th International Conference on Environmental Systems. 2018.
- [26] Jet Propulsion Laboratory. *JPL Small-Body Database Browser*. 1999. URL: <https://ssd.jpl.nasa.gov/sbdb.cgi> (visited on 05/30/2019).
- [27] S.S. Lindsay et al. “Composition, mineralogy, and porosity of multiple asteroid systems from visible and near-infrared spectral data”. In: *Icarus* 247 (2015), pp. 53–70. ISSN: 0019-1035. DOI: <https://doi.org/10.1016/j.icarus.2014.08.040>. URL: <http://www.sciencedirect.com/science/article/pii/S0019103514004576>.
- [28] Katarzyna Łuszczek and Tadeusz A. Przylibski. “Potential deposits of selected metallic resources on L chondrite parent bodies”. In: *Planetary and Space Science* 168 (2019), pp. 40–51. ISSN: 0032-0633. DOI: <https://doi.org/10.1016/j.pss.2019.02.005>. URL: <http://www.sciencedirect.com/science/article/pii/S0032063318302368>.
- [29] Franck Marchis et al. “A low density of 0.8 g cm⁻³ for the Trojan binary asteroid 617 Patroclus”. In: *Nature* 439.7076 (2006), pp. 565–567. ISSN: 1476-4687. DOI: 10.1038/nature04350. URL: <https://doi.org/10.1038/nature04350>.
- [30] F. Marchis et al. “Characteristics and large bulk density of the C-type main-belt triple asteroid (93) Minerva”. In: *Icarus* 224.1 (2013), pp. 178–191. ISSN: 0019-1035. DOI: <https://doi.org/10.1016/j.icarus.2013.02.018>. URL: <http://www.sciencedirect.com/science/article/pii/S0019103513000808>.
- [31] F. Marchis et al. “Main belt binary asteroidal systems with circular mutual orbits”. In: *Icarus* 196.1 (2008), pp. 97–118. ISSN: 0019-1035. DOI: <https://doi.org/10.1016/j.icarus.2008.03.007>. URL: <http://www.sciencedirect.com/science/article/pii/S0019103508001073>.
- [32] F. Marchis et al. “Main belt binary asteroidal systems with eccentric mutual orbits”. In: *Icarus* 195.1 (2008), pp. 295–316. ISSN: 0019-1035. DOI: <https://doi.org/10.1016/j.icarus.2007.12.010>. URL: <http://www.sciencedirect.com/science/article/pii/S0019103507006124>.

- [33] J. L. Margot et al. “Radar Discovery and Characterization of Binary Near-Earth Asteroids”. In: *Lunar and Planetary Science Conference*. Vol. 33. Lunar and Planetary Science Conference. Mar. 2002.
- [34] Margaret M. McAdam et al. “Spectral evidence for amorphous silicates in least-processed CO meteorites and their parent bodies”. In: *Icarus* 306 (2018), pp. 32–49. ISSN: 0019-1035. DOI: <https://doi.org/10.1016/j.icarus.2018.01.024>. URL: <http://www.sciencedirect.com/science/article/pii/S0019103517304694>.
- [35] H. Y. McSween Jr. and G. H. Huss. *Cosmochemistry*. Cambridge University Press, 2012. ISBN: 978-0-511-72968-3.
- [36] David Mimoun. *Cours Mécanique Céleste Avancée*. Dec. 2017.
- [37] J.D. Mireles James. *Celestial Mechanics Notes Set 4: The Circular Restricted Three Body Problem*. Dec. 2006.
- [38] Gavin M. Mudd. “Gold mining in Australia: linking historical trends and environmental and resource sustainability”. In: *Environmental Science & Policy* 10.7 (2007), pp. 629–644. ISSN: 1462-9011. DOI: <https://doi.org/10.1016/j.envsci.2007.04.006>. URL: <http://www.sciencedirect.com/science/article/pii/S1462901107000706>.
- [39] Müller, T. G. et al. “Thermal infrared observations of asteroid (99942) Apophis with Herschel”. In: *A&A* 566 (2014), A22. DOI: 10.1051/0004-6361/201423841. URL: <https://doi.org/10.1051/0004-6361/201423841>.
- [40] S. P. Naidu et al. “RADAR IMAGING AND CHARACTERIZATION OF THE BINARY NEAR-EARTH ASTEROID (185851) 2000 DP107”. In: *The Astronomical Journal* 150.2 (July 2015), p. 54. DOI: 10.1088/0004-6256/150/2/54. URL: <https://doi.org/10.1088/0004-6256/150/2/54>.
- [41] The Navigation and Ancillary Information Facility. *About SPICE*. 2019. URL: <https://naif.jpl.nasa.gov/naif/aboutspice.html>.
- [42] Navigation and Ancillary Information Facility. *An Overview of Reference Frames and Coordinate Systems in the SPICE Context*. June 2019.
- [43] OpenMDAO 1.7.3 Alpha documentation. *Hohmann Transfer Tutorial - Optimizing a Spacecraft Manuever*. 2015. URL: https://openmdao.readthedocs.io/en/1.7.3/_images/hohmann_dv1.png.
- [44] Steven. J. Ostro et al. “Radar Imaging of Binary Near-Earth Asteroid (66391) 1999 KW4”. In: *Science* 314.5803 (2006), pp. 1276–1280. ISSN: 0036-8075. DOI: 10.1126/science.1133622. eprint: <https://science.sciencemag.org/content/314/5803/1276.full.pdf>. URL: <https://science.sciencemag.org/content/314/5803/1276>.
- [45] Steven J. Ostro et al. “Radar Observations of Asteroid 1620 Geographos”. In: *Icarus* 121.1 (1996), pp. 46–66. ISSN: 0019-1035. DOI: <https://doi.org/10.1006/icar.1996.0071>. URL: <http://www.sciencedirect.com/science/article/pii/S0019103596900718>.
- [46] Myriam Pajuelo et al. “Spectral properties of binary asteroids”. In: *Monthly Notices of the Royal Astronomical Society* 477.4 (Apr. 2018), pp. 5590–5604. ISSN: 0035-8711. DOI: 10.1093/mnras/sty1013. eprint: <http://oup.prod.sis.lan/mnras/article-pdf/477/4/5590/24955549/sty1013.pdf>. URL: <https://doi.org/10.1093/mnras/sty1013>.

- [47] Perna, D. et al. “The triple near-Earth asteroid (153591) 2001 SN263: an ultra-blue, primitive target for the Aster space mission”. In: *A&A* 568 (2014), p. L6. DOI: 10.1051/0004-6361/201424447. URL: <https://doi.org/10.1051/0004-6361/201424447>.
- [48] Popescu, M. et al. “Near-Earth asteroids spectroscopic survey at Isaac Newton Telescope”. In: *A&A* 627 (2019), A124. DOI: 10.1051/0004-6361/201935006. URL: <https://doi.org/10.1051/0004-6361/201935006>.
- [49] P. Pravec et al. “Photometric survey of binary near-Earth asteroids”. In: *Icarus* 181.1 (2006), pp. 63–93. ISSN: 0019-1035. DOI: <https://doi.org/10.1016/j.icarus.2005.10.014>. URL: <http://www.sciencedirect.com/science/article/pii/S0019103505003891>.
- [50] Vishnu Reddy and Juan Sanchez. *NEA (66391) 1999 KW₄ Observing Campaign Gallery*. May 2019. URL: http://iawn.net/obscomp/1999KW4/1999KW4_gallery.shtml.
- [51] D. C. Richardson et al. “Dynamical and Physical Properties of 65803 Didymos”. In: *Lunar and Planetary Science Conference*. Vol. 47. Lunar and Planetary Science Conference. Mar. 2016, p. 1501.
- [52] Rozitis, B. et al. “A thermophysical analysis of the (1862) Apollo Yarkovsky and YORP effects”. In: *A&A* 555 (2013), A20. DOI: 10.1051/0004-6361/201321659. URL: <https://doi.org/10.1051/0004-6361/201321659>.
- [53] Michael K. Shepard et al. “Radar and infrared observations of binary near-Earth Asteroid 2002 CE26”. In: *Icarus* 184.1 (2006), pp. 198–210. ISSN: 0019-1035. DOI: <https://doi.org/10.1016/j.icarus.2006.04.019>. URL: <http://www.sciencedirect.com/science/article/pii/S0019103506001357>.
- [54] SMM. *Shanghai Metals Market*. 1999. URL: <https://www.metal.com/> (visited on 06/12/2019).
- [55] U.S. Geological Survey. *Commodity Statistics and Information*. URL: <https://www.usgs.gov/centers/nmic/commodity-statistics-and-information/> (visited on 06/12/2019).
- [56] Minghu Tan, Colin McInnes, and Matteo Ceriotti. “Low-energy near Earth asteroid capture using Earth flybys and aerobraking”. In: *Advances in Space Research* 61.8 (2018), pp. 2099–2115. ISSN: 0273-1177. DOI: <https://doi.org/10.1016/j.asr.2018.01.027>. URL: <http://www.sciencedirect.com/science/article/pii/S0273117718300723>.
- [57] Taylor, J. *carbonaceous chondrite: Allende meteorite*. URL: <https://www.britannica.com/science/carbonaceous-chondrite/>.
- [58] UK Defence Journal. *British firm Cobham to supply Lockheed Martin Orion spacecraft crew module elements*. 2018. URL: <https://ukdefencejournal.org.uk/british-firm-cobham-to-supply-lockheed-martin-orion-spacecraft-crew-module-elements/>.
- [59] P. Vernazza et al. “Multiple and Fast: The Accretion of Ordinary Chondrite Parent Bodies”. In: *The Astrophysical Journal* 791.2, 120 (Aug. 2014), p. 120. DOI: 10.1088/0004-637X/791/2/120. arXiv: 1405.6850 [astro-ph.EP].

- [60] P. Vernazza et al. “Paucity of Tagish Lake-like parent bodies in the Asteroid Belt and among Jupiter Trojans”. In: *Icarus* 225.1 (2013), pp. 517–525. ISSN: 0019-1035. DOI: <https://doi.org/10.1016/j.icarus.2013.04.019>. URL: <http://www.sciencedirect.com/science/article/pii/S001910351300184X>.
- [61] J. Veverka et al. “NEAR’s Flyby of 253 Mathilde: Images of a C Asteroid”. In: *Science* 278.5346 (1997), pp. 2109–2114. ISSN: 0036-8075. DOI: 10.1126/science.278.5346.2109. eprint: <https://science.sciencemag.org/content/278/5346/2109.full.pdf>. URL: <https://science.sciencemag.org/content/278/5346/2109>.
- [62] S. Widnall. *Lecture L18 - Exploring the Neighborhood: the Restricted Three-Body Problem*. 2008.
- [63] D. K. Yeomans et al. “Estimating the Mass of Asteroid 253 Mathilde from Tracking Data During the NEAR Flyby”. In: *Science* 278.5346 (1997), pp. 2106–2109. ISSN: 0036-8075. DOI: 10.1126/science.278.5346.2106. eprint: <https://science.sciencemag.org/content/278/5346/2106.full.pdf>. URL: <https://science.sciencemag.org/content/278/5346/2106>.
- [64] D. K. Yeomans et al. “Radio Science Results During the NEAR-Shoemaker Spacecraft Rendezvous with Eros”. In: *Science* 289.5487 (2000), pp. 2085–2088. ISSN: 0036-8075. DOI: 10.1126/science.289.5487.2085. eprint: <https://science.sciencemag.org/content/289/5487/2085.full.pdf>. URL: <https://science.sciencemag.org/content/289/5487/2085>.
- [65] LiangLiang Yu, Jianghui Ji, and Su Wang. “Shape, thermal and surface properties determination of a candidate spacecraft target asteroid (175706) 1996 FG3”. In: *Monthly Notices of the Royal Astronomical Society* 439.4 (Feb. 2014), pp. 3357–3370. ISSN: 0035-8711. DOI: 10.1093/mnras/stu164. eprint: <http://oup.prod.sis.lan/mnras/article-pdf/439/4/3357/3955289/stu164.pdf>. URL: <https://doi.org/10.1093/mnras/stu164>.
- [66] William Zielenbach. “MASS DETERMINATION STUDIES OF 104 LARGE ASTEROIDS”. In: *The Astronomical Journal* 142.4 (Sept. 2011), p. 120. DOI: 10.1088/0004-6256/142/4/120. URL: <https://doi.org/10.1088/0004-6256/142/4/120>.

Appendices

A Economic value

A.1 Meteorite elemental mass fractions

| | H chondrites | L chondrites | LL chondrites | L/LL chondrites | CI chondrites | CM chondrites | CV chondrites | CO chondrites |
|----|-----------------|-----------------|------------------|--------------------|------------------|------------------|------------------|------------------|
| Li | 1.70E-06 | 1.85E-06 | 1.80E-06 | 1.83E-06 | 1.50E-06 | 1.50E-06 | 1.70E-06 | 1.80E-06 |
| Be | 3.00E-08 | 4.00E-08 | 4.50E-08 | 4.25E-08 | 2.50E-08 | 4.00E-08 | 5.00E-08 | |
| B | 4.00E-07 | 4.00E-07 | 7.00E-07 | 5.50E-07 | 8.70E-07 | 4.80E-07 | 3.00E-07 | |
| C | 2.10E-03 | 2.50E-03 | 3.10E-03 | 2.80E-03 | 3.45E-02 | 2.20E-02 | 5.30E-03 | 4.40E-03 |
| N | 4.80E-05 | 4.30E-05 | 7.00E-05 | 5.65E-05 | 3.18E-03 | 1.52E-03 | 8.00E-05 | 9.00E-05 |
| O | 3.57E-01 | 3.77E-01 | 4.00E-01 | 3.89E-01 | 4.64E-01 | 4.32E-01 | 3.70E-01 | 3.70E-01 |
| F | 1.25E-04 | 1.00E-04 | 7.00E-05 | 8.50E-05 | 6.00E-05 | 3.80E-05 | 2.40E-05 | 3.00E-05 |
| Na | 6.11E-03 | 6.90E-03 | 6.84E-03 | 6.87E-03 | 5.00E-03 | 3.90E-03 | 3.40E-03 | 4.20E-03 |
| Mg | 1.41E-01 | 1.49E-01 | 1.53E-01 | 1.51E-01 | 9.70E-02 | 1.15E-01 | 1.43E-01 | 1.45E-01 |
| Al | 1.06E-02 | 1.16E-02 | 1.18E-02 | 1.17E-02 | 8.65E-03 | 1.13E-02 | 1.68E-02 | 1.40E-02 |
| Si | 1.71E-01 | 1.86E-01 | 1.89E-01 | 1.88E-01 | 1.06E-01 | 1.27E-01 | 1.57E-01 | 1.58E-01 |
| P | 1.20E-03 | 1.03E-03 | 9.10E-04 | 9.70E-04 | 9.50E-04 | 1.03E-03 | 1.12E-03 | 1.21E-03 |
| S | 2.00E-02 | 2.20E-02 | 2.10E-02 | 2.15E-02 | 5.41E-02 | 2.70E-02 | 2.20E-02 | 2.20E-02 |
| Cl | 1.40E-04 | 2.70E-04 | 2.00E-04 | 2.35E-04 | 7.00E-04 | 4.30E-04 | 2.50E-04 | 2.80E-04 |
| K | 7.80E-04 | 9.20E-04 | 8.80E-04 | 9.00E-04 | 5.50E-04 | 3.70E-04 | 3.60E-04 | 3.60E-04 |
| Ca | 1.22E-02 | 1.33E-02 | 1.32E-02 | 1.33E-02 | 9.26E-03 | 1.29E-02 | 1.84E-02 | 1.58E-02 |
| Sc | 7.80E-06 | 8.10E-06 | 8.00E-06 | 8.05E-06 | 5.90E-06 | 8.20E-06 | 1.02E-05 | 9.50E-06 |
| Ti | 6.30E-04 | 6.70E-04 | 6.80E-04 | 6.75E-04 | 4.40E-04 | 5.50E-04 | 8.70E-04 | 7.30E-04 |
| V | 7.30E-05 | 7.50E-05 | 7.60E-05 | 7.55E-05 | 5.50E-05 | 7.50E-05 | 9.70E-05 | 9.50E-05 |
| Cr | 3.50E-03 | 3.69E-03 | 3.68E-03 | 3.69E-03 | 2.65E-03 | 3.05E-03 | 3.48E-03 | 3.52E-03 |
| Mn | 2.34E-03 | 2.59E-03 | 2.60E-03 | 2.60E-03 | 1.94E-03 | 1.65E-03 | 1.52E-03 | 1.62E-03 |
| Fe | 2.73E-01 | 2.18E-01 | 1.98E-01 | 2.08E-01 | 1.82E-01 | 2.13E-01 | 2.35E-01 | 2.50E-01 |
| Co | 8.30E-04 | 5.80E-04 | 4.80E-04 | 5.30E-04 | 5.05E-04 | 5.60E-04 | 6.40E-04 | 6.80E-04 |
| Ni | 1.71E-02 | 1.24E-02 | 1.06E-02 | 1.15E-02 | 1.10E-02 | 1.23E-02 | 1.32E-02 | 1.42E-02 |
| Cu | 9.40E-05 | 9.00E-05 | 8.50E-05 | 8.75E-05 | 1.25E-04 | 1.30E-04 | 1.04E-04 | 1.30E-04 |
| Zn | 4.70E-05 | 5.70E-05 | 5.60E-05 | 5.65E-05 | 3.15E-04 | 1.80E-04 | 1.10E-04 | 1.10E-04 |
| Ga | 6.00E-06 | 5.40E-06 | 5.30E-06 | 5.35E-06 | 9.80E-06 | 7.60E-06 | 6.10E-06 | 7.10E-06 |
| Ge | 1.00E-05 | 1.00E-05 | 1.00E-05 | 1.00E-05 | 3.30E-05 | 2.60E-05 | 1.60E-05 | 2.00E-05 |
| As | 2.20E-06 | 1.36E-06 | 1.30E-06 | 1.33E-06 | 1.85E-06 | 1.80E-06 | 1.50E-06 | 2.00E-06 |
| Se | 8.00E-06 | 8.50E-06 | 9.00E-06 | 8.75E-06 | 2.10E-05 | 1.20E-05 | 8.70E-06 | 8.00E-06 |
| Br | 1.00E-06 | 2.00E-06 | 1.00E-06 | 1.50E-06 | 3.50E-06 | 3.00E-06 | 1.60E-06 | 1.40E-06 |
| Rb | 2.30E-06 | 2.80E-06 | 2.20E-06 | 2.50E-06 | 2.30E-06 | 1.60E-06 | 1.20E-06 | 1.30E-06 |
| Sr | 8.80E-06 | 1.10E-05 | 1.30E-05 | 1.20E-05 | 7.30E-06 | 1.00E-05 | 1.48E-05 | 1.30E-05 |
| Y | 2.00E-06 | 1.80E-06 | 2.00E-06 | 1.90E-06 | 1.56E-06 | 2.00E-06 | 2.60E-06 | 2.40E-06 |
| Zr | 7.30E-06 | 6.40E-06 | 7.40E-06 | 6.90E-06 | 3.90E-06 | 7.00E-06 | 8.90E-06 | 9.00E-06 |
| Nb | 4.00E-07 | 4.00E-07 | | 2.00E-07 | 2.50E-07 | 4.00E-07 | 5.00E-07 | |
| Mo | 1.40E-06 | 1.20E-06 | 1.10E-06 | 1.15E-06 | 9.20E-07 | 1.40E-06 | 1.80E-06 | 1.70E-06 |
| Ru | 1.10E-06 | 7.50E-07 | | 3.75E-07 | 7.10E-07 | 8.70E-07 | 1.20E-06 | 1.08E-06 |
| Rh | 2.10E-07 | 1.55E-07 | | 7.75E-08 | 1.40E-07 | 1.60E-07 | 1.70E-07 | |
| Pd | 8.45E-07 | 6.20E-07 | 5.60E-07 | 5.90E-07 | 5.60E-07 | 6.30E-07 | 7.10E-07 | 7.10E-07 |
| Ag | 4.50E-08 | 5.00E-08 | 7.50E-08 | 6.25E-08 | 2.00E-07 | 1.60E-07 | 1.00E-07 | 1.00E-07 |
| Cd | 1.00E-08 | 3.00E-08 | 4.00E-08 | 3.50E-08 | 6.90E-07 | 4.20E-07 | 3.50E-07 | 8.00E-09 |
| In | 1.50E-09 | 2.00E-08 | 2.00E-08 | 2.00E-08 | 8.00E-08 | 5.00E-08 | 3.20E-08 | 2.50E-08 |

| | | | | | | | | |
|----|----------|----------|----------|----------|----------|----------|----------|----------|
| Sn | 3.50E-07 | 5.40E-07 | | 2.70E-07 | 1.70E-06 | 7.90E-07 | 6.80E-07 | 8.90E-07 |
| Sb | 6.60E-08 | 7.80E-08 | 7.50E-08 | 7.65E-08 | 1.35E-07 | 1.30E-07 | 8.50E-08 | 1.10E-07 |
| Te | 5.20E-07 | 4.60E-07 | 3.80E-07 | 4.20E-07 | 2.30E-06 | 1.30E-06 | 1.00E-06 | 9.50E-07 |
| I | 6.00E-08 | 7.00E-08 | | 3.50E-08 | 4.30E-07 | 2.70E-07 | 2.00E-07 | 2.00E-07 |
| Cs | 2.00E-07 | 5.00E-07 | 1.50E-07 | 3.25E-07 | 1.90E-07 | 1.10E-07 | 9.00E-08 | 8.00E-08 |
| Ba | 4.40E-06 | 4.10E-06 | 4.00E-06 | 4.05E-06 | 2.35E-06 | 3.10E-06 | 4.55E-06 | 4.30E-06 |
| La | 3.01E-07 | 3.18E-07 | 3.30E-07 | 3.24E-07 | 2.35E-07 | 3.20E-07 | 4.69E-07 | 3.80E-07 |
| Ce | 7.63E-07 | 9.70E-07 | 8.80E-07 | 9.25E-07 | 6.20E-07 | 9.40E-07 | 1.19E-06 | 1.14E-06 |
| Pr | 1.20E-07 | 1.40E-07 | 1.30E-07 | 1.35E-07 | 9.40E-08 | 1.37E-07 | 1.74E-07 | 1.40E-07 |
| Nd | 5.81E-07 | 7.00E-07 | 6.50E-07 | 6.75E-07 | 4.60E-07 | 6.26E-07 | 9.19E-07 | 8.50E-07 |
| Sm | 1.94E-07 | 2.03E-07 | 2.05E-07 | 2.04E-07 | 1.50E-07 | 2.04E-07 | 2.94E-07 | 2.50E-07 |
| Eu | 7.40E-08 | 8.00E-08 | 7.80E-08 | 7.90E-08 | 5.70E-08 | 7.80E-08 | 1.05E-07 | 9.60E-08 |
| Gd | 2.75E-07 | 3.17E-07 | 2.90E-07 | 3.04E-07 | 2.00E-07 | 2.90E-07 | 4.05E-07 | 3.90E-07 |
| Tb | 4.90E-08 | 5.90E-08 | 5.40E-08 | 5.65E-08 | 3.70E-08 | 5.10E-08 | 7.10E-08 | 6.00E-08 |
| Dy | 3.05E-07 | 3.72E-07 | 3.60E-07 | 3.66E-07 | 2.50E-07 | 3.32E-07 | 4.54E-07 | 4.20E-07 |
| Ho | 7.40E-08 | 8.90E-08 | 8.20E-08 | 8.55E-08 | 5.60E-08 | 7.70E-08 | 9.70E-08 | 9.60E-08 |
| Er | 2.13E-07 | 2.52E-07 | 2.40E-07 | 2.46E-07 | 1.60E-07 | 2.21E-07 | 2.77E-07 | 3.05E-07 |
| Tm | 3.30E-08 | 3.80E-08 | 3.50E-08 | 3.65E-08 | 2.50E-08 | 3.50E-08 | 4.80E-08 | 4.00E-08 |
| Yb | 2.03E-07 | 2.26E-07 | 2.30E-07 | 2.28E-07 | 1.60E-07 | 2.15E-07 | 3.12E-07 | 2.70E-07 |
| Lu | 3.30E-08 | 3.40E-08 | 3.40E-08 | 3.40E-08 | 2.50E-08 | 3.30E-08 | 4.60E-08 | 3.90E-08 |
| Hf | 1.50E-07 | 1.70E-07 | 1.70E-07 | 1.70E-07 | 1.05E-07 | 1.80E-07 | 2.30E-07 | 2.20E-07 |
| Ta | 2.10E-08 | 2.10E-08 | | 1.05E-08 | 1.40E-08 | 1.90E-08 | | |
| W | 1.64E-07 | 1.38E-07 | 1.15E-07 | 1.27E-07 | 9.30E-08 | 1.60E-07 | 1.60E-07 | 1.50E-07 |
| Re | 7.80E-08 | 4.70E-08 | 3.20E-08 | 3.95E-08 | 3.80E-08 | 5.00E-08 | 5.70E-08 | 5.80E-08 |
| Os | 8.35E-07 | 5.30E-07 | 4.10E-07 | 4.70E-07 | 4.90E-07 | 6.70E-07 | 8.00E-07 | 8.05E-07 |
| Ir | 7.70E-07 | 4.90E-07 | 3.80E-07 | 4.35E-07 | 4.65E-07 | 5.80E-07 | 7.30E-07 | 7.40E-07 |
| Pt | 1.58E-06 | 1.09E-06 | 8.80E-07 | 9.85E-07 | 1.00E-06 | 1.10E-06 | 1.25E-06 | 1.24E-06 |
| Au | 2.20E-07 | 1.56E-07 | 1.46E-07 | 1.51E-07 | 1.45E-07 | 1.50E-07 | 1.53E-07 | 1.90E-07 |
| Hg | | 3.00E-08 | 2.20E-08 | 2.60E-08 | 3.10E-07 | | | |
| Tl | 1.00E-09 | 5.00E-09 | 3.00E-08 | 1.75E-08 | 1.42E-07 | 9.20E-08 | 5.80E-08 | 4.00E-08 |
| Pb | 2.40E-07 | 4.00E-08 | | 2.00E-08 | 2.50E-06 | 1.60E-06 | 1.10E-06 | 2.15E-06 |
| Bi | 1.00E-08 | 1.40E-08 | 3.00E-08 | 2.20E-08 | 1.10E-07 | 7.10E-08 | 5.40E-08 | 3.50E-08 |
| Th | 3.80E-08 | 4.20E-08 | 4.70E-08 | 4.45E-08 | 2.90E-08 | 4.10E-08 | 5.80E-08 | 8.00E-08 |
| U | 1.30E-08 | 1.50E-08 | 1.50E-08 | 1.50E-08 | 8.00E-09 | 1.20E-08 | 1.70E-08 | 1.80E-08 |

Table 2: Elemental mass fractions of different chondrite groups

A.2 Elemental market price

| | Market price (\$/kg) | Source | Date | Notes |
|----|----------------------|--------|---------------|---------------------|
| Li | 104.76 | [54] | 12/6/2019 | |
| Be | 830.88 | [54] | 12/6/2019 | |
| B | 0.39 | [55] | February 2019 | For borate products |
| C | 0.43 | [55] | February 2019 | For graphite |
| N | 2.77 | | | |
| O | 0.64 | | | |
| F | 270.00 | [55] | February 2019 | For fluorspar |

| | | | | |
|----|------------|------|---------------|-----------------------|
| Na | 3.14 | [54] | 12/6/2019 | |
| Mg | 2.49 | [54] | 12/6/2019 | |
| Al | 2.03 | [54] | 12/6/2019 | |
| Si | 2.01 | [54] | 12/6/2019 | For Si #2202 |
| P | 300.00 | | | |
| S | 0.07 | [55] | February 2019 | |
| Cl | 1.50 | | | |
| K | 13.01 | [54] | 12/6/2019 | |
| Ca | 6.43 | [54] | 12/6/2019 | |
| Sc | 15,000.00 | [55] | January 2018 | In 5g samples |
| Ti | 10.12 | [54] | 12/6/2019 | |
| V | 390.15 | [54] | 12/6/2019 | |
| Cr | 9.39 | [54] | 12/6/2019 | |
| Mn | 2.13 | [54] | 12/6/2019 | |
| Fe | 0.60 | [54] | 12/6/2019 | For cold-rolled steel |
| Co | 35.76 | [54] | 12/6/2019 | |
| Ni | 14.26 | [54] | 12/6/2019 | |
| Cu | 6.74 | [54] | 12/6/2019 | |
| Zn | 3.05 | [54] | 12/6/2019 | |
| Ga | 140.89 | [54] | 12/6/2019 | |
| Ge | 1,076.53 | [54] | 12/6/2019 | |
| As | 1.37 | [54] | 12/6/2019 | |
| Se | 23.84 | [54] | 12/6/2019 | |
| Br | 4.90 | [55] | June 2018 | |
| Rb | 15,460.00 | [55] | February 2019 | |
| Sr | 6.21 | [55] | June 2018 | |
| Y | 32.51 | [54] | 12/6/2019 | |
| Zr | 36.13 | [54] | 12/6/2019 | |
| Nb | 89.59 | [54] | 12/6/2019 | |
| Mo | 40.17 | [54] | 12/6/2019 | |
| Ru | 10,765.25 | [54] | 12/6/2019 | |
| Rh | 116,250.25 | [54] | 12/6/2019 | |
| Pd | 50,719.50 | [54] | 12/6/2019 | |
| Ag | 513.12 | [54] | 12/6/2019 | |
| Cd | 2.87 | [54] | 12/6/2019 | |
| In | 156.06 | [54] | 12/6/2019 | |
| Sn | 20.88 | [54] | 12/6/2019 | |
| Sb | 5.82 | [54] | 12/6/2019 | |
| Te | 59.25 | [54] | 12/6/2019 | |
| I | 22.00 | [55] | February 2019 | |
| Cs | 78,700.00 | [55] | February 2019 | |
| Ba | 0.18 | [55] | February 2019 | For barium sulphate |
| La | 5.13 | [54] | 12/6/2019 | |
| Ce | 4.99 | [54] | 12/6/2019 | |
| Pr | 102.60 | [54] | 12/6/2019 | |
| Nd | 66.11 | [54] | 12/6/2019 | |
| Sm | 1.81 | [54] | 12/6/2019 | For samarium oxide |
| Eu | 33.24 | [54] | 12/6/2019 | For europium oxide |
| Gd | 29.62 | [54] | 12/6/2019 | For gadolinium oxide |

| | | | | |
|----|-----------|------|---------------|--------------------|
| Tb | 722.50 | [54] | 12/6/2019 | |
| Dy | 346.80 | [54] | 12/6/2019 | |
| Ho | 58.52 | [54] | 12/6/2019 | For holmium oxide |
| Er | 27.09 | [54] | 12/6/2019 | For erbium oxide |
| Hf | 775.00 | [55] | February 2019 | |
| Ta | 218.00 | [55] | February 2019 | For tantalum oxide |
| W | 36.49 | [54] | 12/6/2019 | |
| Re | 4,190.50 | [54] | 12/6/2019 | |
| Os | 5,888.89 | [55] | November 2018 | |
| Ir | 55,849.25 | [54] | 12/6/2019 | |
| Pt | 27,455.00 | [54] | 12/6/2019 | |
| Au | 43,224.29 | [54] | 12/6/2019 | |
| Hg | 81.22 | [55] | February 2019 | |
| Tl | 4,000.00 | [55] | February 2019 | |
| Pb | 2.33 | [54] | 12/6/2019 | |
| Bi | 6.14 | [54] | 12/6/2019 | |
| Th | 176.00 | | | |
| U | 52.91 | | | |

Table 3: Market price of the different studied chemical elements

A.3 Asteroid total economic sizes

| Asteroid | Chondrite Type | Source | Mass (kg) | Source | Value (\$) |
|-------------------|----------------|--------|-----------|--------|----------------------------|
| (19) Fortuna | CM | [7] | 9.03E+18 | [8] | 17,952,660,131,558,000,000 |
| (23) Thalia | H | [59] | 1.96E+18 | [9] | 4,456,892,820,224,430,000 |
| (41) Daphne | CM | [8] | 6.10E+18 | [8] | 12,127,489,125,415,700,000 |
| (78) Diana | CM | [9] | 8.99E+17 | [8] | 1,787,313,561,270,280,000 |
| (87) Sylvia | CM | [60] | 1.48E+19 | [5] | 29,073,196,487,665,100,000 |
| (93) Minerva | CO | [34] | 3.35E+18 | [30] | 7,330,792,621,362,170,000 |
| (117) Lomia | CV | [9] | 6.08E+18 | [66] | 13,233,302,316,286,100,000 |
| (121) Hermione | CM | [13] | 4.94E+18 | [8] | 9,821,278,078,615,320,000 |
| (130) Elektra | CM | [14] | 6.20E+18 | [8] | 12,326,300,422,553,600,000 |
| (253) Mathilde | CM | [61] | 1.03E+17 | [63] | 204,775,636,052,101,000 |
| (259) Aletheia | CV | [9] | 7.79E+18 | [66] | 16,955,168,592,741,500,000 |
| (324) Bamberga | CM | [24] | 1.03E+19 | [9] | 20,477,563,605,210,100,000 |
| (372) Palma | CV | [9] | 5.15E+18 | [9] | 11,209,129,429,091,000,000 |
| (433) Eros | LL | [18] | 6.69E+17 | [64] | 13,904,608,493,757,100 |
| (442) Eichsfeldia | CM | [9] | 2.50E+17 | [8] | 497,028,242,844,905,000 |
| (554) Peraga | CI | [12] | 5.86E+17 | [8] | 1,045,542,093,710,350,000 |
| (617) Patroclus | CV | [9] | 1.36E+18 | [29] | 2,960,080,781,274,510,000 |
| (654) Zelinda | CM | [9] | 1.22E+18 | [8] | 2,425,497,825,083,140,000 |
| (704) Interamnia | CI | [12] | 3.28E+19 | [9] | 58,521,810,023,377,800,000 |
| (751) Faina | CM | [13] | 3.67E+18 | [8] | 7,296,374,604,963,210,000 |
| (762) Pulcova | CM | [12] | 1.40E+18 | [31] | 2,783,358,159,931,470,000 |
| (1089) Tama | L/LL | [27] | 8.90E+14 | [6] | 1,886,230,501,622,000 |
| (1313) Berna | LL | [27] | 2.25E+15 | [6] | 4,678,535,832,354,350 |

| | | | | | |
|---------------------|----|------|----------|------|-----------------------|
| (1620) Geographos | LL | [18] | 1.48E+13 | [45] | 30,774,369,030,598 |
| (1627) Ivar | LL | [18] | 5.64E+14 | [16] | 1,171,962,829,258,470 |
| (1862) Apollo | LL | [18] | 5.68E+12 | [52] | 11,810,703,790,121 |
| (3671) Dionysus | CM | [15] | 8.38E+11 | [49] | 1,666,038,670,016 |
| (3749) Balam | L | [27] | 5.10E+14 | [32] | 1,060,468,122,000,320 |
| (4179) Toutatis | L | [28] | 5.00E+13 | [28] | 110,740,457,809,329 |
| (25143) Itokawa | LL | [1] | 3.58E+10 | [2] | 74,440,703,466 |
| (65803) Didymos | L | [28] | 5.28E+11 | [51] | 1,168,976,272,635 |
| (66063) 1998 RO1 | L | [3] | 3.60E+11 | [9] | 797,331,296,227 |
| (66391) Moshup | L | [50] | 2.49E+12 | [44] | 5,510,445,180,592 |
| (99942) Apophis | LL | [18] | 5.20E+10 | [39] | 108,126,161,459 |
| (101955) Bennu | CM | [22] | 7.80E+10 | [11] | 155,072,811,768 |
| (153591) 2001 SN263 | CI | [47] | 9.51E+12 | [20] | 16,972,716,583,969 |
| (175706) 1996 FG3 | CM | [17] | 3.54E+12 | [65] | 7,034,412,480,685 |
| (185851) 2000 DP107 | L | [46] | 4.83E+11 | [40] | 1,055,991,970,686 |
| (276049) 2002 CE26 | CM | [48] | 1.95E+13 | [53] | 38,768,202,941,903 |
| (311066) 2004 DC | CM | [9] | 3.59E+10 | [19] | 71,365,303,221 |
| (494658) 2000 UG11 | CM | [9] | 9.40E+09 | [33] | 18,688,261,931 |

Table 4: Total economic size of the target asteroids

B Economic distance

B.1 Optimal total Δv values

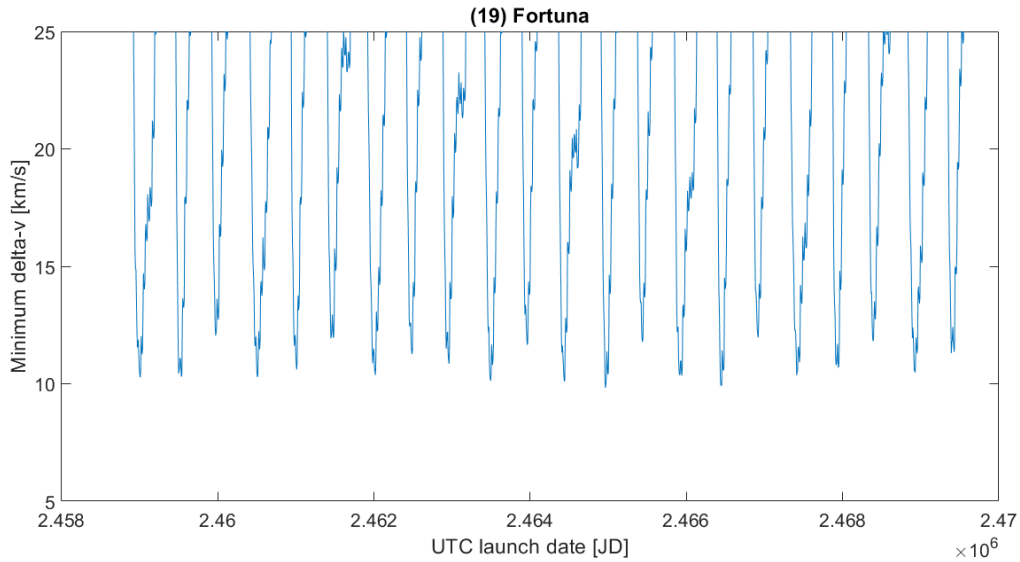


Figure 17: Optimal Δv values for (19) Fortuna

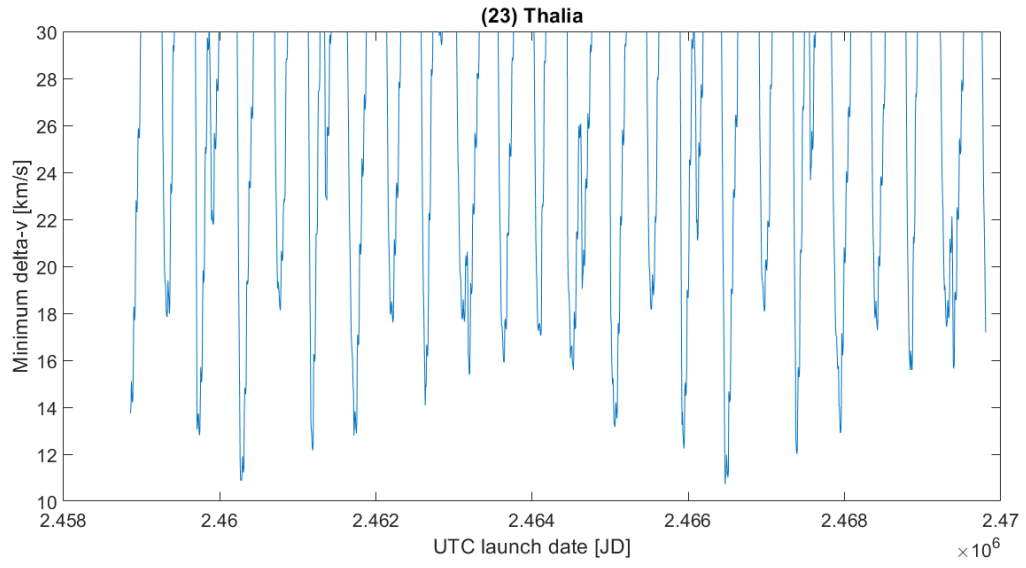


Figure 18: Optimal Δv values for (23) Thalia

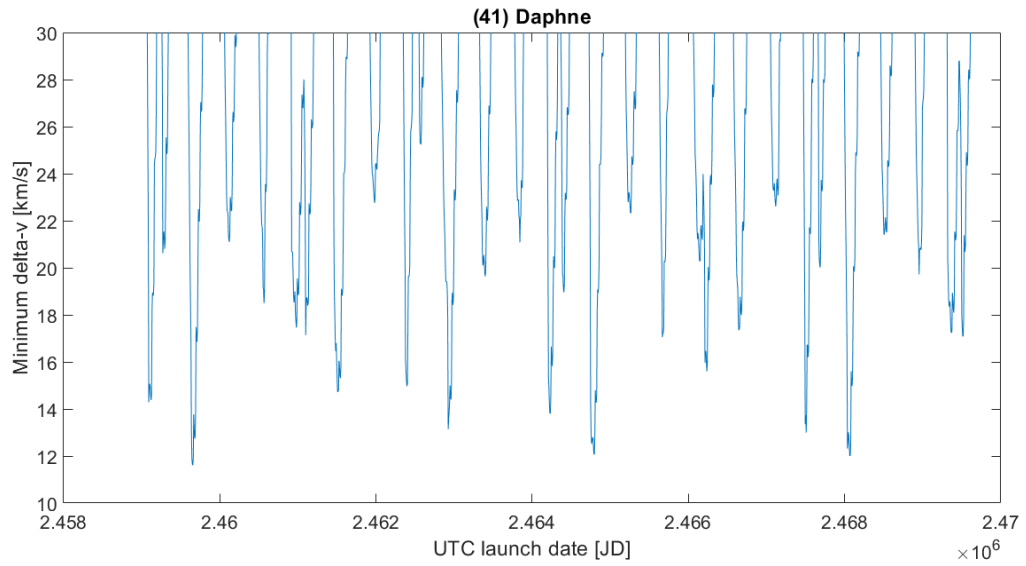


Figure 19: Optimal Δv values for (41) Daphne

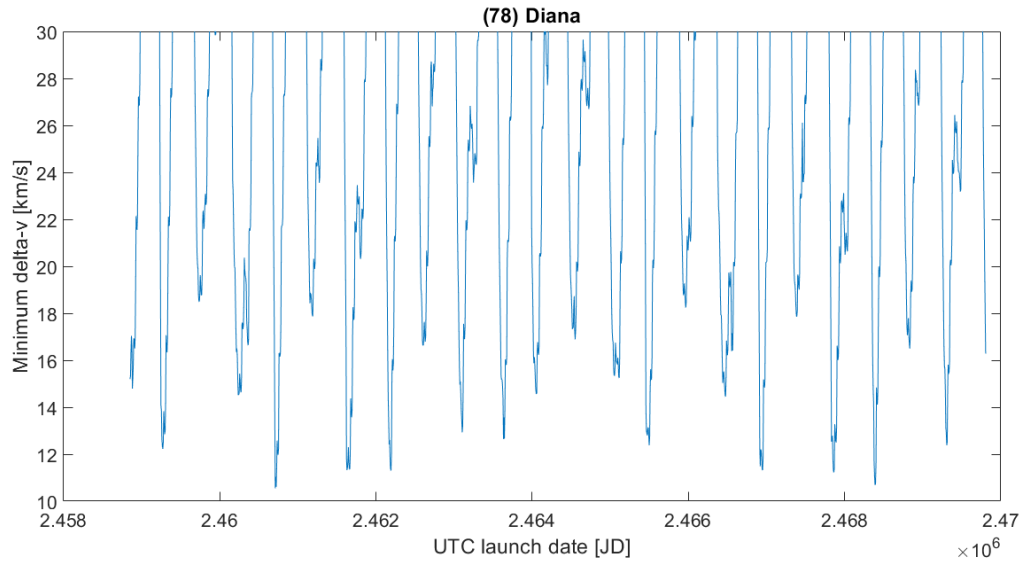


Figure 20: Optimal Δv values for (78) Diana

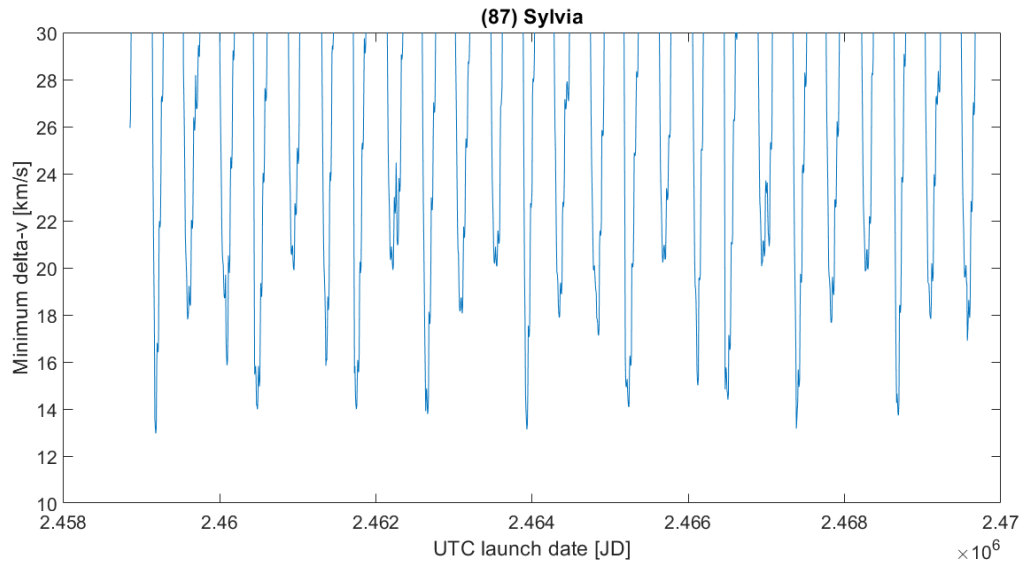


Figure 21: Optimal Δv values for (87) Sylvia

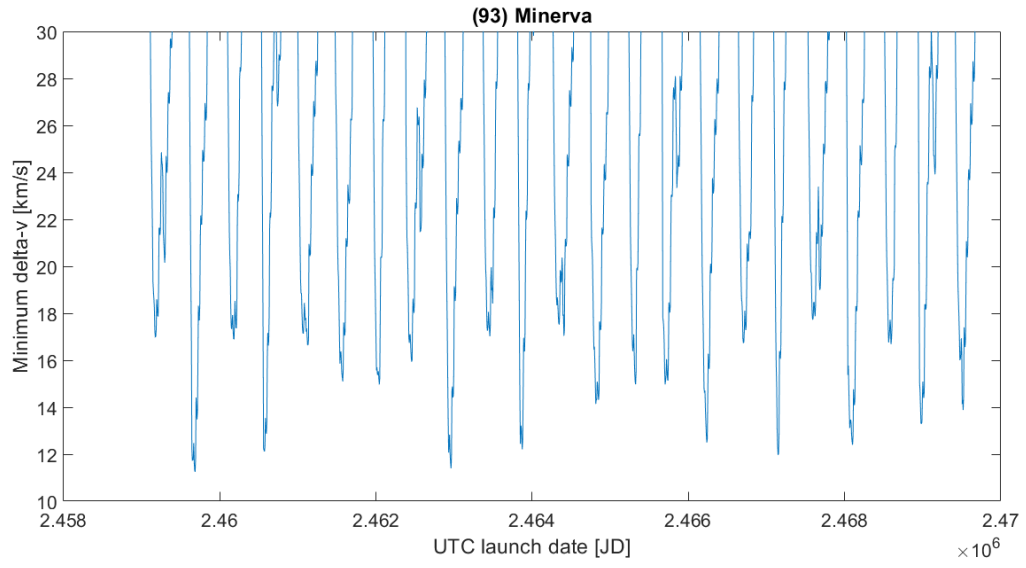


Figure 22: Optimal Δv values for (93) Minerva

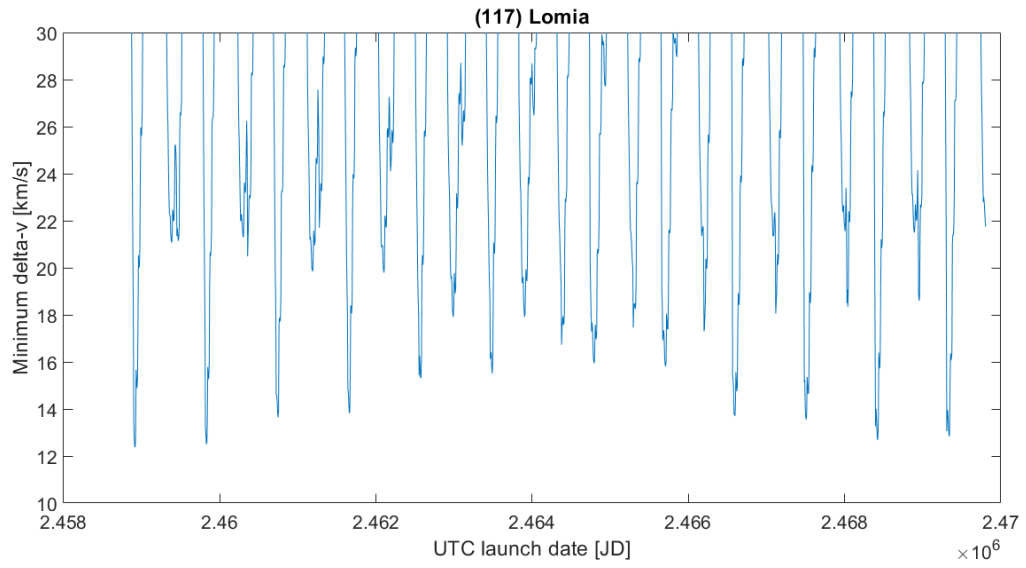


Figure 23: Optimal Δv values for (117) Lomia

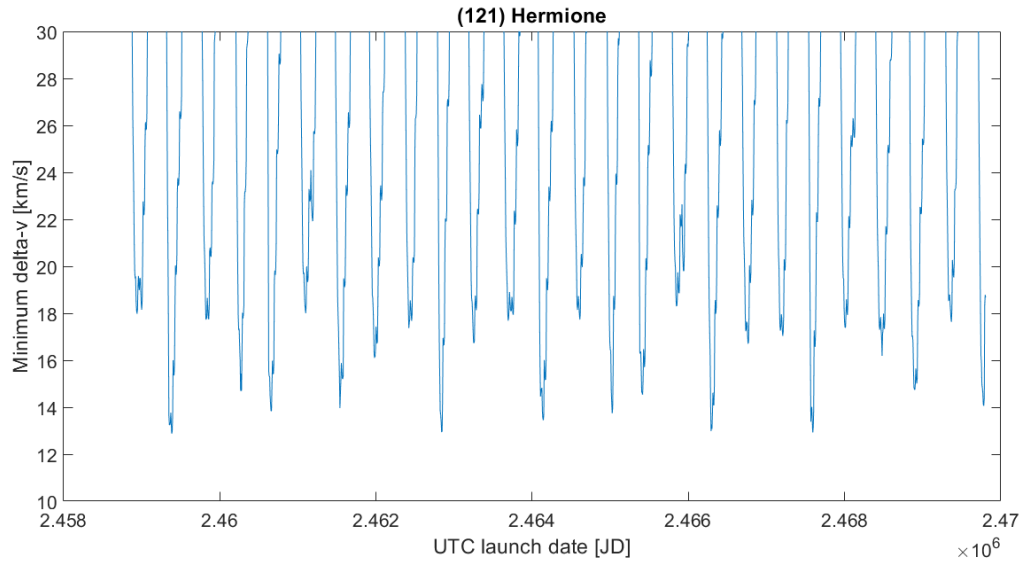


Figure 24: Optimal Δv values for (121) Hermione

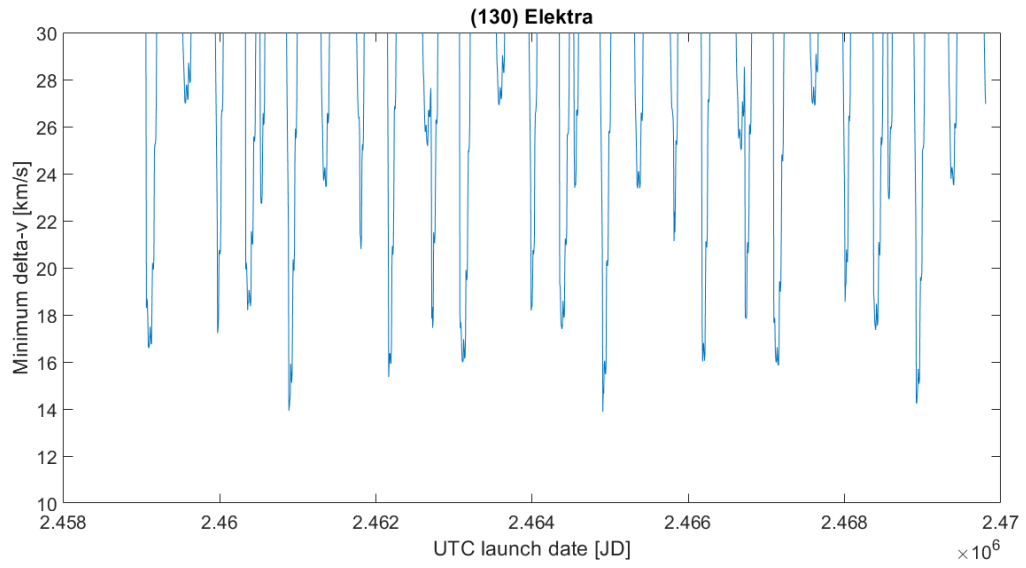


Figure 25: Optimal Δv values for (130) Elektra

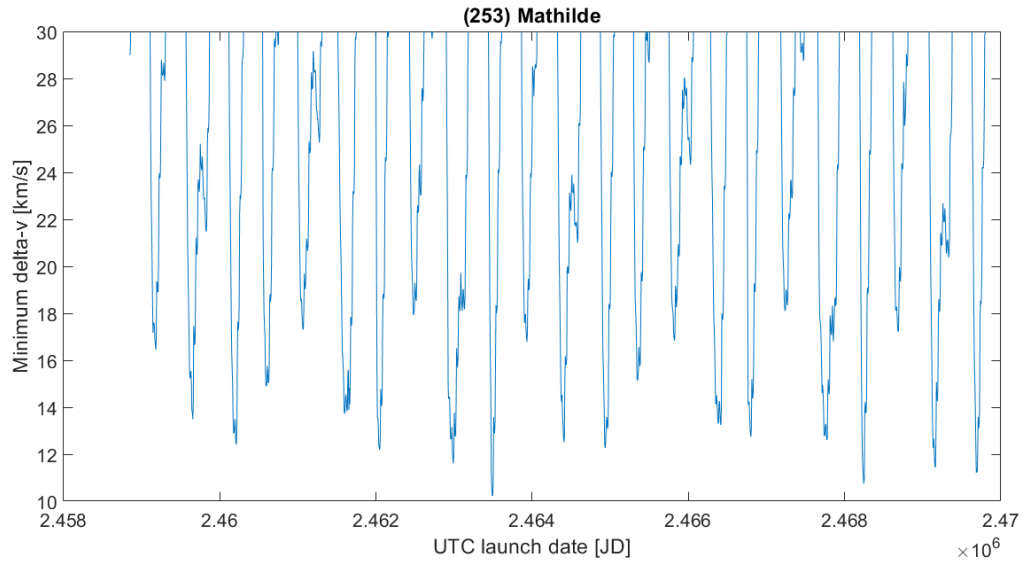


Figure 26: Optimal Δv values for (253) Mathilde

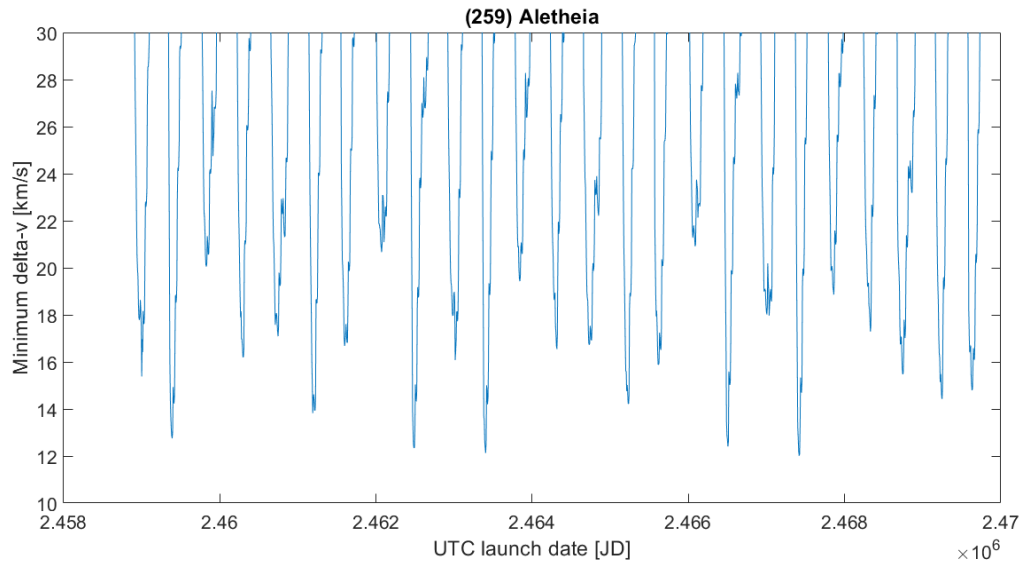


Figure 27: Optimal Δv values for (259) Aletheia

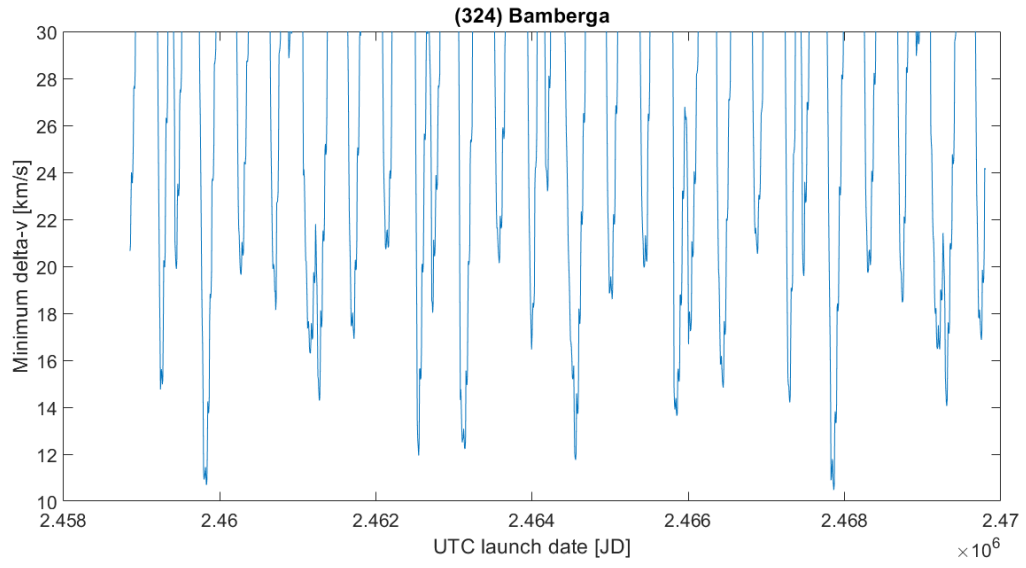


Figure 28: Optimal Δv values for (324) Bamberga

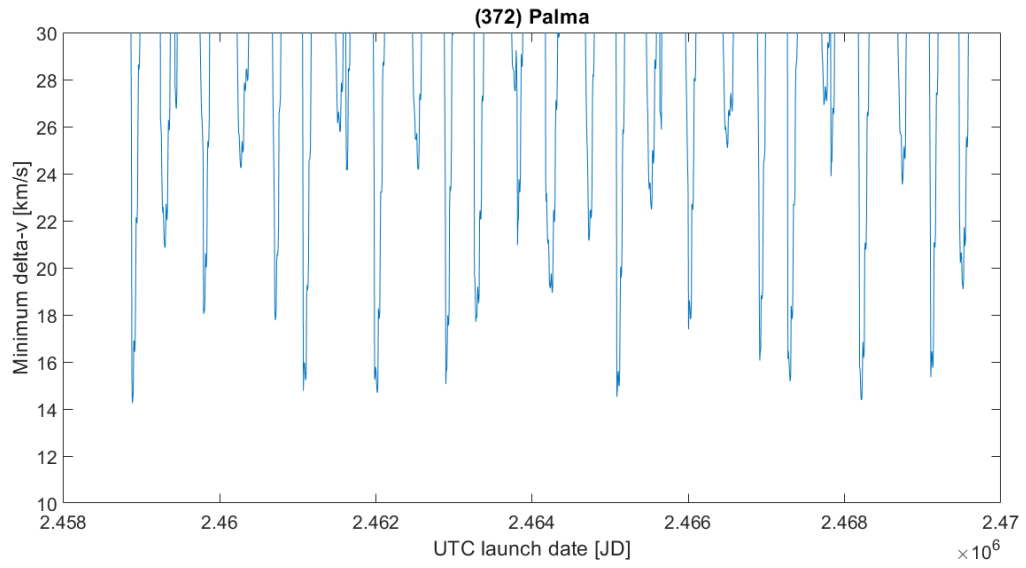


Figure 29: Optimal Δv values for (372) Palma

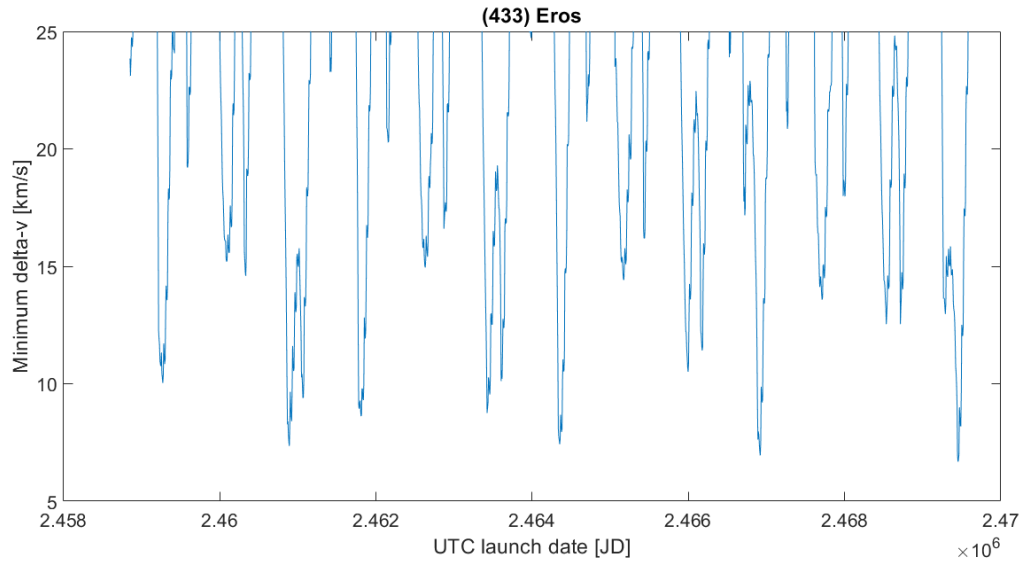


Figure 30: Optimal Δv values for (433) Eros

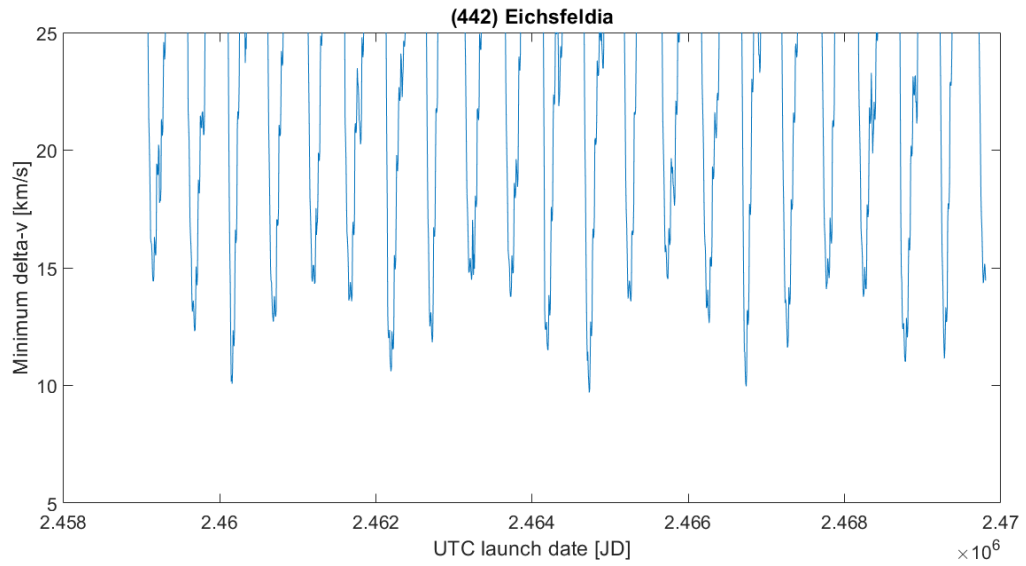


Figure 31: Optimal Δv values for (442) Eichsfeldia

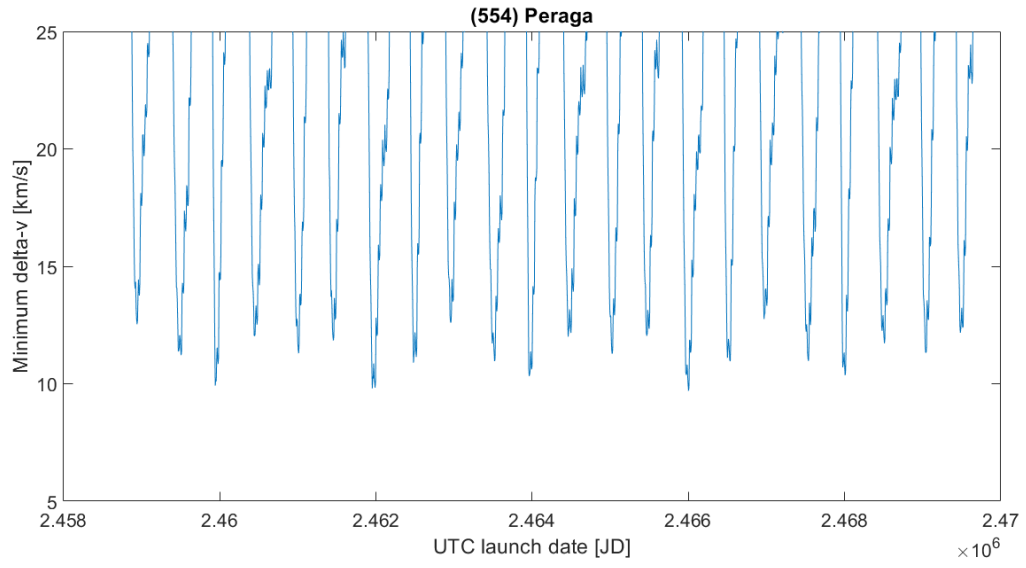


Figure 32: Optimal Δv values for (554) Peraga

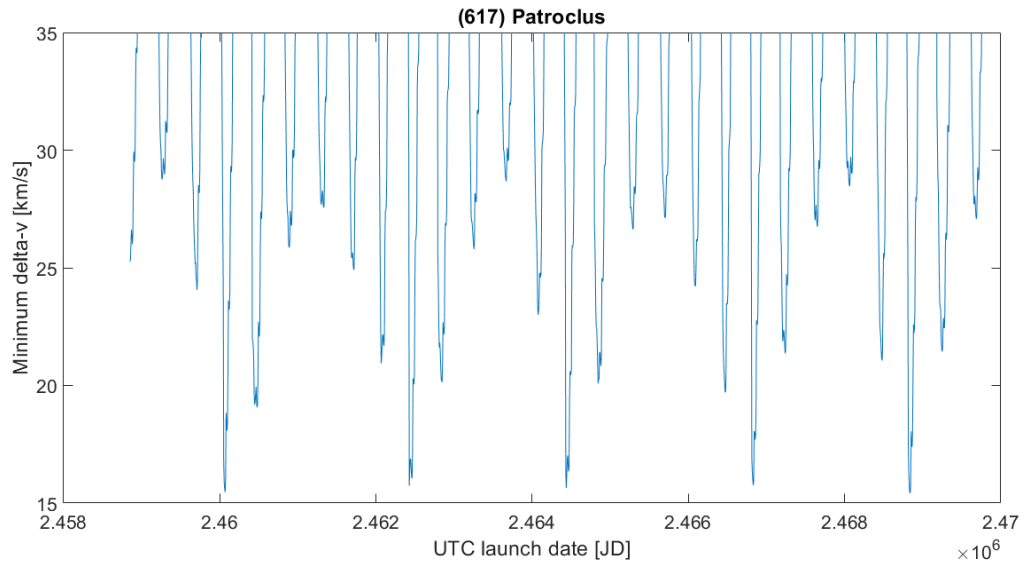


Figure 33: Optimal Δv values for (617) Patroclus

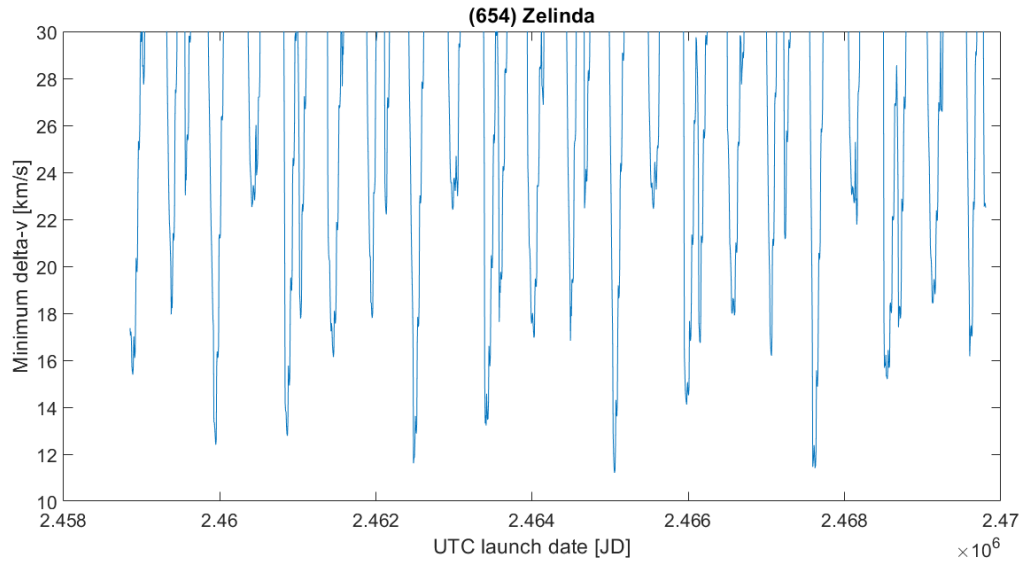


Figure 34: Optimal Δv values for (654) Zelinda

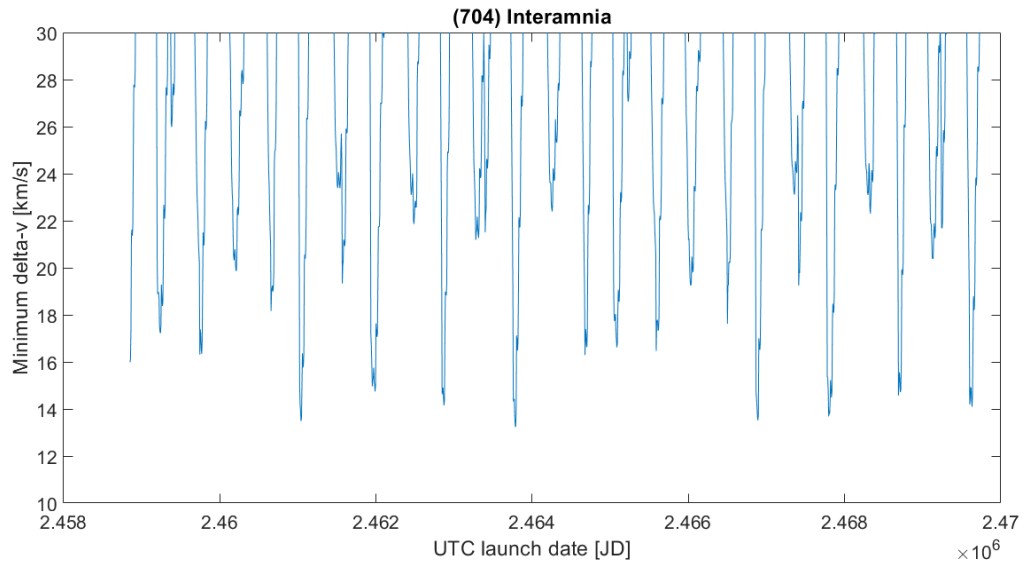


Figure 35: Optimal Δv values for (704) Interamnia

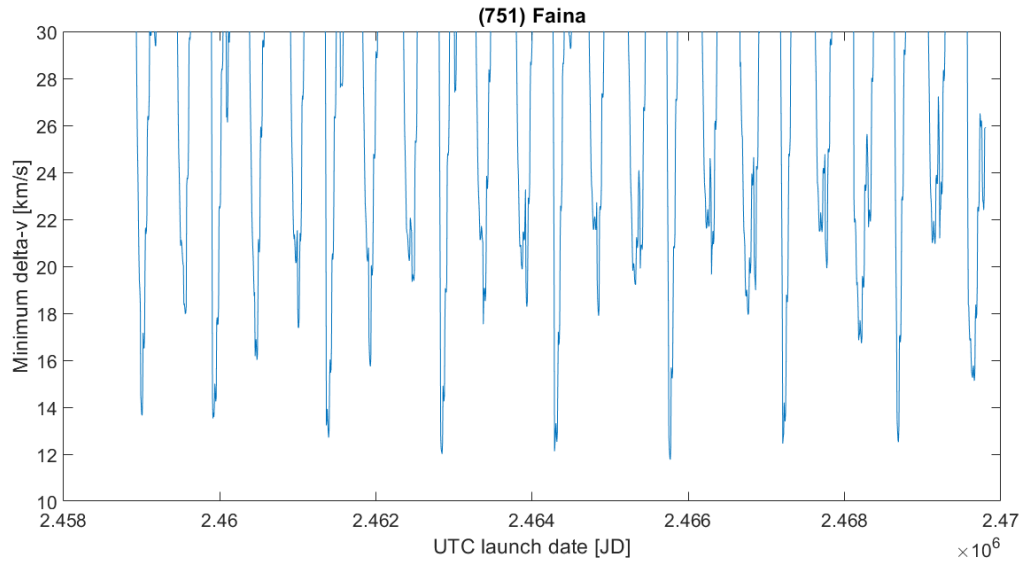


Figure 36: Optimal Δv values for (751) Faina

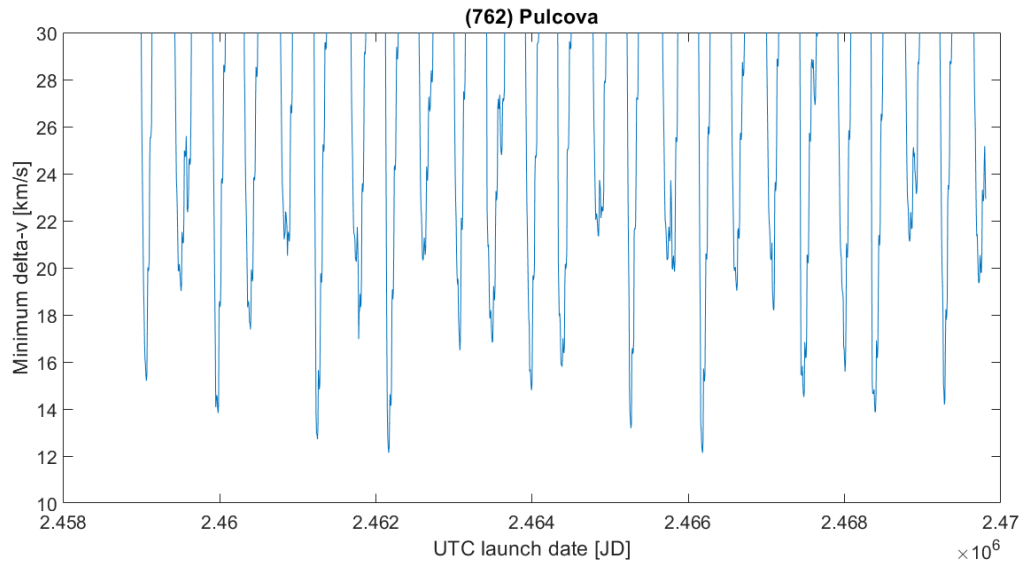


Figure 37: Optimal Δv values for (762) Pulcova

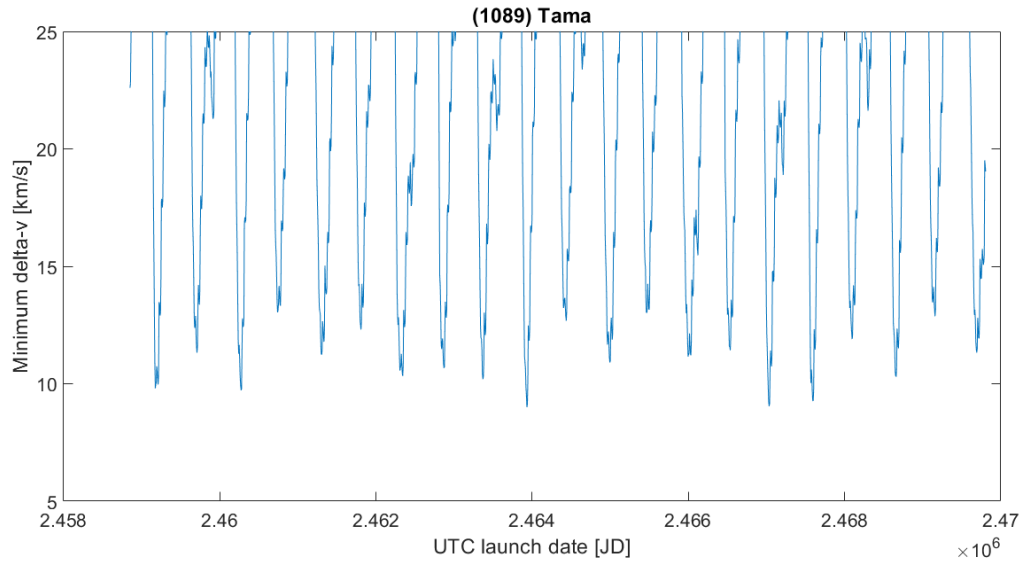


Figure 38: Optimal Δv values for (1089) Tama

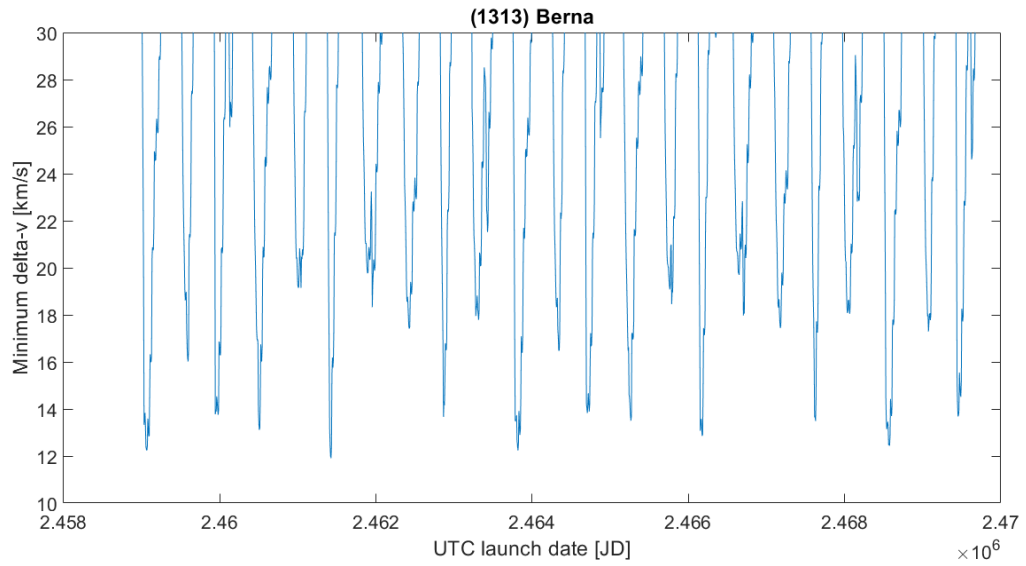


Figure 39: Optimal Δv values for (1313) Berna

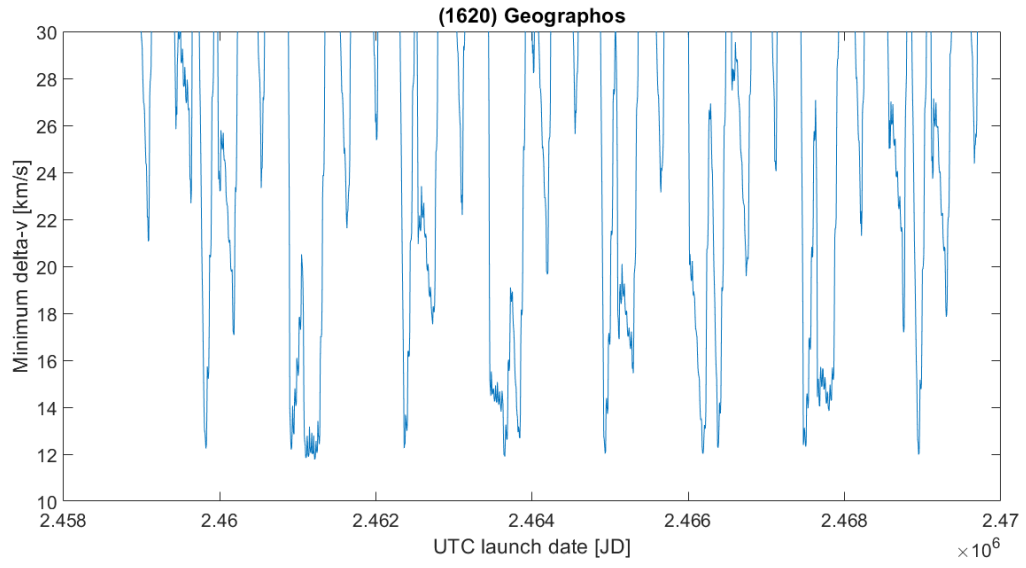


Figure 40: Optimal Δv values for (1620) Geographos

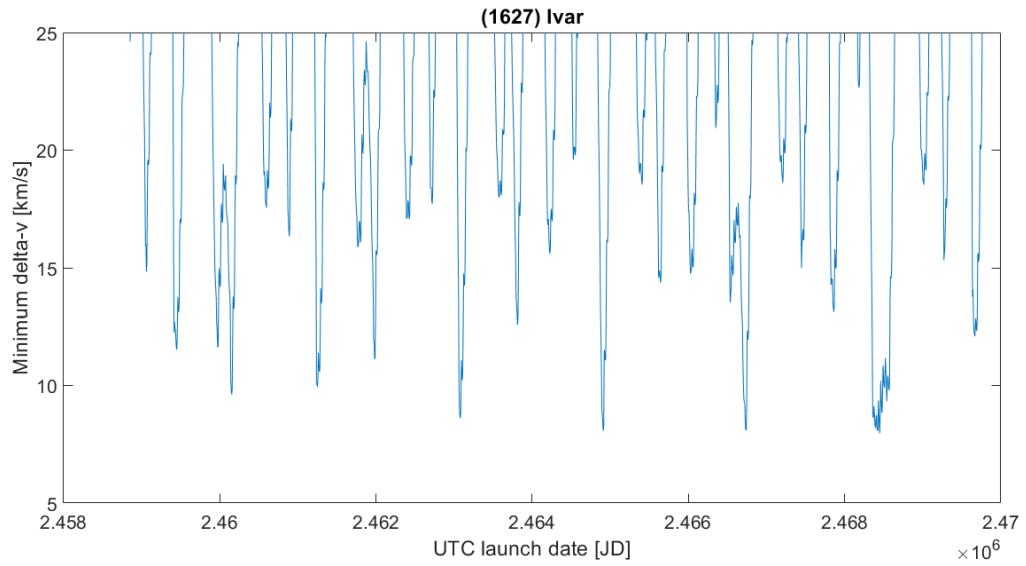


Figure 41: Optimal Δv values for (1627) Ivar

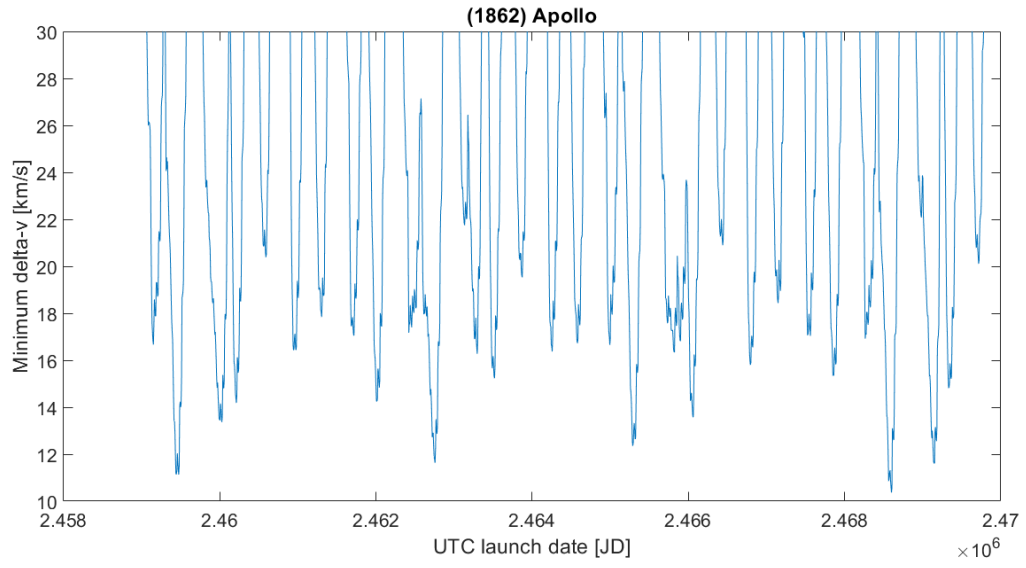


Figure 42: Optimal Δv values for (1862) Apollo

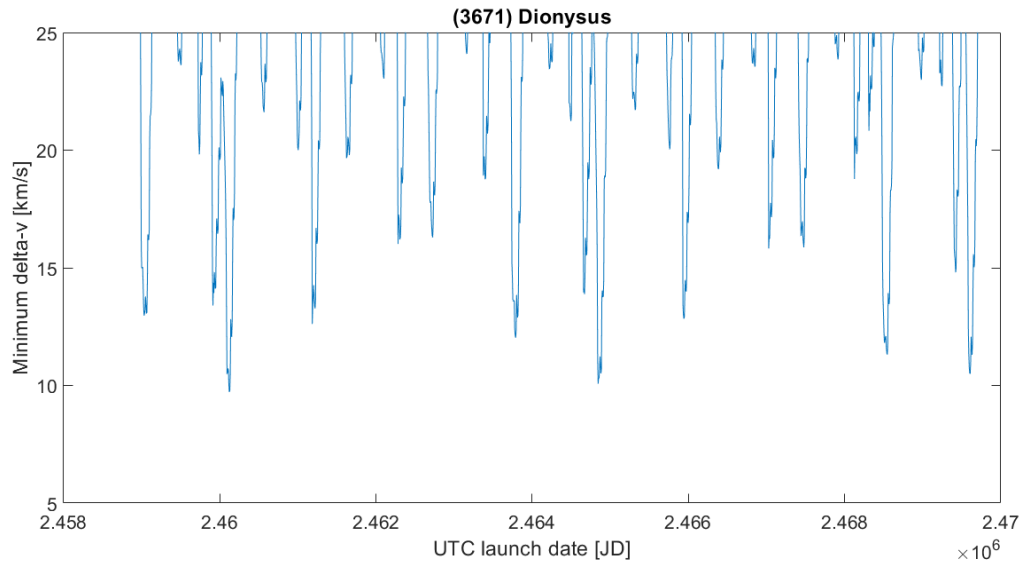


Figure 43: Optimal Δv values for (3671) Dionysus

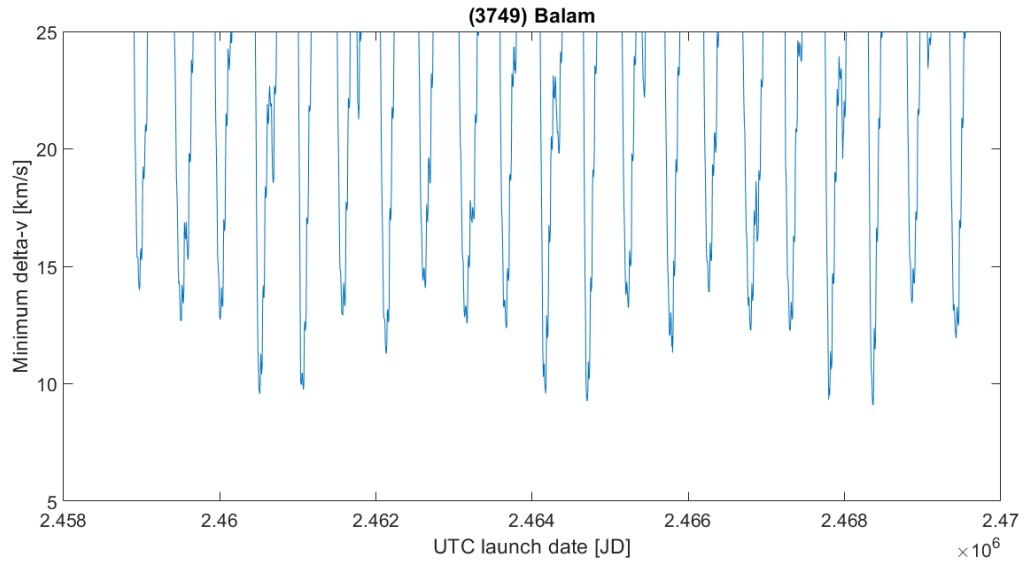


Figure 44: Optimal Δv values for (3749) Balam

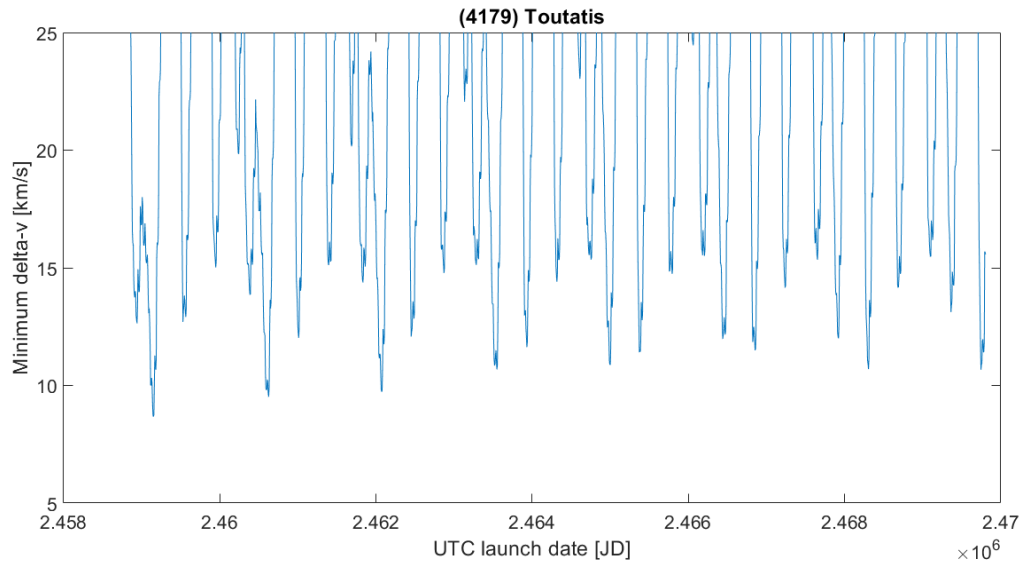


Figure 45: Optimal Δv values for (4179) Toutatis

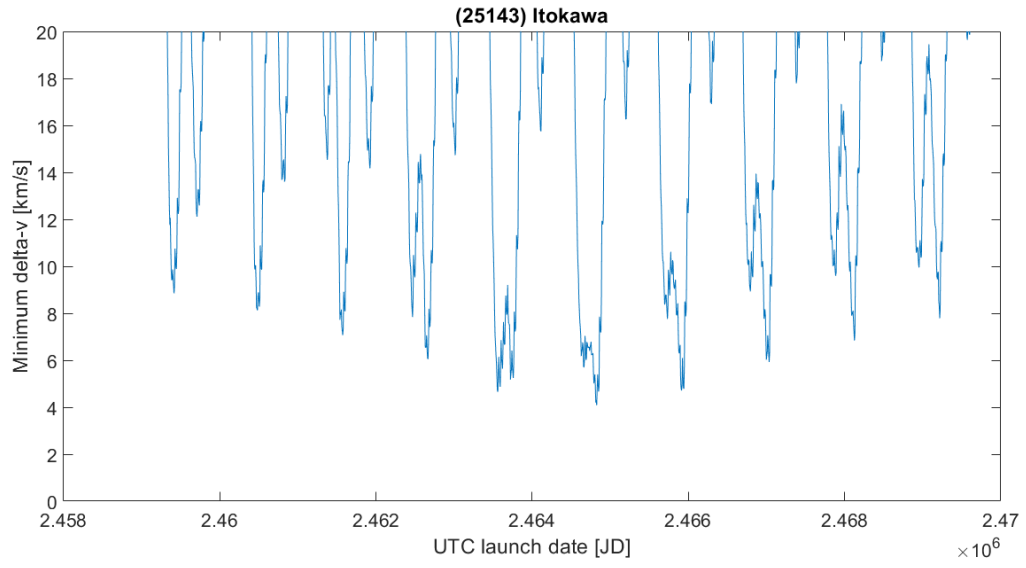


Figure 46: Optimal Δv values for (25143) Itokawa

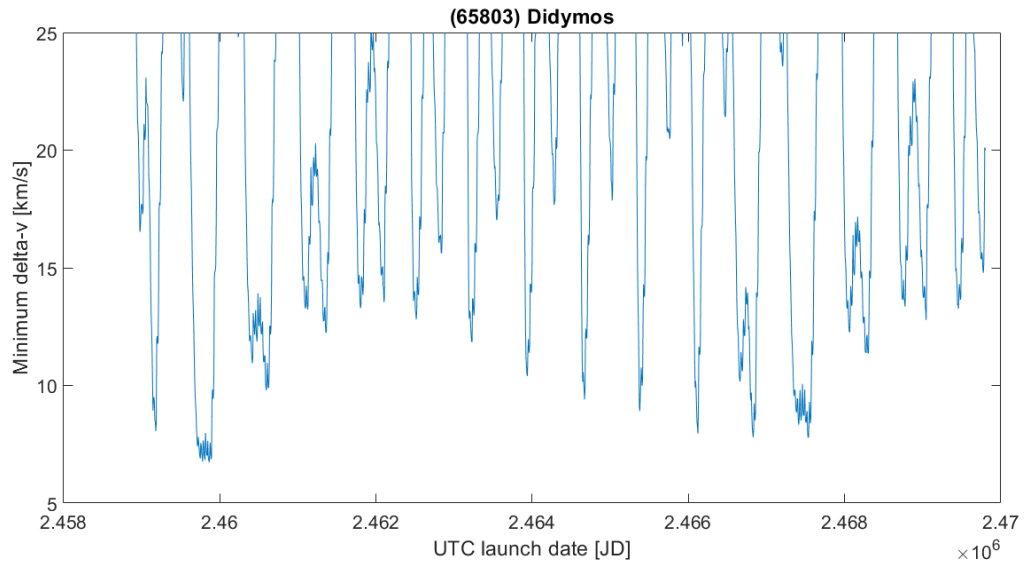


Figure 47: Optimal Δv values for (65803) Didymos

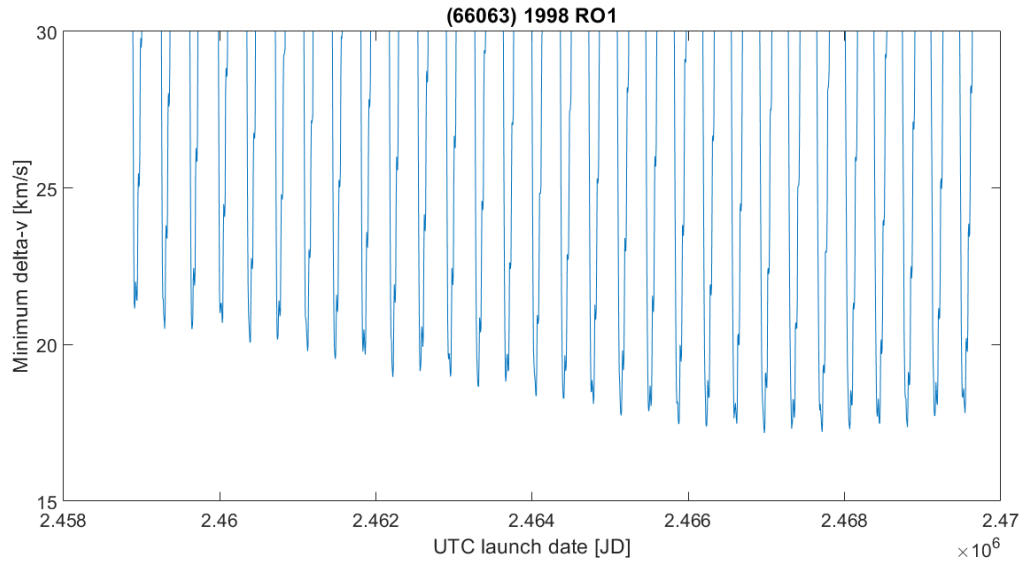


Figure 48: Optimal Δv values for (66063) 1998 RO1

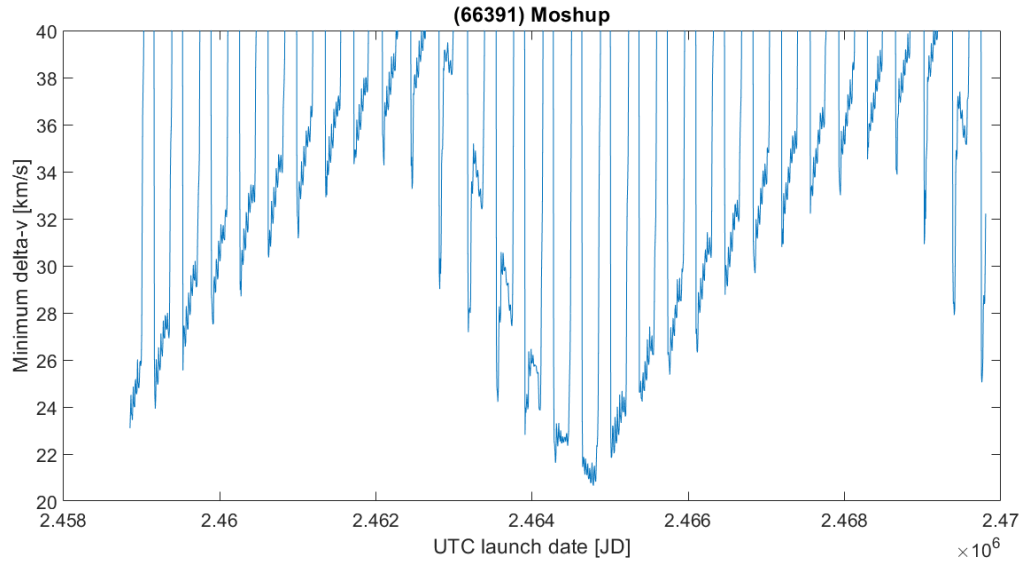


Figure 49: Optimal Δv values for (66391) Moshup

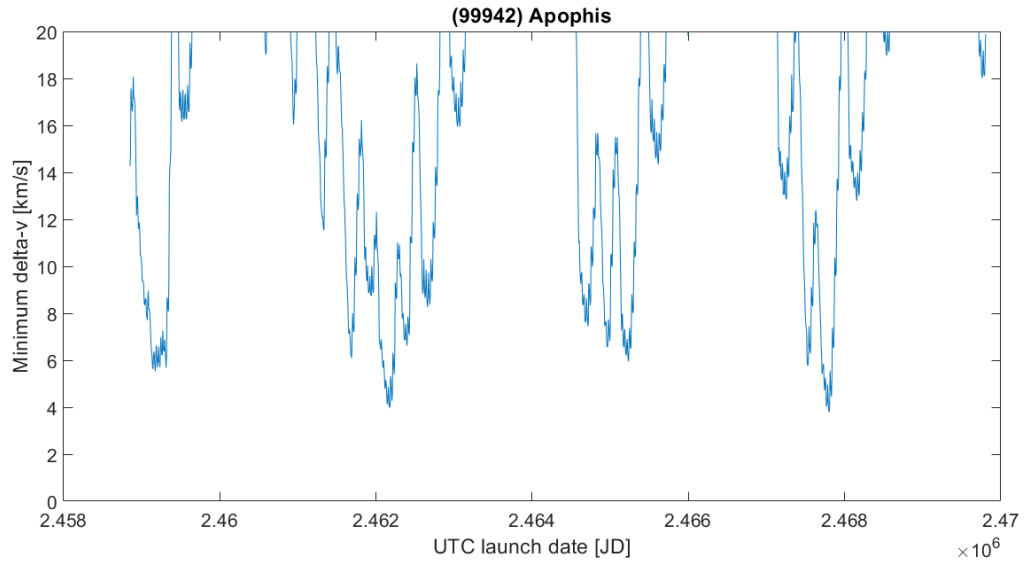


Figure 50: Optimal Δv values for (99942) Apophis

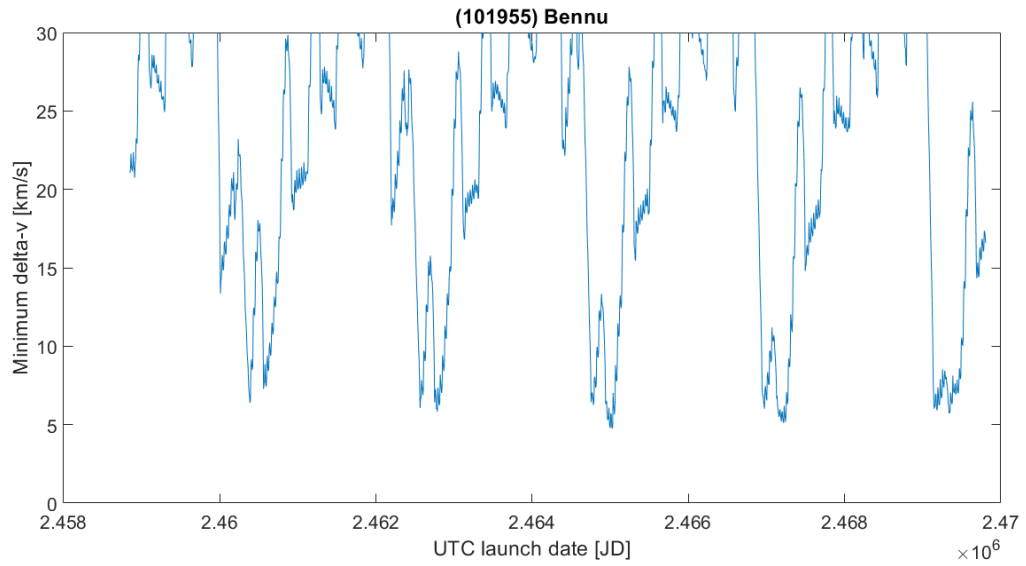


Figure 51: Optimal Δv values for (101955) Bennu

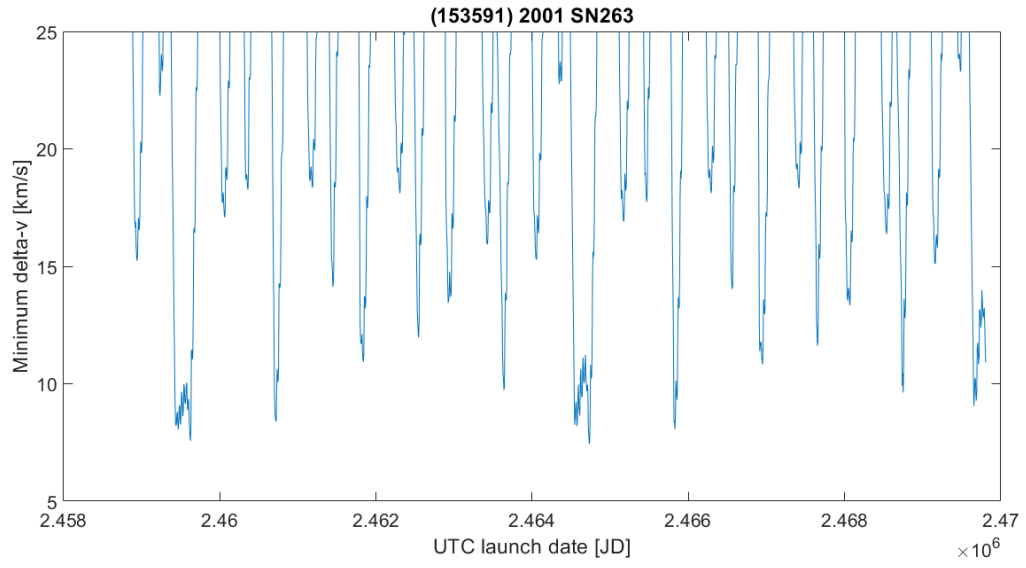


Figure 52: Optimal Δv values for (153591) 2001 SN263

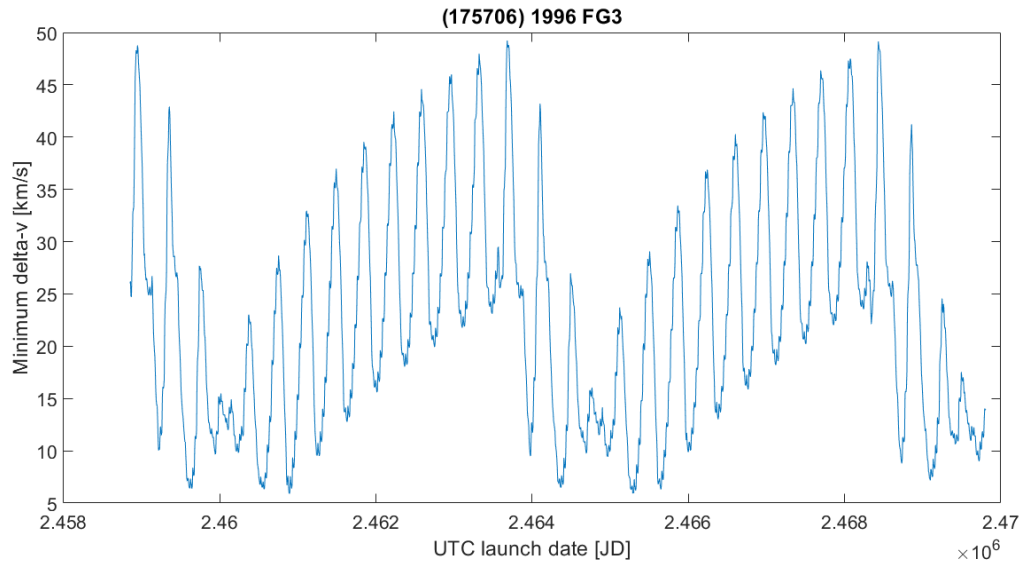


Figure 53: Optimal Δv values for (175706) 1996 FG3

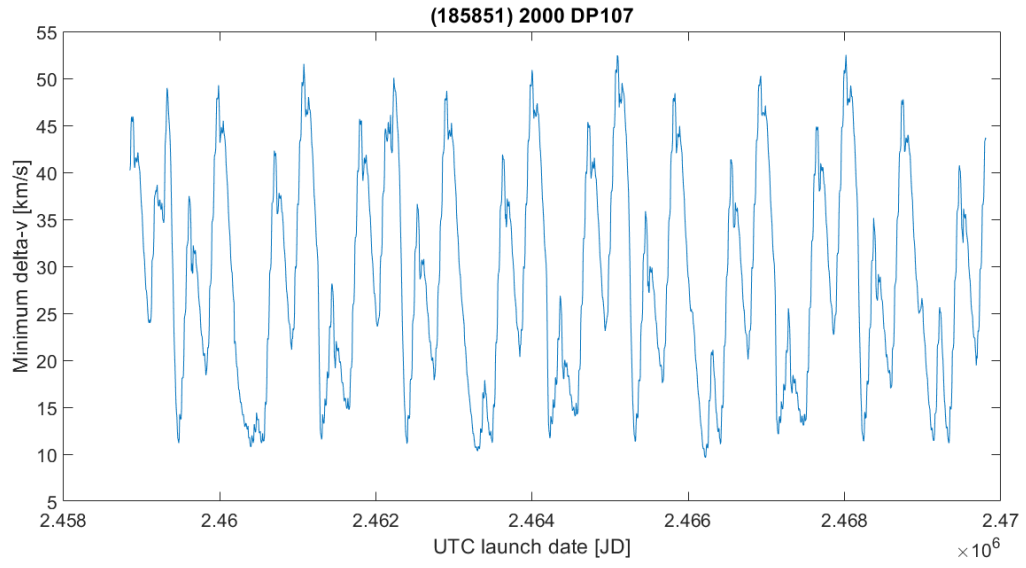


Figure 54: Optimal Δv values for (185851) 2000 DP107

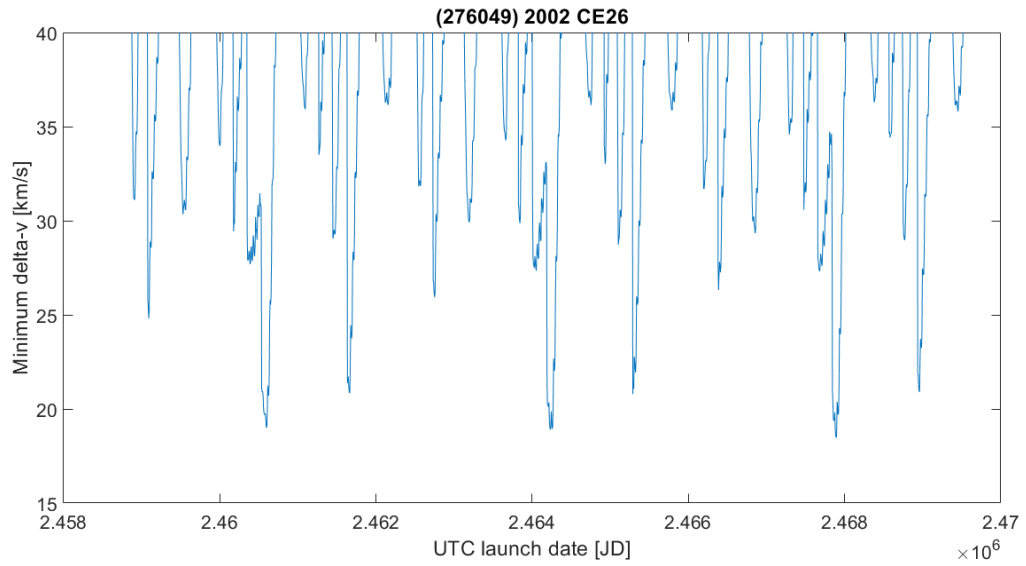


Figure 55: Optimal Δv values for (276049) 2002 CE26

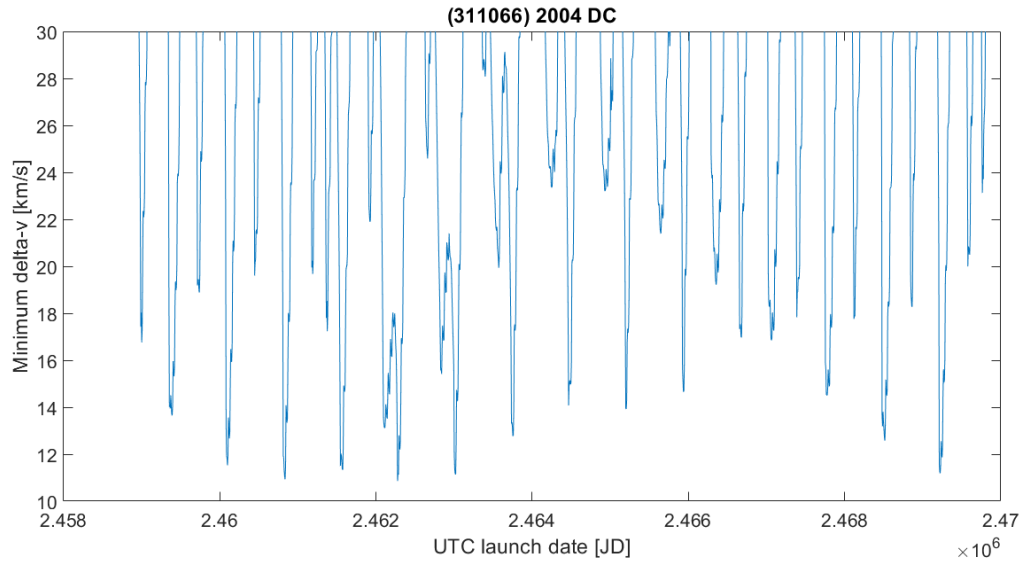


Figure 56: Optimal Δv values for (311066) 2004 DC

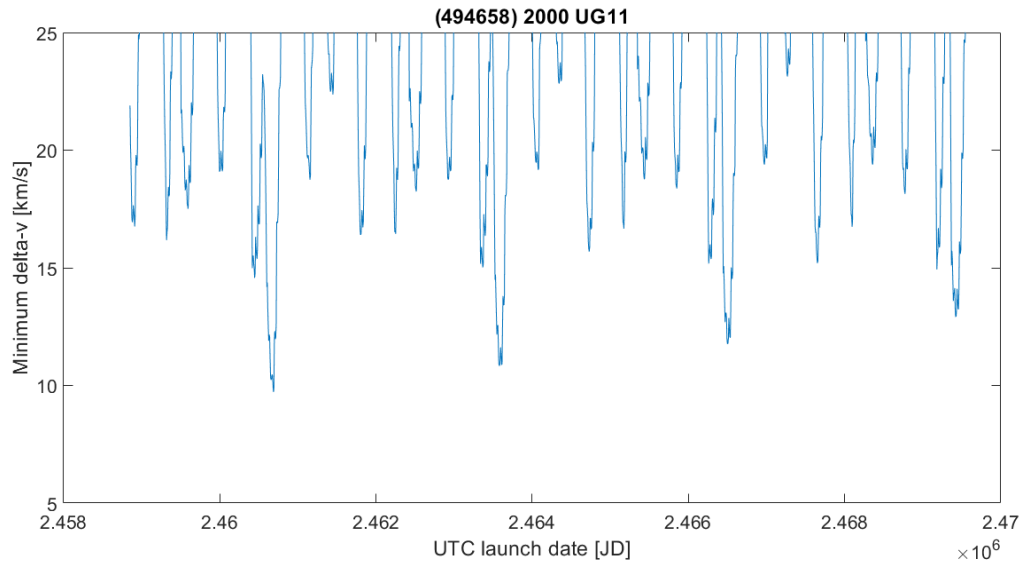


Figure 57: Optimal Δv values for (494658) 2000 UG11

B.2 Most optimal trajectories

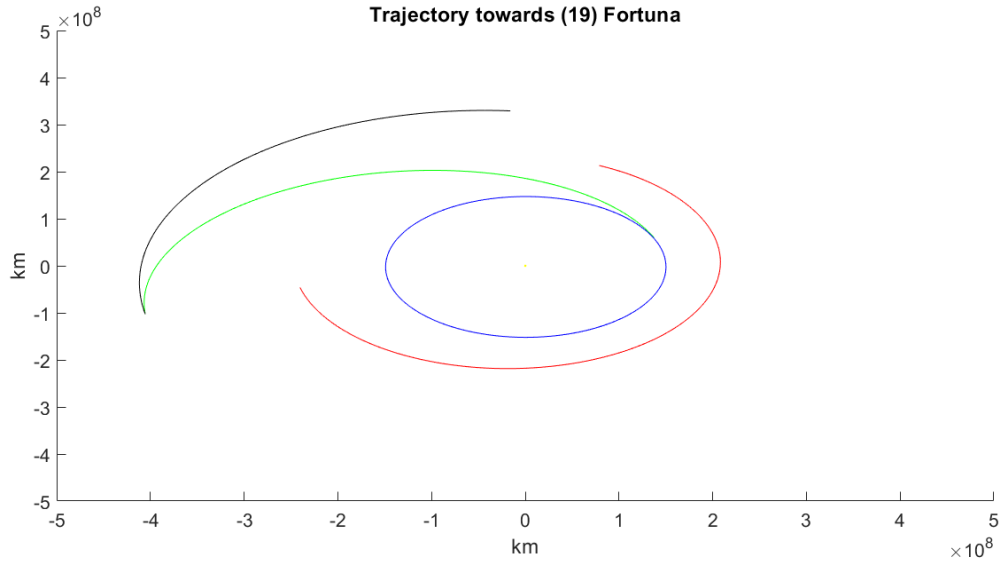


Figure 58: Minimum Δv trajectory for (19) Fortuna

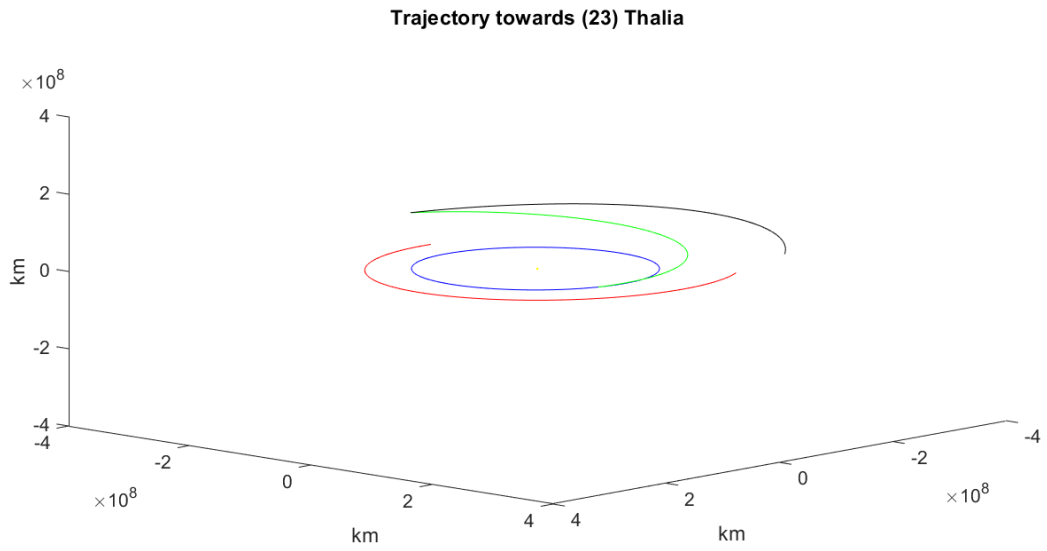


Figure 59: Minimum Δv trajectory for (23) Thalia

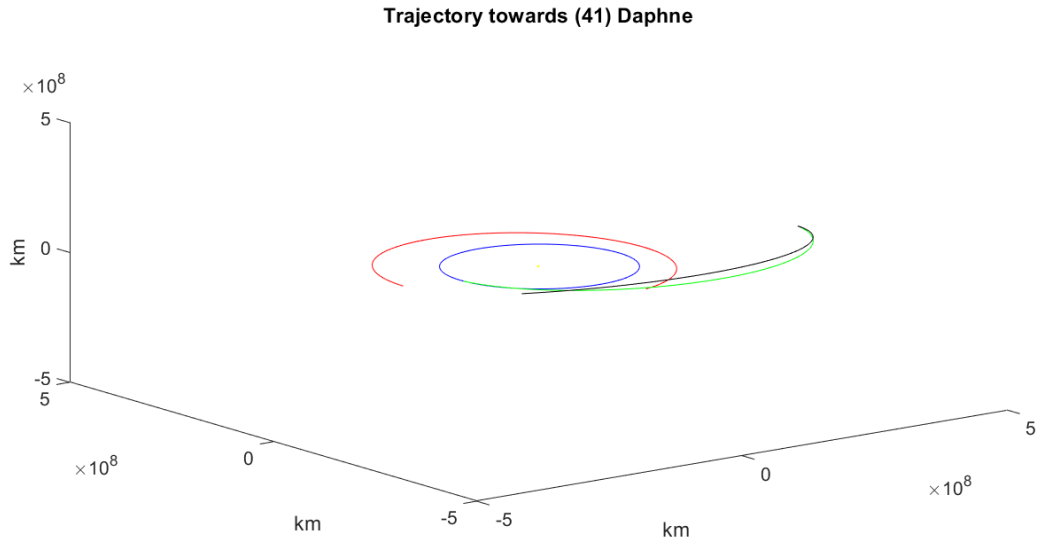


Figure 60: Minimum Δv trajectory for (41) Daphne

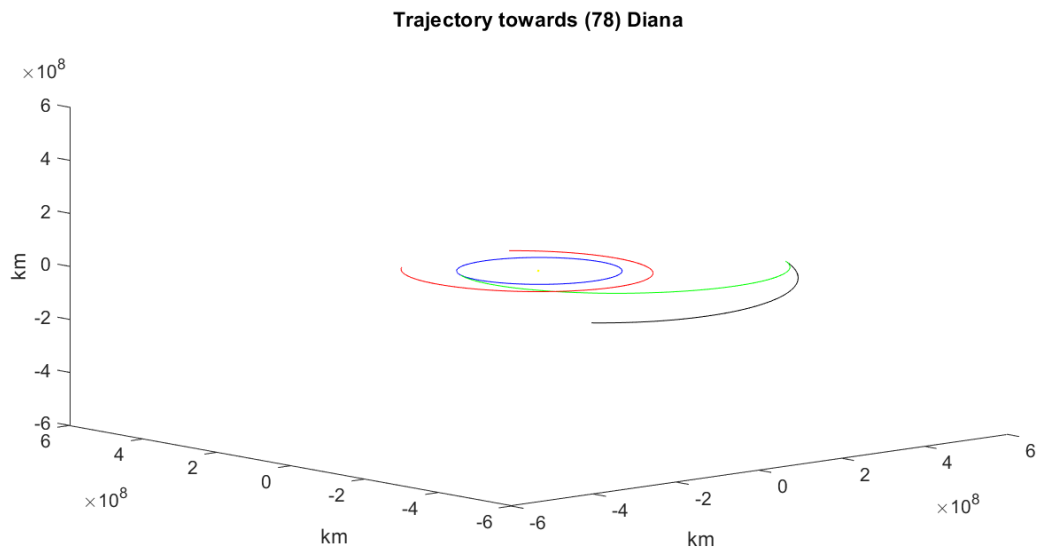
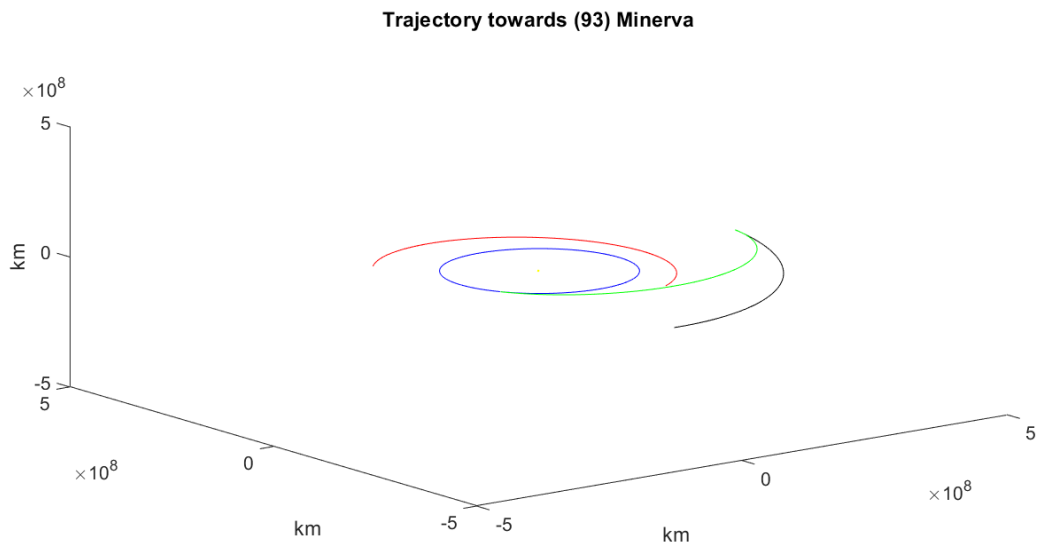
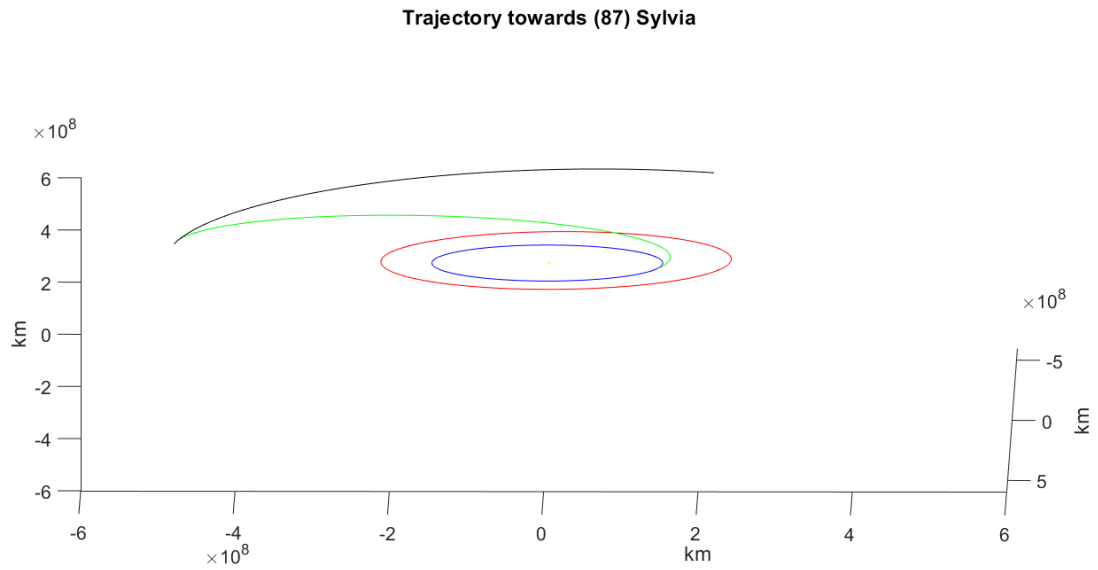


Figure 61: Minimum Δv trajectory for (78) Diana



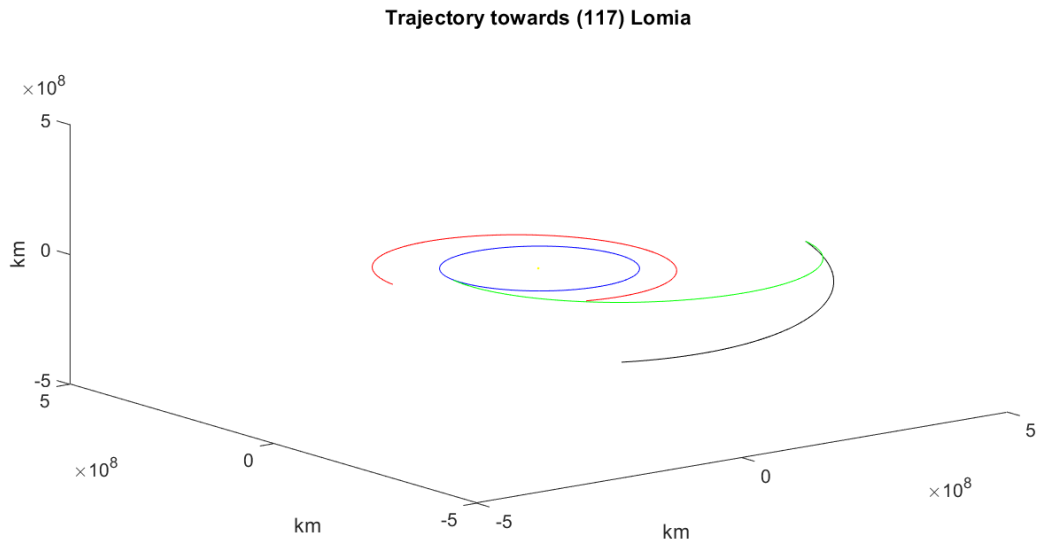


Figure 64: Minimum Δv trajectory for (117) Lomia

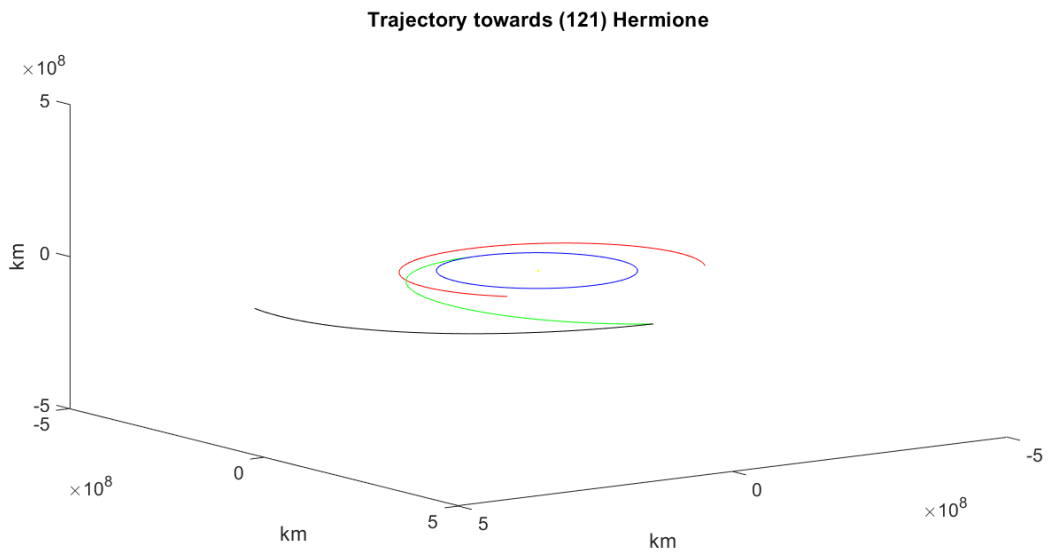


Figure 65: Minimum Δv trajectory for (121) Hermione

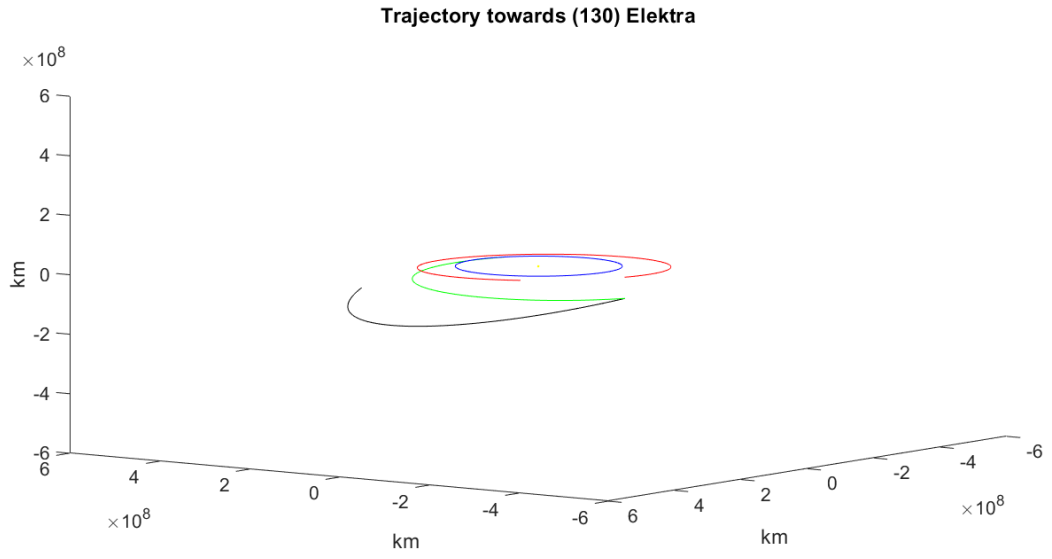


Figure 66: Minimum Δv trajectory for (130) Elektra

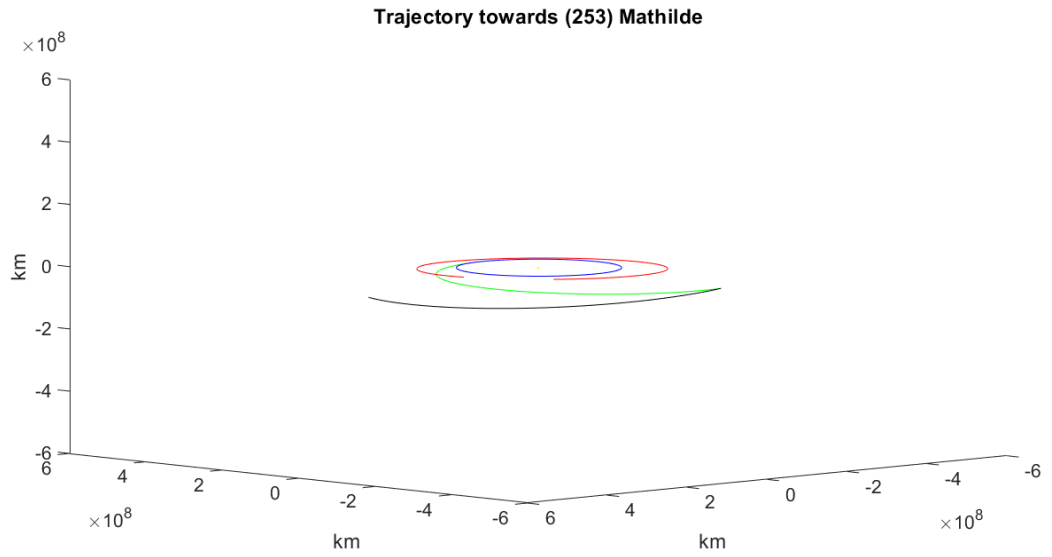


Figure 67: Minimum Δv trajectory for (253) Mathilde

Trajectory towards (259) Aletheia

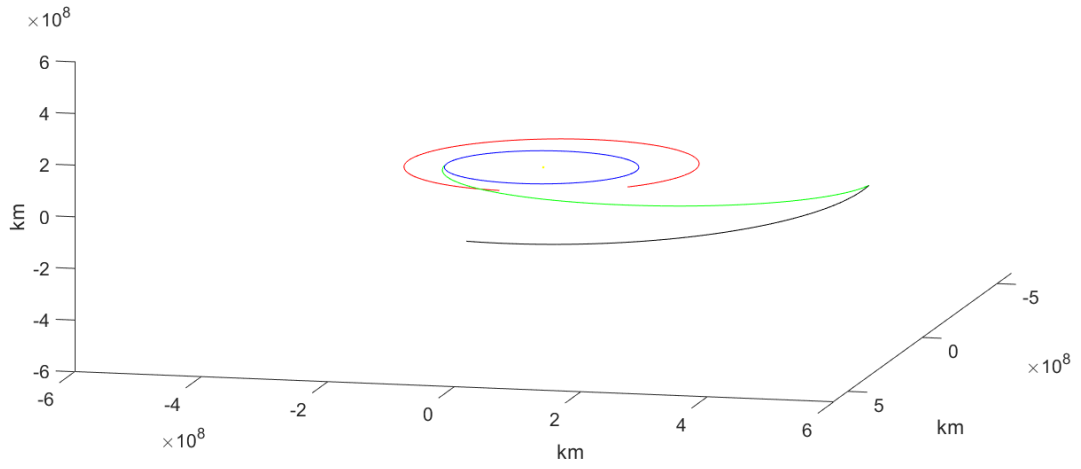


Figure 68: Minimum Δv trajectory for (259) Aletheia

Trajectory towards (324) Bamberga

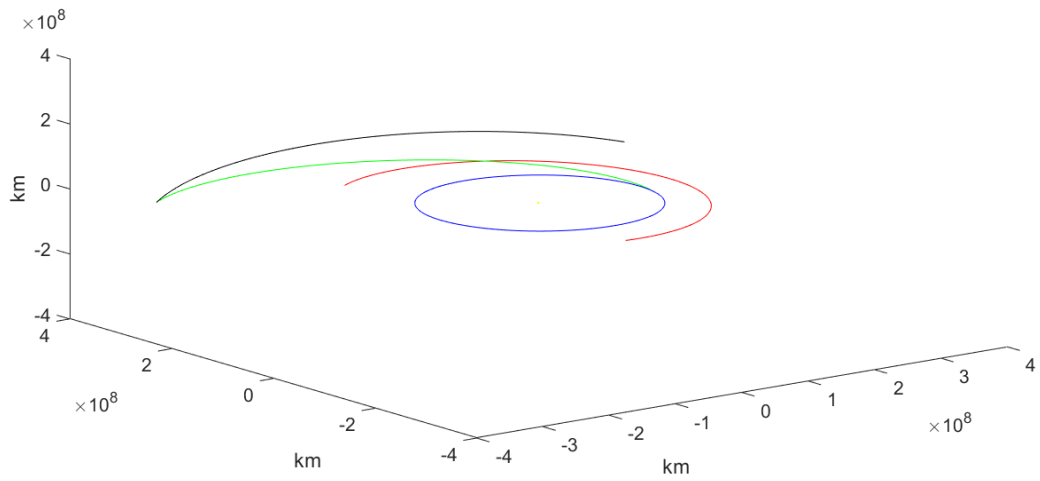
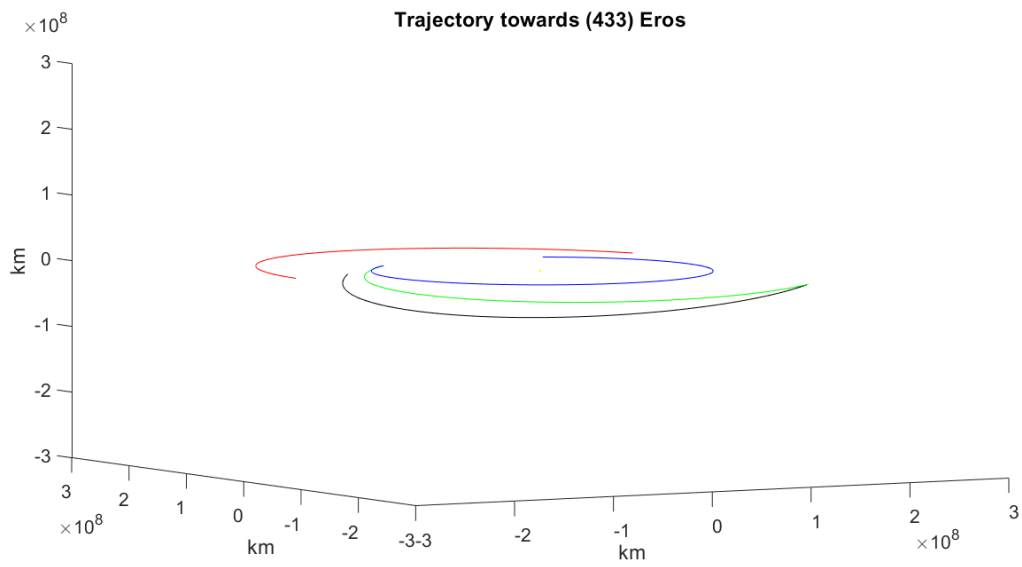
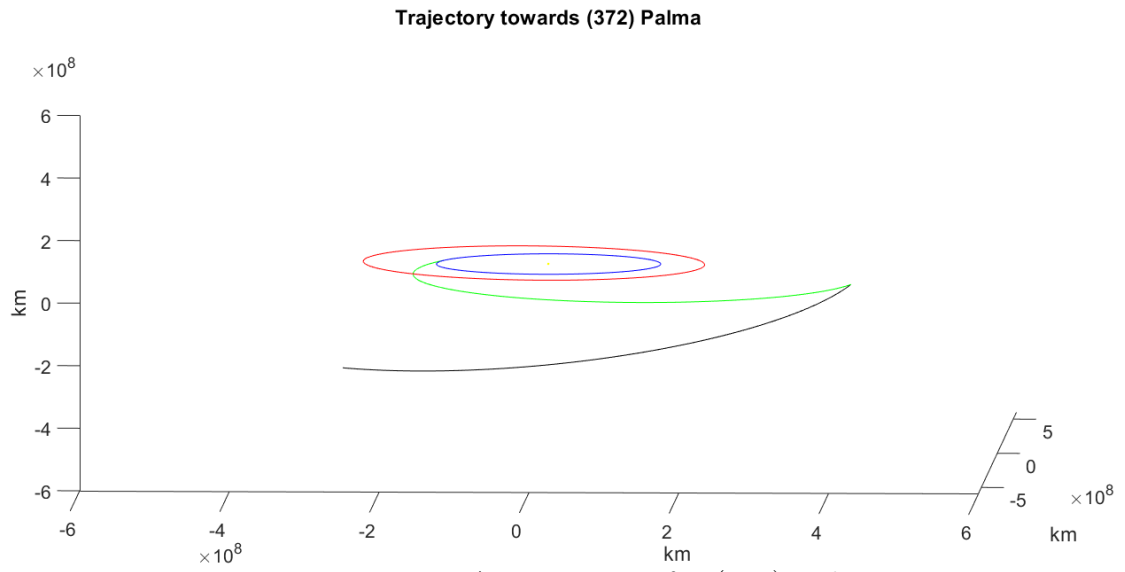


Figure 69: Minimum Δv trajectory for (324) Bamberga



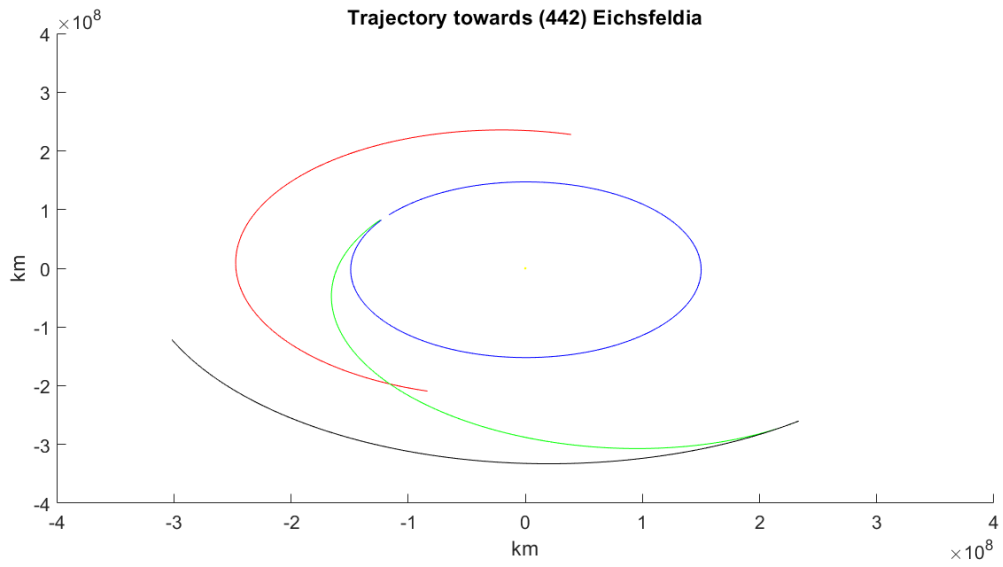


Figure 72: Minimum Δv trajectory for (442) Eichsfeldia

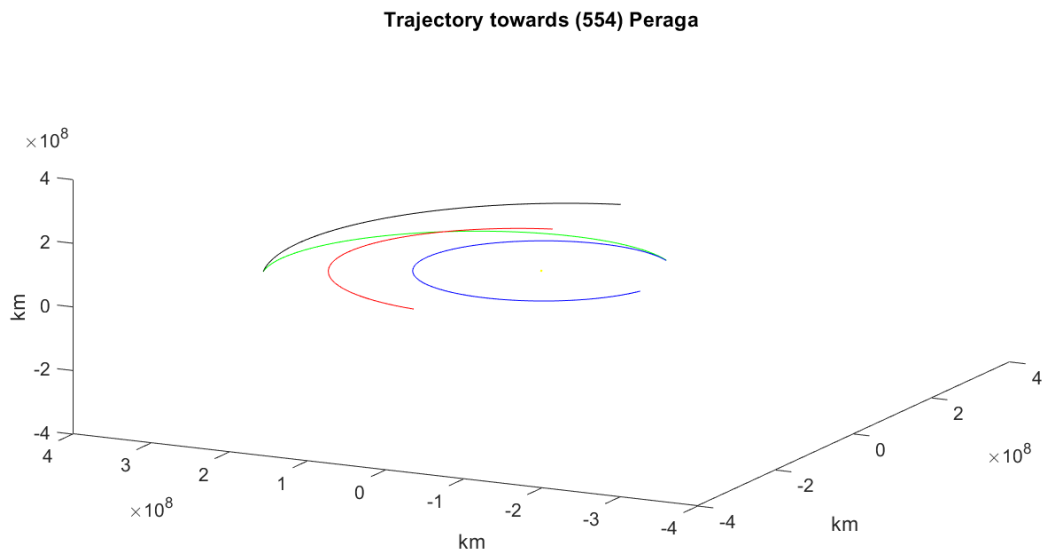


Figure 73: Minimum Δv trajectory for (554) Peraga

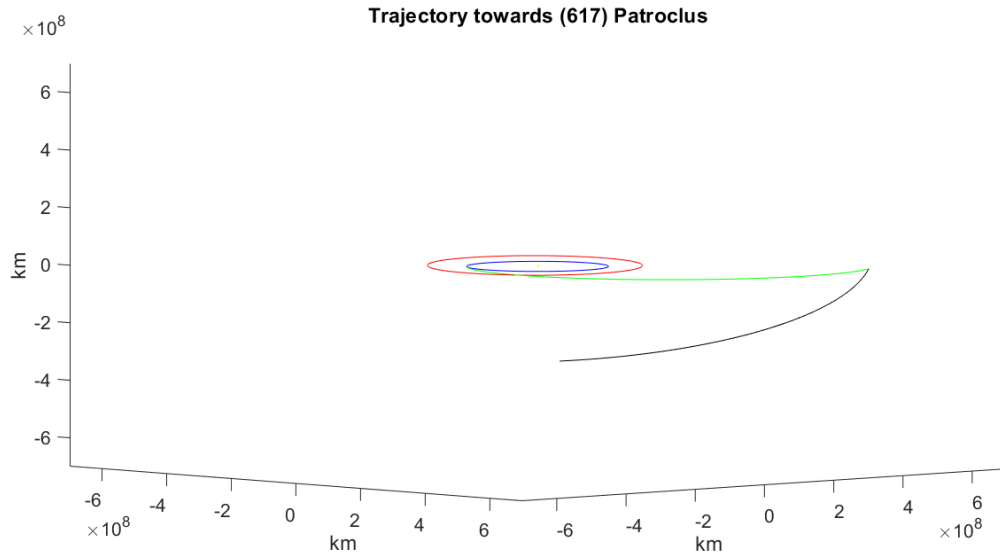


Figure 74: Minimum Δv trajectory for (617) Patroclus

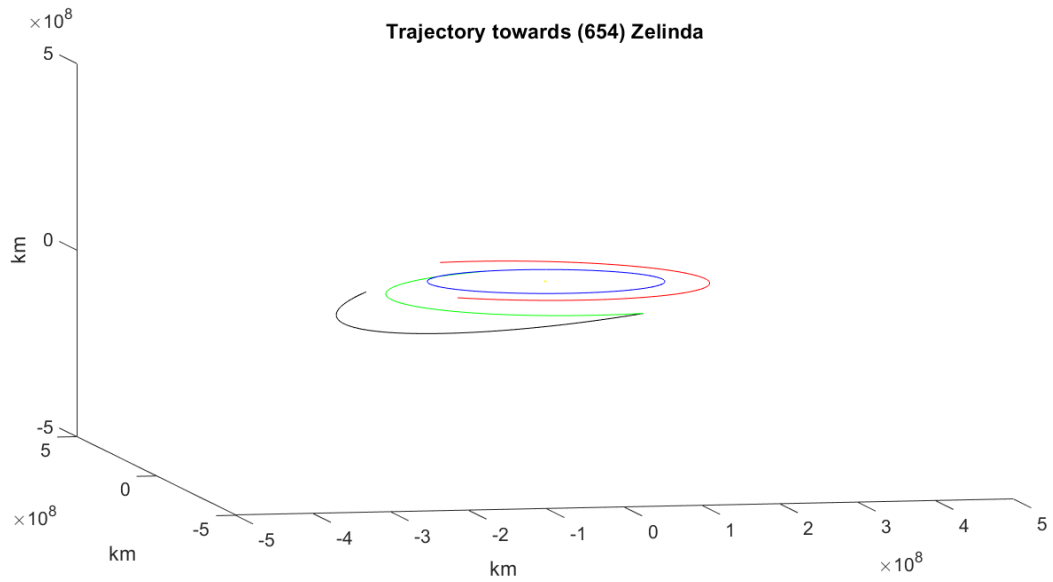


Figure 75: Minimum Δv trajectory for (654) Zelinda

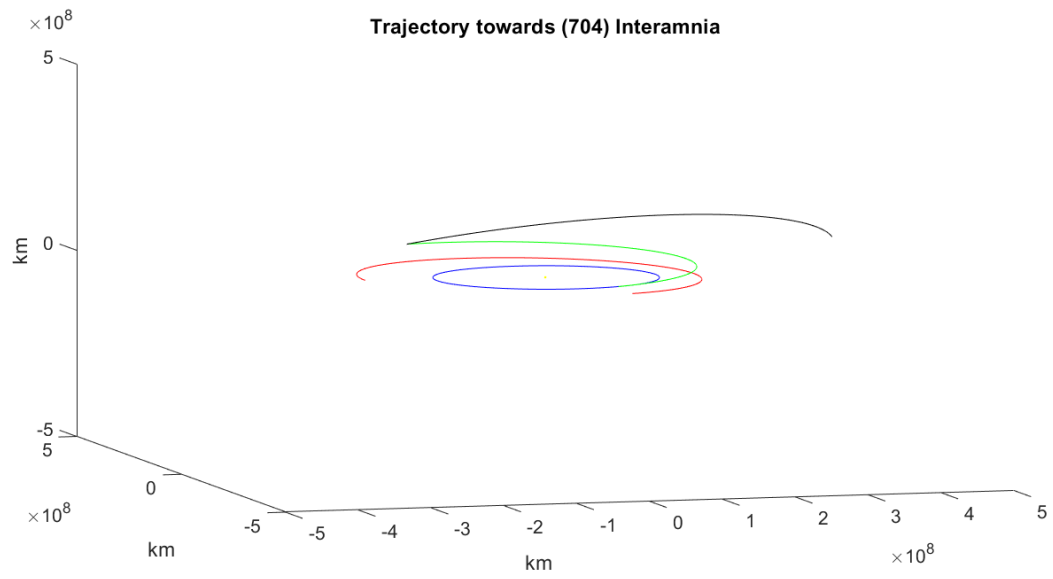


Figure 76: Minimum Δv trajectory for (704) Interamnia

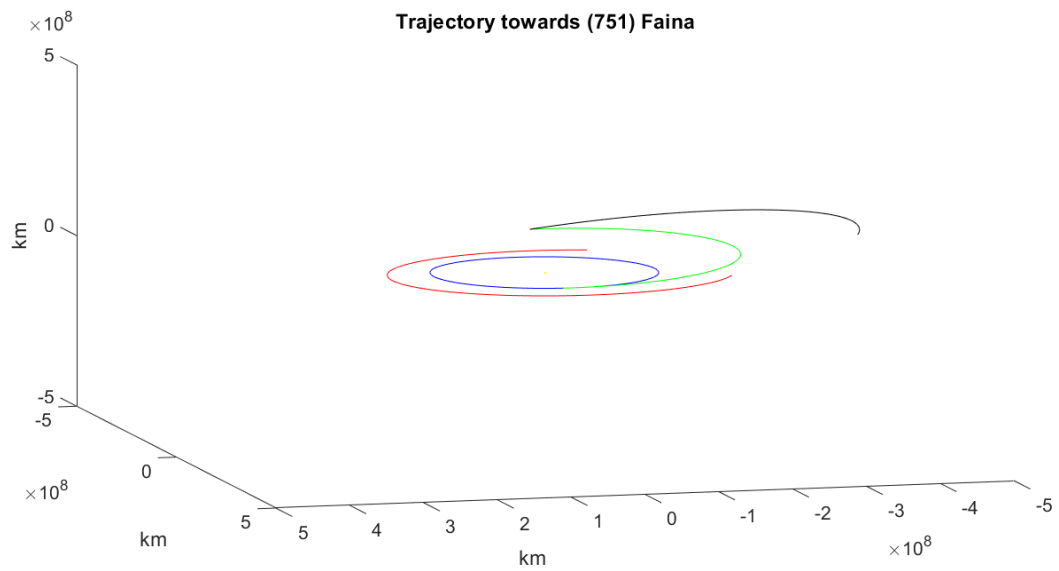


Figure 77: Minimum Δv trajectory for (751) Faina

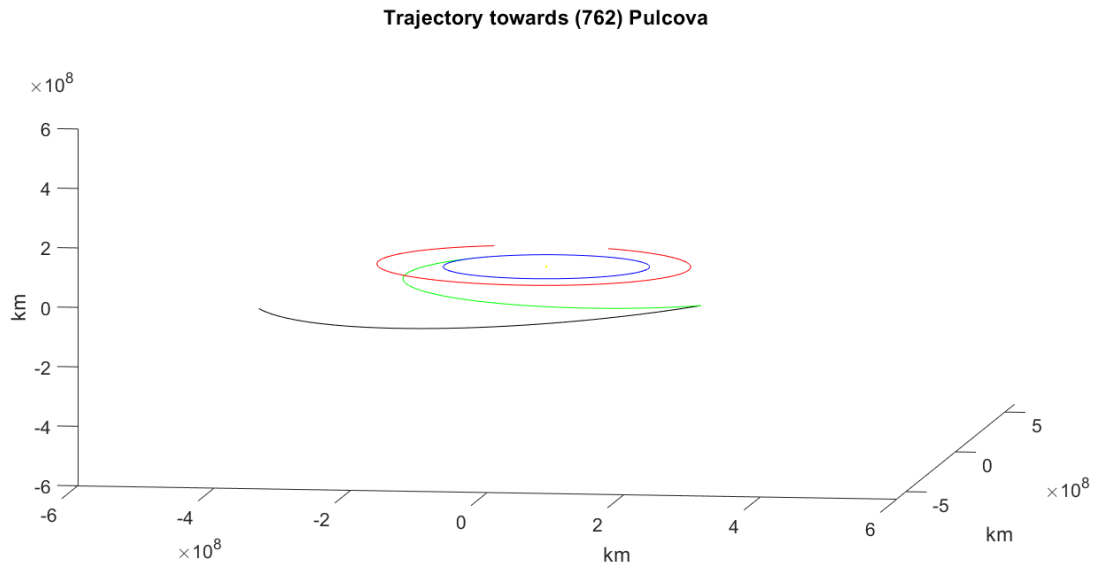


Figure 78: Minimum Δv trajectory for (762) Pulcova

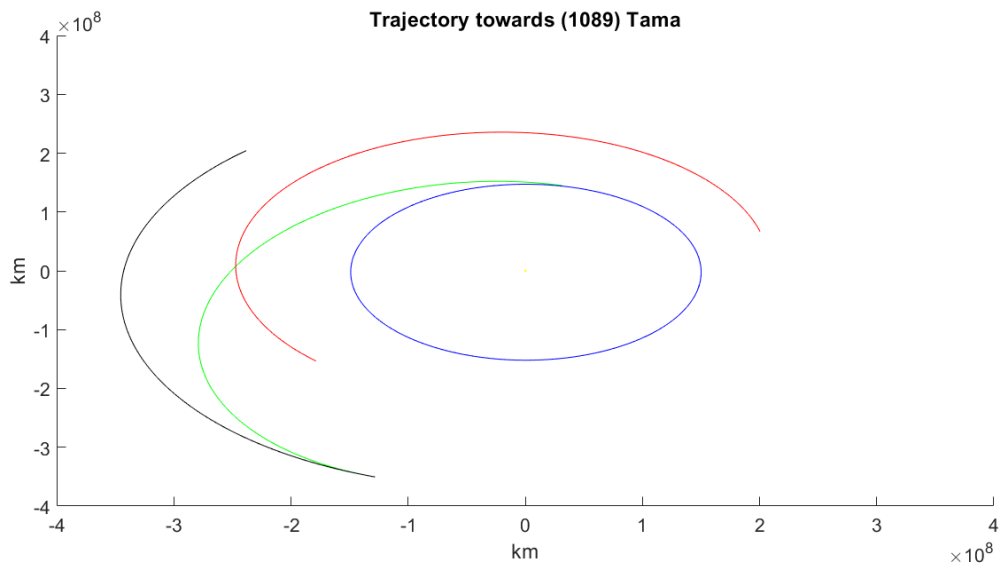


Figure 79: Minimum Δv trajectory for (1089) Tama

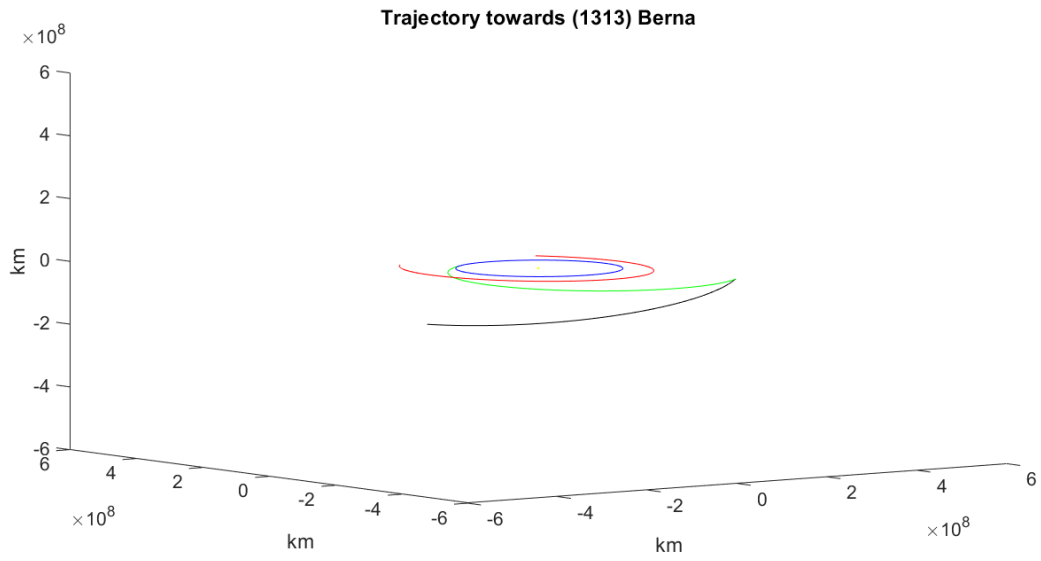


Figure 80: Minimum Δv trajectory for (1313) Berna

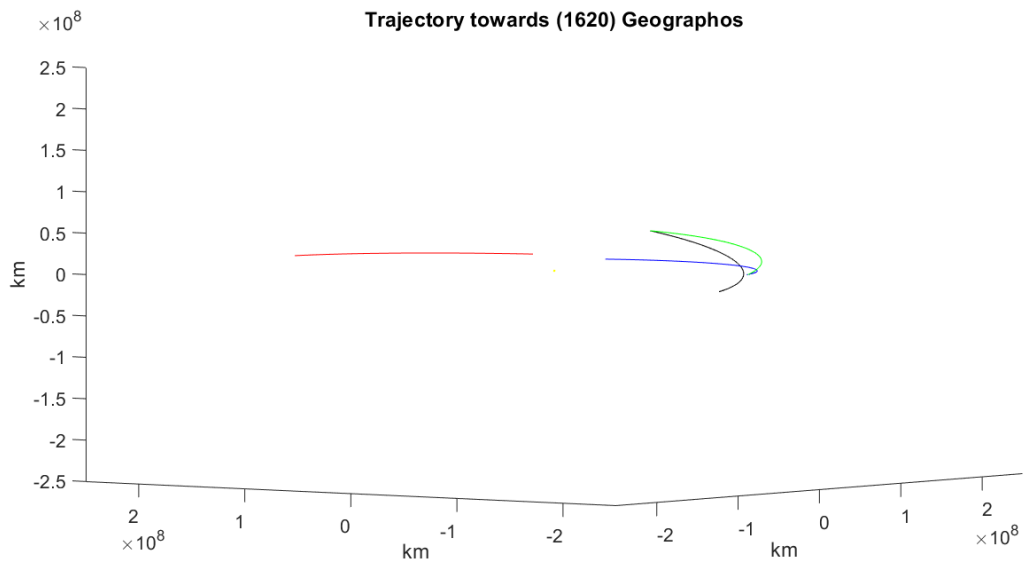


Figure 81: Minimum Δv trajectory for (1620) Geographos

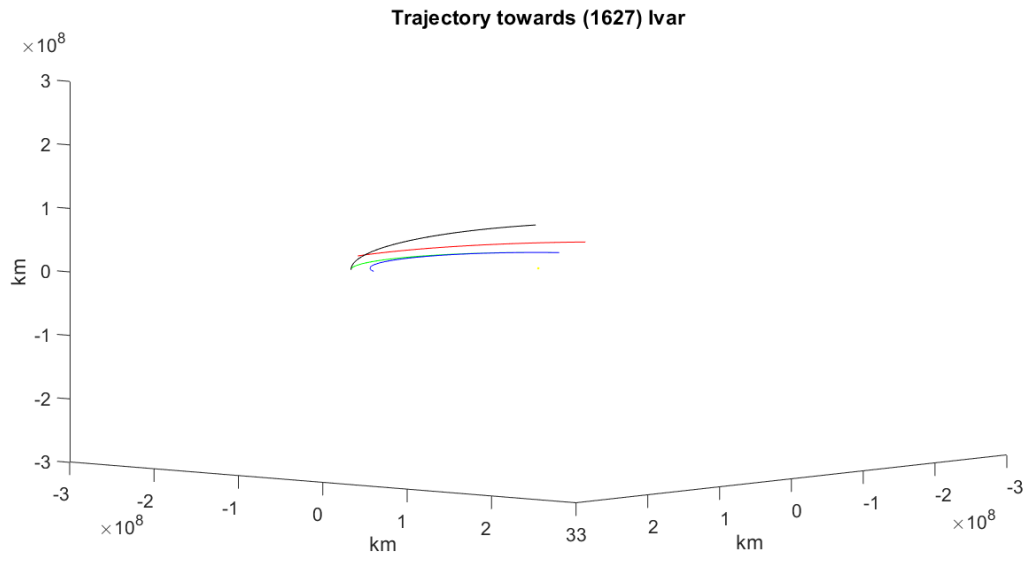


Figure 82: Minimum Δv trajectory for (1627) Ivar

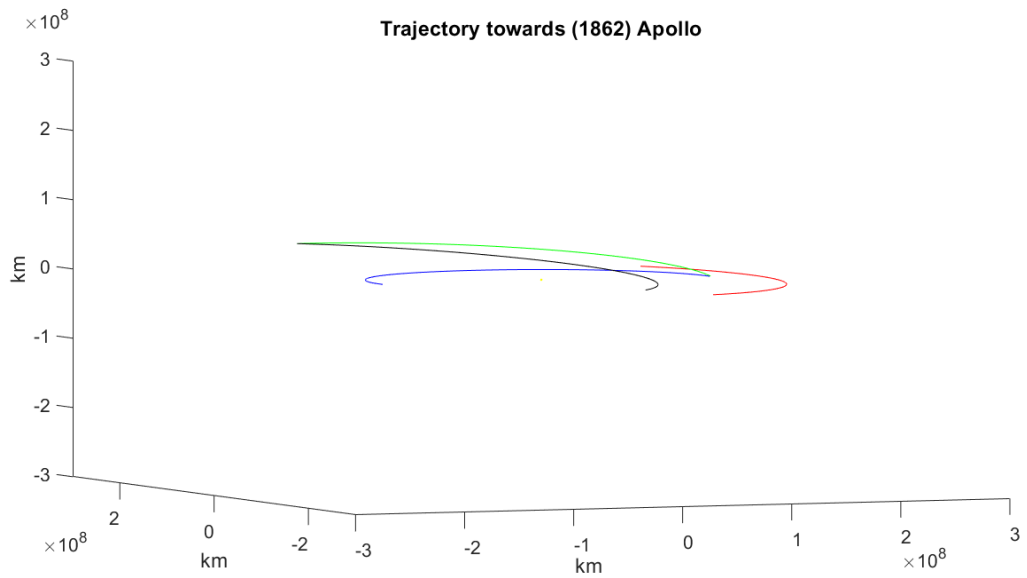


Figure 83: Minimum Δv trajectory for (1862) Apollo

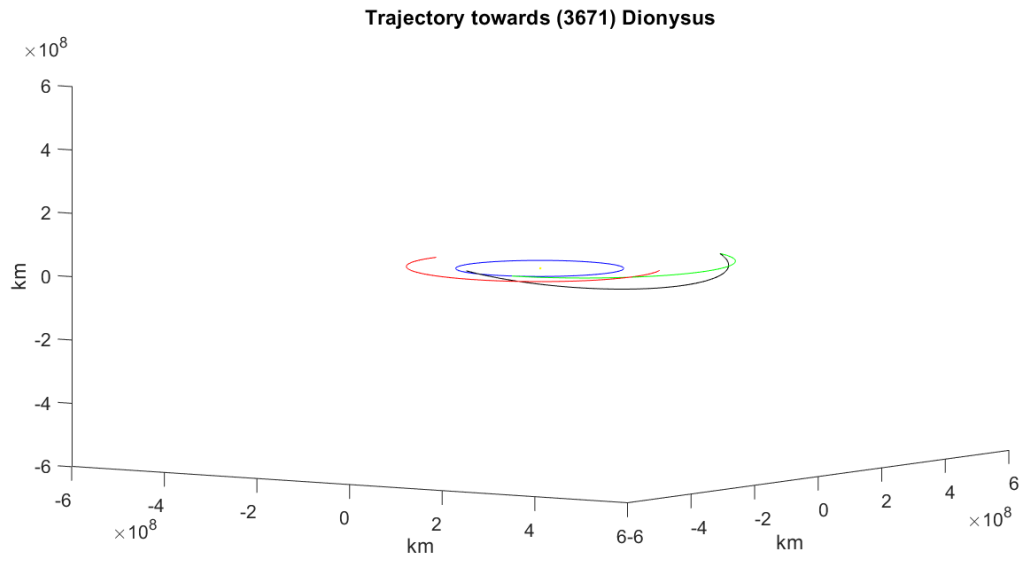


Figure 84: Minimum Δv trajectory for (3671) Dionysus

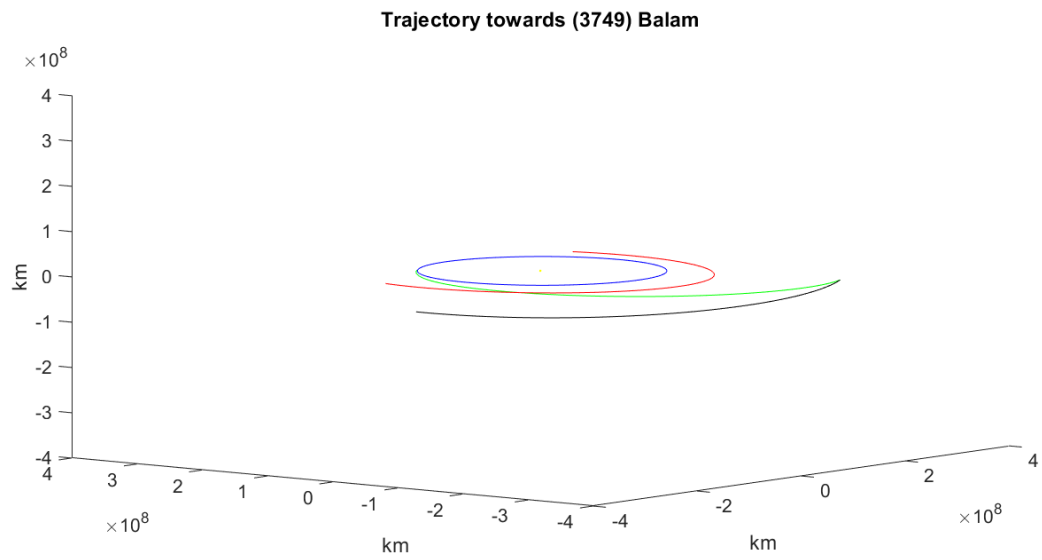


Figure 85: Minimum Δv trajectory for (3749) Balam

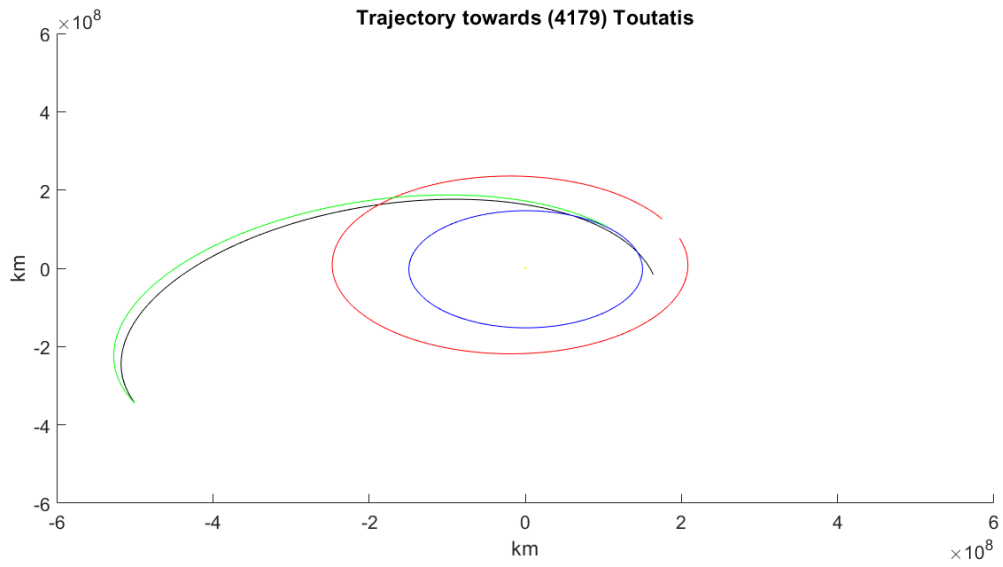


Figure 86: Minimum Δv trajectory for (4179) Toutatis

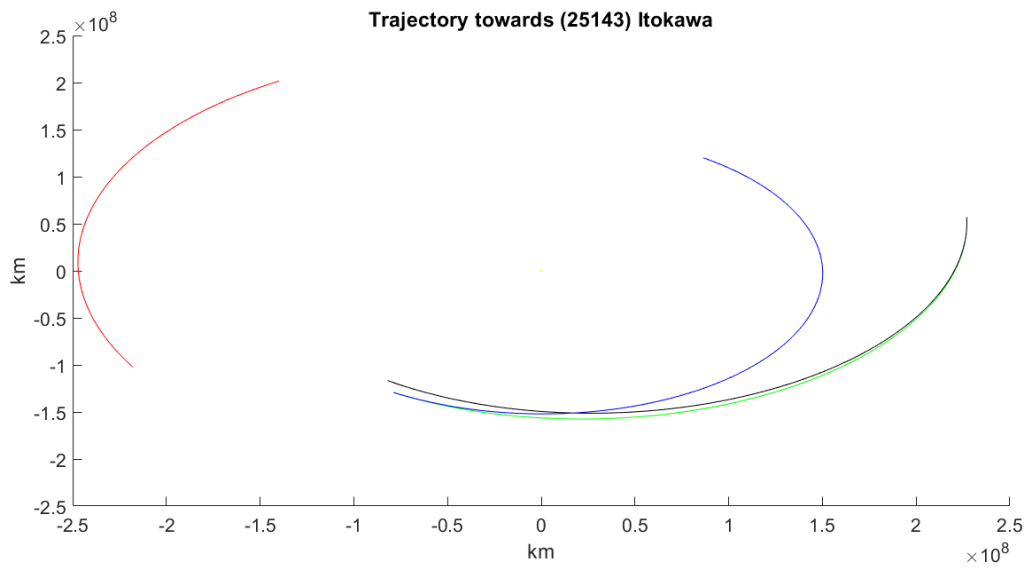


Figure 87: Minimum Δv trajectory for (25143) Itokawa

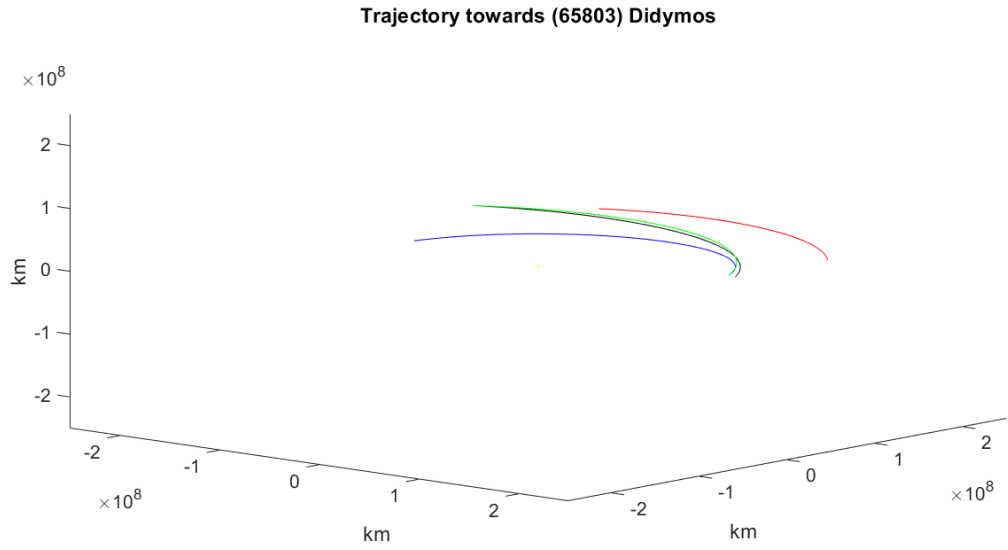


Figure 88: Minimum Δv trajectory for (65803) Didymos

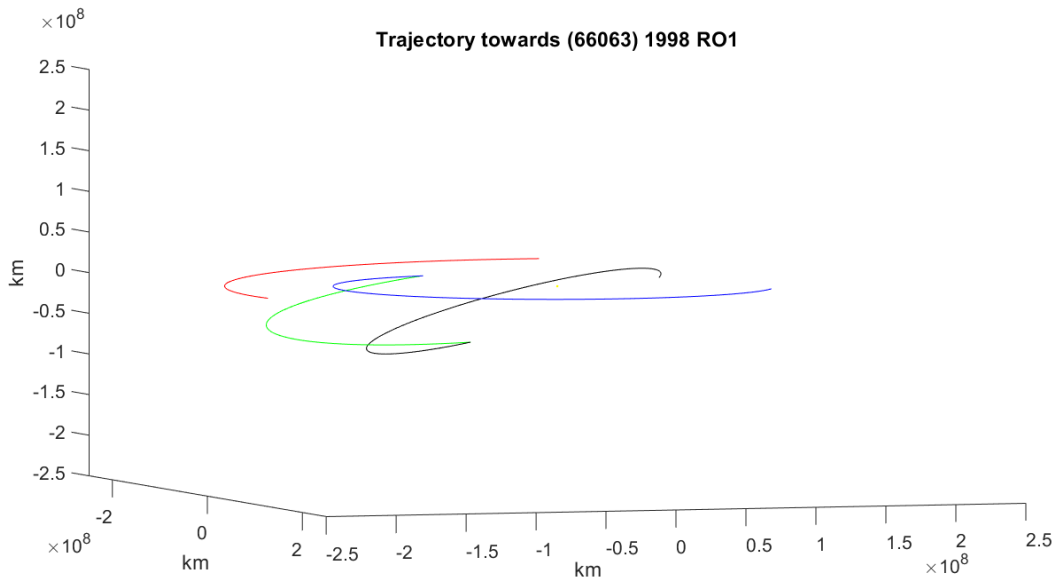


Figure 89: Minimum Δv trajectory for (66063) 1998 RO1

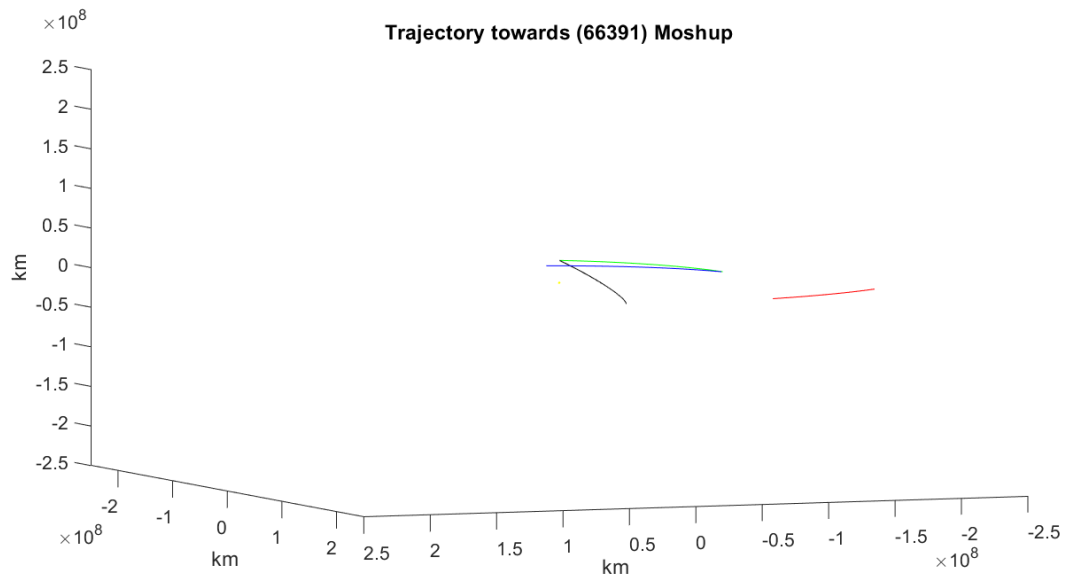


Figure 90: Minimum Δv trajectory for (66391) Moshup

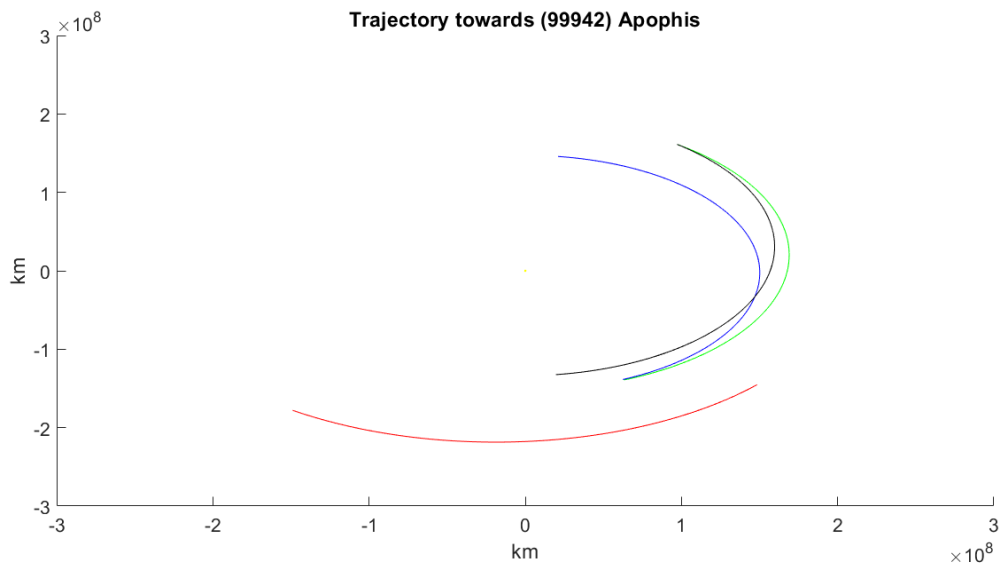


Figure 91: Minimum Δv trajectory for (99942) Apophis

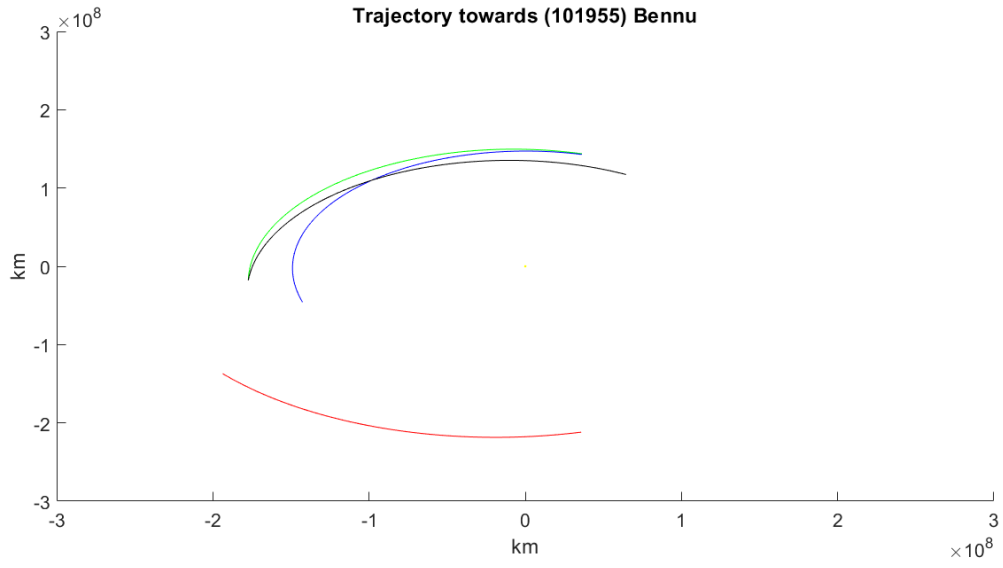


Figure 92: Minimum Δv trajectory for (101955) Bennu

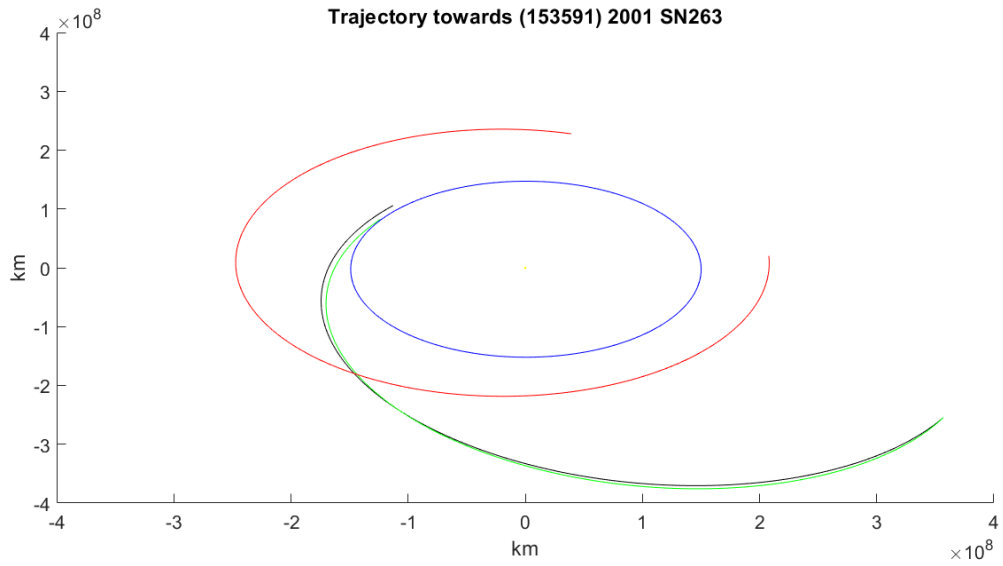


Figure 93: Minimum Δv trajectory for (153591) 2001 SN263

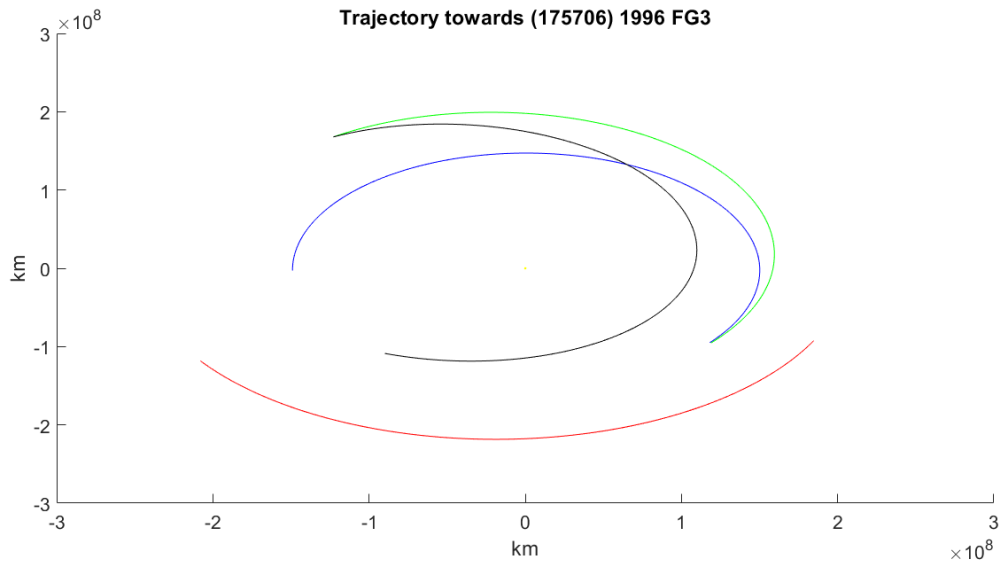


Figure 94: Minimum Δv trajectory for (175706) 1996 FG3

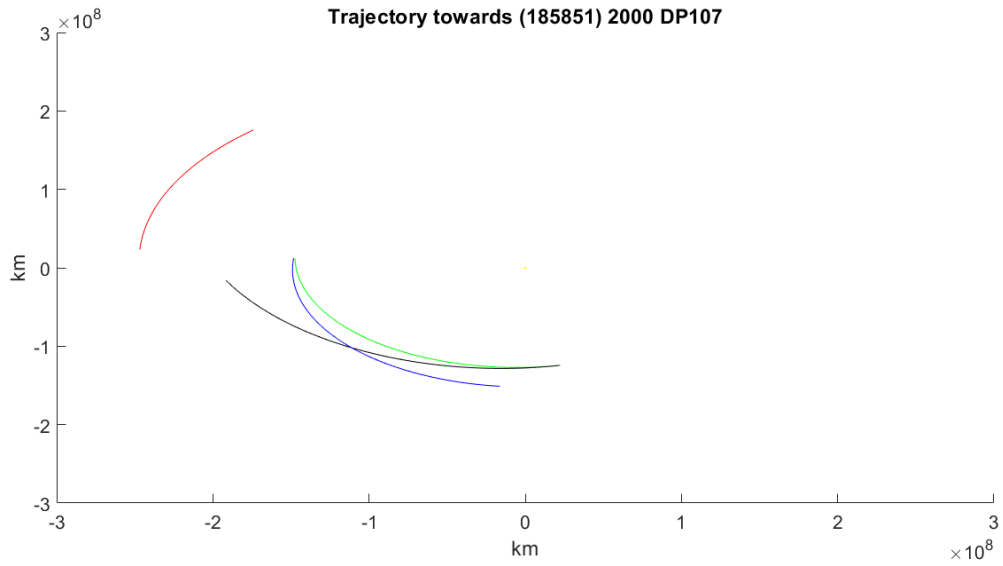


Figure 95: Minimum Δv trajectory for (185851) 2000 DP107

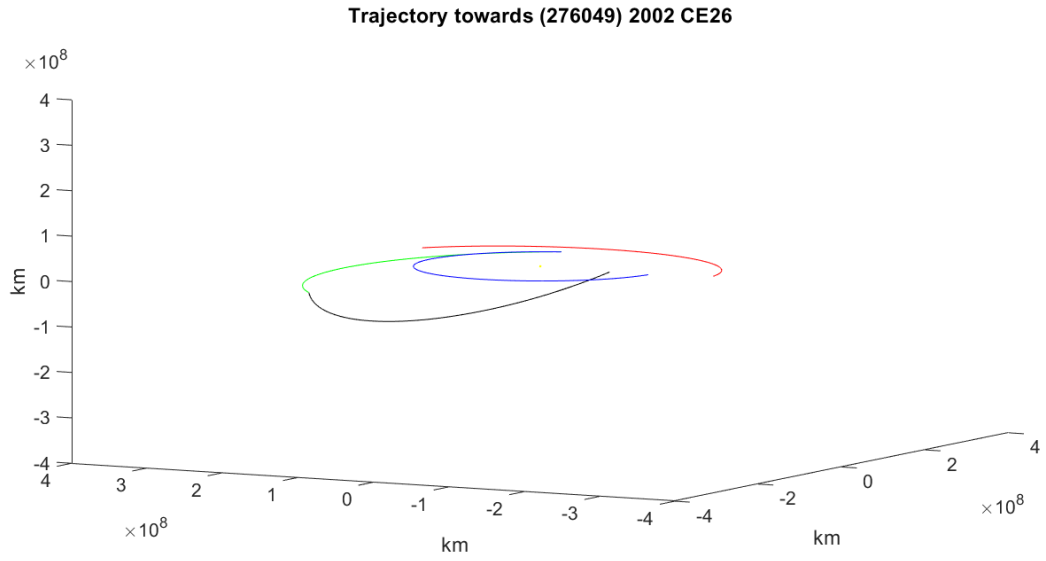


Figure 96: Minimum Δv trajectory for (276049) 2002 CE26

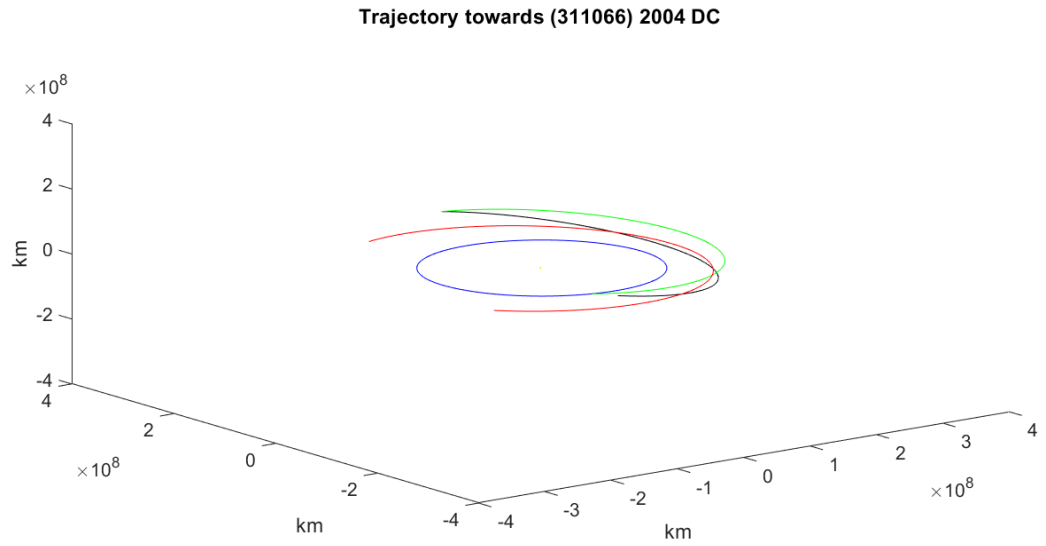


Figure 97: Minimum Δv trajectory for (311066) 2004 DC

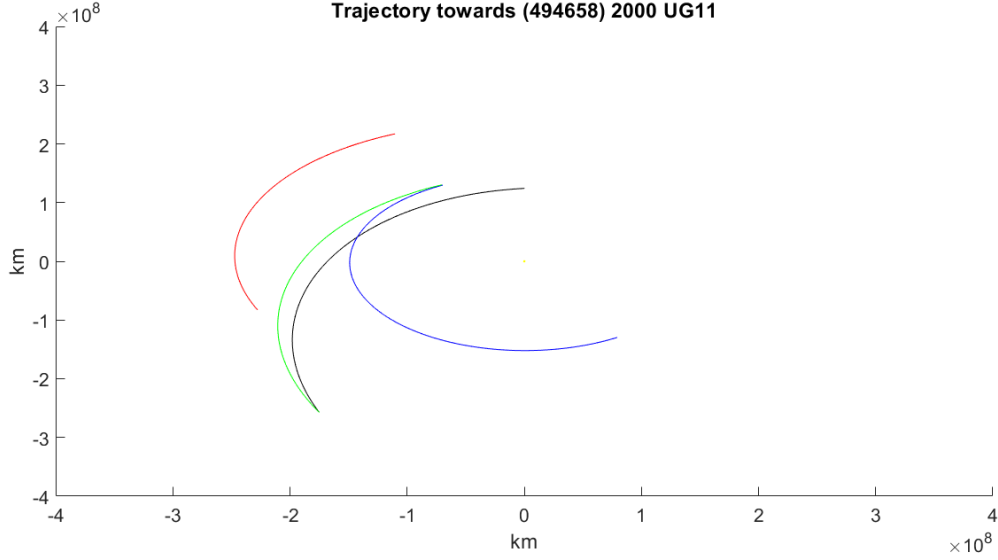


Figure 98: Minimum Δv trajectory for (494658) 2000 UG11

C Gravity model

C.1 Favourability factor values

| Asteroid | Economic size (\$) | Economic distance (km/s) | $\log_{10}(F_j)$ |
|-------------------|--------------------|--------------------------|------------------|
| (19) Fortuna | 1.80E+19 | 10.11 | 14.86 |
| (23) Thalia | 4.46E+18 | 12.02 | 13.43 |
| (41) Daphne | 1.80E+19 | 12.06 | 14.02 |
| (78) Diana | 1.79E+18 | 11.23 | 13.38 |
| (87) Sylvia | 2.91E+19 | 13.17 | 13.74 |
| (93) Minerva | 7.33E+18 | 11.97 | 13.67 |
| (117) Lomia | 1.32E+19 | 12.67 | 13.62 |
| (121) Hermione | 9.82E+18 | 12.94 | 13.37 |
| (130) Elektra | 1.23E+19 | 14.25 | 12.90 |
| (253) Mathilde | 2.05E+17 | 11.21 | 12.44 |
| (259) Aletheia | 1.70E+19 | 12.34 | 13.87 |
| (324) Bamberga | 2.05E+19 | 11.76 | 14.20 |
| (372) Palma | 1.12E+19 | 14.52 | 12.74 |
| (433) Eros | 1.39E+16 | 7.35 | 12.95 |
| (442) Eichsfeldia | 4.97E+17 | 10.07 | 13.32 |
| (554) Peraga | 1.05E+18 | 9.92 | 13.71 |
| (617) Patroclus | 2.96E+18 | 15.64 | 11.68 |
| (654) Zelinda | 2.43E+18 | 11.61 | 13.34 |
| (704) Interamnia | 5.85E+19 | 13.52 | 13.90 |
| (751) Faina | 7.30E+18 | 12.13 | 13.60 |
| (762) Pulcova | 2.79E+18 | 12.71 | 12.92 |
| (1089) Tama | 1.89E+15 | 9.27 | 11.25 |
| (1313) Berna | 4.68E+15 | 12.24 | 10.35 |
| (1620) Geographos | 3.08E+13 | 11.99 | 8.28 |
| (1627) Ivar | 1.17E+15 | 8.093 | 11.55 |
| (1862) Apollo | 1.18E+13 | 11.61 | 8.03 |

| | | | |
|---------------------|----------|--------|-------|
| (3671) Dionysus | 1.67E+12 | 10.5 | 7.66 |
| (3749) Balam | 1.06E+15 | 9.32 | 10.98 |
| (4179) Toutatis | 1.11E+14 | 9.729 | 9.82 |
| (25143) Itokawa | 7.44E+10 | 4.714 | 8.82 |
| (65803) Didymos | 1.17E+12 | 7.8 | 8.68 |
| (66063) 1998 RO1 | 7.97E+11 | 17.3 | 4.39 |
| (66391) Moshup | 5.51E+12 | 21.85 | 3.25 |
| (99942) Apophis | 1.08E+11 | 5.533 | 8.63 |
| (101955) Bennu | 1.55E+11 | 5.72 | 8.71 |
| (153591) 2001 SN263 | 1.70E+13 | 8.048 | 9.73 |
| (175706) 1996 FG3 | 7.03E+12 | 6.294 | 10.11 |
| (185851) 2000 DP107 | 1.06E+12 | 10.78 | 7.34 |
| (276049) 2002 CE26 | 3.88E+13 | 19.01 | 5.33 |
| (311066) 2004 DC | 7.14E+10 | 11.14 | 6.02 |
| (494658) 2000 UG11 | 1.87E+10 | 11.305 | 5.36 |

Table 5: Favourability factor of the target asteroids

D Matlab code

D.1 Asteroid_deltav_calculator

```

1 close all
2 clear variables
3 clc
4
5 init; % Start the semat environment
6 default = load_kernels(default); % Start the SPICE kernels
7 cr3bp = init_CR3BP('EARTH', 'MOON', default); % Start Earth-Moon
   CR3BP model
8
9 % Problem constants
10 G = cst.env.G*10^-9; %[km^3*kg^-1*s^-2]
11 m_1 = cr3bp.m1.M; %[kg] Earth mass
12 m_2 = cr3bp.m2.M; %[kg] Moon mass
13 m_s = cst.sun.ms*(m_1+m_2); %[kg] Sun mass
14 r_s = [0,0,0]; % Sun position at origin in ECLIPJ2000
15 mu_s = G*m_s; %[km^3/s^2] Sun standard gravitational parameter
16 R_1 = cr3bp.m1.Req; %[km] Earth equatorial radius
17 R_2 = cr3bp.m2.Req; %[km] Moon equatorial radius
18 a_12 = cr3bp.L; %[km] Earth-Moon semi-major axis
19 n_12 = sqrt(G*(m_1+m_2)/(a_12^3)); %[rad/s] Earth-Moon angular
   velocity
20 t_12 = sqrt((a_12^3)/(G*(m_1+m_2))); %[s] Earth-Moon characterisitic
   time
21 mu = cr3bp.mu; % CR3BP mu parameter
22 mu_1 = 1-mu; % Earth mu parameter
23 mu_2 = mu; % Moon mu parameter

```

```

24 P1 = [-mu_2,0,0]; %[adim] Earth position in the synodic frame of
    reference
25 P2 = [mu_1,0,0]; %[adim] Moon position in the synodic frame of
    reference
26 t_0 = 2458849.5; %[JD] Minimum start date 01/01/2020 00:00:00 UTC
27 t_f = 2469807.5; %[JD] Maximum start date 01/01/2050 00:00:00 UTC
28 t_start = (t_0:6:t_f); %[days] Vector of start dates
29 t_start_J2000 = cspice_str2et(strcat('JD',num2str(t_start(:)))); %[s]
    Vector of seconds between J2000 TDB and start date
30
31 % Lagrange point calculation
32 [LP] = Lagrange_solver_adim(cr3bp); %[adim] Lagrange point position
    matrix
33
34 % Target parameters
35 number = 19; % Target number
36 name = 'Fortuna'; % Target name
37 SPKID = num2str(2e6+number); % Target SPK ID
38 designation = char(strcat('(' ,num2str(number) ,') ',{ ' ' },name)); %
    Target designation
39 filename = strcat('(' ,num2str(number) ,')_',name, '.mat'); % Data file
    name
40
41 % Spacecraft initial position in the synodic frame of reference
42 x_0 = LP(1,1); %[adim] Initial x position
43 y_0 = LP(1,2); %[adim] Initial y position
44 z_0 = LP(1,3); %[adim] Initial z position
45
46 plot_prel = true; % Plot preliminary results
47
48 % Preliminary solver
49 [delta_v_dopmin,t_flight_opmin] = preliminary_solver(SPKID,
    designation,t_start,t_start_J2000,x_0,y_0,z_0,cr3bp,t_12,mu_s,
    plot_prel);
50
51 % Optimisation parameters
52 delta_v_0 = (0.4:0.1:delta_v_dopmin+2); %[km/s] Initial delta-v from
    the L1 point
53
54 delta_v_0_adim = delta_v_0/(n_12*a_12); %[adim] Initial delta-v from
    the L1 point
55
56 alpha_0 = deg2rad(0:22.5:180); %[rad] Initial tangential angle to the
    Moon
57
58 if min(t_flight_opmin-30) > 4
59     t_flight = (t_flight_opmin-30:6:t_flight_opmin+720); %[days]
        Flight time from Earth SOI to target
60 else
61     t_flight = (4:6:t_flight_opmin+720);
62 end

```

```

63
64 % Spacecraft initial state
65 theta_L1M = atan((R_2/a_12)/(P2(1)-x_0)); %[rad] Angle of the normal
    component of the initial velocity
66
67 % Optimised variables
68 delta_v_min = 10000*ones(size(t_start)); %[km/s] Minimum total delta-
    v for each start date
69 delta_v_0_opt = zeros(size(t_start)); %[km/s] Optimal initial delta-v
    for each start date
70 alpha_0_opt = zeros(size(t_start)); %[deg] Optimal initial tangential
    angle to the Moon for each start date
71 t_flight_opt = zeros(size(t_start)); %[days] Optimal flight time from
    Earth SOI to target for each start date
72 delta_v_dep_opt = 10000*ones(size(t_start)); %[days] Optimal
    departure from Earth SOI delta-v to target for each start date
73
74 t_span = [0 2*pi]; %[adim] Integration timespan
75
76 % Integration conditions
77 options = odeset('Reltol',default.ode113.RelTol,'Abstol',default.
    ode113.AbsTol,'Events',@odezero_EARTHSOI);
78
79 % Optimising algorithm
80 for i = 1:size(delta_v_0,2)
81     delta_v_0_adim_i = delta_v_0_adim(i);
82     delta_v_0_i = delta_v_0(i);
83     for j = 1:size(alpha_0,2)
84         alpha_0_j = alpha_0(j);
85         vx_0 = delta_v_0_adim_i*cos(theta_L1M); %[adim] Initial vx
            velocity
86         vy_0 = -delta_v_0_adim_i*sin(theta_L1M)*sin(alpha_0_j); %[
            adim] Initial vy velocity
87         vz_0 = delta_v_0_adim_i*sin(theta_L1M)*cos(alpha_0_j); %[adim
            ] Initial vz velocity
88         C=[x_0,y_0,z_0,vx_0,vy_0,vz_0]; %[adim] Initial conditions of
            state vector (x,y,z,vx,vy,vz)
89         % Integration setup
90         cv0 = (1:42)'; % Integration vector
91         cv0(1:6) = C; % 6-dim state
92         cv0 = matrixToVector(cv0,cr3bp.est.orbit.STM0,6,6,6); % STM
            concatenation after the 6-dim state
93         % Integration of the movement equations using ODE113 with STM
            until departure from the Earth's SOI
94         [~,~,t_sc_soi_syn_adim,cv_soi_syn_adim,~] = ode113(@(t,y)
            cr3bp_derivatives_42(t,y,mu),t_span,cv0,options);
95         s_sc_soi_syn_adim = cv_soi_syn_adim(1:6); %[adim] State
            vector of the spacecraft at the Earth's SOI
96         parfor k = 1:size(t_start,2)
97             load_kernels_alt();
98             t_start_J2000_k = t_start_J2000(k);

```

```

99      % Seconds between J2000 TDB and SOI and state vector of
      % the spacecraft with regards to the Sun at SOI in the
      % J2000 inertial reference frame
100      [t_sc_soi_J2000,s_sc_soi] = syn2scECLIPJ2000(
          t_sc_soi_syn_adim,s_sc_soi_syn_adim',cr3bp,t_12,
          t_start_J2000_k,false,false);
101      r_sc_soi = s_sc_soi(1:3); %[km] Position of the
          spacecraft at SOI
102      v_sc_soi = s_sc_soi(4:6); %[km/s] Velocity of the
          spacecraft at SOI
103      for l = 1:size(t_flight,2)
104          t_flight_l = t_flight(l);
105          t_rv_J2000 = t_sc_soi_J2000+t_flight_l*cst.env.days;
          %[s] Seconds between J2000 TDB and rendez-vous
          date
106          eph_target_patch_rv_l = mice_spkezr(SPKID,t_rv_J2000,
          'ECLIPJ2000', 'NONE', 'SUN');
107          r_t_rv_l = eph_target_patch_rv_l.state(1:3); %
          Position of the target wrt the Sun in ECLIPJ2000
          at rendez-vous date
108          v_t_rv_l = eph_target_patch_rv_l.state(4:6); %
          Velocity of the target wrt the Sun in ECLIPJ2000
          at rendez-vous date
109          [v_sc_dep_l,v_sc_arr_l,~,~] = lambert_mex(r_sc_soi',
          r_t_rv_l',t_flight_l,0,mu_s); % Call to Lambert
          solver
110          delta_v_dep_l = norm(v_sc_dep_l'-v_sc_soi); %[km/s]
          Earth departure delta-v
111          delta_v_arr_l = norm(v_t_rv_l-v_sc_arr_l'); %[km/s]
          Asteroid rendez-vous delta-v
112          delta_v_l = delta_v_0_i+delta_v_dep_l+delta_v_arr_l;
          %[km/s] Total mission delta-v
113          if delta_v_l < delta_v_min(k)
114              delta_v_min(k) = delta_v_l;
115              delta_v_0_opt(k) = delta_v_0_i;
116              alpha_0_opt(k) = rad2deg(alpha_0_j);
117              t_flight_opt(k) = t_flight_l;
118              delta_v_dep_opt(k) = delta_v_dep_l;
119          end
120      end
121      unload_kernels_alt();
122  end
123  end
124  end
125
126  folder = 'C:\Users\Joan\MUEA\SFE\Trajectories\';
127  save (strcat(folder,filename),'t_start','delta_v_min','delta_v_0_opt',
          'alpha_0_opt','t_flight_opt','delta_v_dep_opt');
128
129  figure
130  plot(t_start,delta_v_min);

```

```

131 title(designation);
132 xlabel('UTC launch date [JD]');
133 ylabel('Minimum delta-v [km/s]');
134
135 figure
136 plot(t_start,delta_v_0_opt);
137 title(designation);
138 xlabel('UTC launch date [JD]');
139 ylabel('Optimal launch delta-v [km/s]');
140
141 figure
142 plot(t_start,alpha_0_opt);
143 title(designation);
144 xlabel('UTC launch date [JD]');
145 ylabel('Optimal tangential angle [deg]');
146
147 figure
148 plot(t_start,delta_v_dep_opt);
149 title(designation);
150 xlabel('UTC launch date [JD]');
151 ylabel('Optimal Earth SOI departure delta-v [km/s]');
152
153 figure
154 plot(t_start,t_flight_opt);
155 title(designation);
156 xlabel('UTC launch date [JD]');
157 ylabel('Optimal flight time [days]');
158
159 % Displaying the minimum delta-v orbital transfer
160 [~,h] = min(delta_v_min);
161 delta_v_0_adim_h = delta_v_0_opt(h)/(n_12*a_12);
162 alpha_0_h = deg2rad(alpha_0_opt(h));
163 vx_0_h = delta_v_0_adim_h*cos(theta_L1M);
164 vy_0_h = -delta_v_0_adim_h*sin(theta_L1M)*sin(alpha_0_h);
165 vz_0_h = delta_v_0_adim_h*sin(theta_L1M)*cos(alpha_0_h);
166 C_h = [x_0,y_0,z_0,vx_0_h,vy_0_h,vz_0_h];
167 cv0_h = (1:42)'; % Integration vector
168 cv0_h(1:6) = C_h; % 6-dim state
169 cv0_h = matrixToVector(cv0_h,cr3bp.cst.orbit.STM0,6,6,6); % STM
    concatenation after the 6-dim state
170 [~,~,t_sc_soi_syn_adim_h,cv_soi_syn_adim_h,~] = ode113(@(t,y)
    cr3bp_derivatives_42(t,y,mu),t_span,cv0_h,options);
171 s_sc_soi_syn_adim_h = cv_soi_syn_adim_h(1:6);
172 % [t_sc_soi_syn_h,s_sc_soi_syn_h] = CR3BP_integrator_syn(C_h,cr3bp);
173 t_start_J2000_h = t_start_J2000(h);
174 [t_sc_soi_J2000_h,s_sc_soi_h] = syn2scECLIPJ2000(t_sc_soi_syn_adim_h,
    s_sc_soi_syn_adim_h',cr3bp,t_12,t_start_J2000_h,false,false);
175 % [t_sc_soi_J2000_h,s_sc_soi_h] = framechange(t_sc_soi_syn_h,
    s_sc_soi_syn_h,cr3bp,t_start_J2000_h);
176 r_sc_soi_h = s_sc_soi_h(1:3);
177 t_flight_h = t_flight_opt(h);

```



```

178 t_rv_J2000_h = t_sc_soi_J2000_h+t_flight_h*cst.env.days;
179 eph_target_patch_rv_h = mice_spkezr(SPKID,t_rv_J2000_h, 'ECLIPJ2000', '
    NONE', 'SUN');
180 r_t_rv_h = eph_target_patch_rv_h.state(1:3);
181 [v_sc_dep_h,~,~,~] = lambert_mex(r_sc_soi_h',r_t_rv_h',t_flight_h,0,
    mu_s);
182 s_sc_dep_h(1:3,1) = r_sc_soi_h;
183 s_sc_dep_h(4:6,1) = v_sc_dep_h';
184 [~,a_sc,e_sc,I_sc,o_ap_sc,o_an_sc,~,~,M_sc_dep_h] = cart2kep(
    s_sc_dep_h,mu_s);
185 n_sc = sqrt(mu_s/a_sc^3);
186
187 t_JD = zeros(1,t_flight_h+1);
188 r_t = zeros(t_flight_h+1,3);
189 r_sc = zeros(t_flight_h+1,3);
190 r_earth = zeros(t_flight_h+1,3);
191 r_mars = zeros(t_flight_h+1,3);
192
193 for g = 0:t_flight_h
194     t_J2000_g = t_sc_soi_J2000_h+g*cst.env.days; %[s] Seconds between
        J2000 TDB and current date
195     M_sc = M_sc_dep_h+n_sc*(t_J2000_g-t_sc_soi_J2000_h);
196     s_sc = kep2cart(a_sc,e_sc,I_sc,o_ap_sc,o_an_sc,M_sc,mu_s); %
        Spacecraft state vector
197     eph_target_patch = mice_spkezr(SPKID,t_J2000_g, 'ECLIPJ2000', '
        NONE', 'SUN');
198     eph_earth_patch = mice_spkezr('EARTH', t_J2000_g, 'ECLIPJ2000', '
        NONE', 'SUN');
199     eph_mars_patch = mice_spkezr('MARS BARYCENTER', t_J2000_g, '
        ECLIPJ2000', 'NONE', 'SUN');
200     r_sc(g+1,:) = s_sc(1:3); % Spacecraft position
201     r_t(g+1,:) = eph_target_patch.state(1:3); % Target position
202     r_earth(g+1,:) = eph_earth_patch.state(1:3); % Earth position
203     r_mars(g+1,:) = eph_mars_patch.state(1:3); % Mars position
204 end
205
206 figure
207 hold on
208 scatter3(r_s(1),r_s(2),r_s(3),'yellow','filled');
209 plot3(r_t(:,1),r_t(:,2),r_t(:,3),'black');
210 plot3(r_sc(:,1),r_sc(:,2),r_sc(:,3),'green');
211 plot3(r_earth(:,1),r_earth(:,2),r_earth(:,3),'blue');
212 plot3(r_mars(:,1),r_mars(:,2),r_mars(:,3),'red');
213 axis([-6.0e8 6.0e8 -6.0e8 6.0e8 -6.0e8 6.0e8]);
214 xlabel('km');
215 ylabel('km');
216 zlabel('km');
217 title(strcat('Trajectory towards',{ ' },designation));
218 hold off
219
220 unload_kernels_alt();

```

D.2 Lagrange_solver_adim

```

1 function [LP] = Lagrange_solver_adim(cr3bp)
2
3 mu = cr3bp.mu;
4 mu_1 = 1-mu;
5 mu_2 = mu;
6
7 % dU/dx, adimesionalised
8 fun1 = @(x,y) x-mu_1*(x+mu_2)/(sqrt((x+mu_2)^2+y^2))^3-mu_2*(x-mu_1)/(
    sqrt((x-mu_1)^2+y^2))^3 ;
9 % dU/dy, adimesionalised
10 fun2 = @(x,y) y-(mu_1/(sqrt((x+mu_2)^2+y^2))^3+mu_2/(sqrt((x-mu_1)^2+y
    ^2))^3)*y;
11 % Solver, find the (x,y) points for which the gradient of
12 % U is null (Definition of Lagrange points)
13 fun3 = @(r) [fun1(r(1),r(2)) , fun2(r(1),r(2))];
14 L1 = (fsolve(fun3,[0.5,0])); %[adim] (x,y) position of L1
15 L2 = (fsolve(fun3,[1.5,0])); %[adim] (x,y) position of L2
16 L3 = (fsolve(fun3,[-2,0])); %[adim] (x,y) position of L3
17 L4 = (fsolve(fun3,[0.5,0.5])); %[adim] (x,y) position of L4
18 L5 = (fsolve(fun3,[0.5,-0.5])); %[adim] (x,y) position of L5
19
20 Lx = [L1(1);L2(1);L3(1);L4(1);L5(1)];
21 Ly = [L1(2);L2(2);L3(2);L4(2);L5(2)];
22 Lz = [0;0;0;0;0];
23
24 LP = [Lx,Ly,Lz]; %[adim] Lagrange point position matrix

```

D.3 preliminary_solver

```

1 function [delta_v_dep_opt_prelim_min,t_flight_opt_prelim_min] =
    preliminary_solver(SPKID,designation,t_start,t_start_J2000,x_0,y_0
    ,z_0,cr3bp,t_c,mu_s,plot_bool)
2
3 % Preliminary problem variables
4 t_flight_prelim = (60:1:2190); %[days] Flight time from Earth SOI to
    target
5
6 % Preliminary optimised variables
7 delta_v_min_prelim = 10000*ones(size(t_start)); %[km/s] Minimum total
    delta-v for each start date
8 t_flight_opt_prelim = zeros(size(t_start)); %[days] Optimal flight
    time from Earth SOI to target for each start date
9 delta_v_dep_opt_prelim = zeros(size(t_start)); %[days] Optimal
    departure from Earth SOI delta-v to target for each start date
10
11 % Spacecraft initial state in the synodic frame of reference
12 vx_0 = 0; %[adim] Initial x velocity
13 vy_0 = 0; %[adim] Initial y velocity
14 vz_0 = 0; %[adim] Initial z velocity
15 C=[x_0,y_0,z_0,vx_0,vy_0,vz_0]; %[adim] Initial conditions of state

```

```

    vector (x,y,z,vx,vy,vz)
16 t_i = 0; %[adim] Initial time from start date
17
18 parfor k = 1:size(t_start,2)
19     load_kernels_alt(); % Start the SPICE kernels
20     t_start_k_J2000 = t_start_J2000(k); %[s] Seconds between J2000
        TDB and start date
21 %     [~,s_sc_k] = framechange_adim(t_i,t_c,C,cr3bp,t_start_k_J2000);
22     [~,s_sc_k] = syn2scECLIPJ2000(t_i,C',cr3bp,t_c,t_start_k_J2000,
        false,false);
23     r_sc_k = s_sc_k(1:3); %[km] Position of the spacecraft wrt the
        Sun in ECLIPJ2000 at start date k
24     v_sc_k = s_sc_k(4:6); %[km/s] Velocity of the spacecraft wrt the
        Sun in ECLIPJ2000 at start date k
25     for l = 1:size(t_flight_prelim,2)
26         t_flight_l = t_flight_prelim(l);
27         t_arr_J2000 = t_start_k_J2000+t_flight_l*cr3bp.cst.env.
            days; %[s] Seconds between J2000 TDB and arrival date
28         eph_target_patch_l = mice_spkezr(SPKID,t_arr_J2000, '
            ECLIPJ2000', 'NONE', 'SUN');
29         r_t_l = eph_target_patch_l.state(1:3); % Position of the
            target wrt the Sun in ECLIPJ2000 at arrival date l
30         v_t_l = eph_target_patch_l.state(4:6); % Velocity of the
            target wrt the Sun in ECLIPJ2000 at arrival date l
31         [v_sc_dep,v_sc_arr,~,~] = lambert_mex(r_sc_k',r_t_l',
            t_flight_l,0,mu_s); % Call to Lambert solver
32         delta_v_dep = norm(v_sc_dep'-v_sc_k); %[km/s] Earth
            departure delta-v
33         delta_v_arr = norm(v_t_l-v_sc_arr'); %[km/s] Mars rendez-
            vous delta-v
34         delta_v = delta_v_dep+delta_v_arr; %[km/s] Total mission
            delta-v
35         if delta_v < delta_v_min_prelim(k)
36             delta_v_min_prelim(k) = delta_v;
37             t_flight_opt_prelim(k) = t_flight_l;
38             delta_v_dep_opt_prelim(k) = delta_v_dep;
39         end
40     end
41     unload_kernels_alt();
42 end
43
44 % Preliminary optimal departure delta-v and associated flight time
45 delta_v_dep_opt_prelim_min = min(delta_v_dep_opt_prelim); %[km/s]
    Preliminary optimal departure delta-v
46 delta_v_dep_opt_prelim_min = floor(delta_v_dep_opt_prelim_min/0.1)
    *0.1; % rounding down
47 t_flight_opt_prelim_min = min(t_flight_opt_prelim); %[days]
    Preliminary optimal flight time
48
49 if plot_bool == true
50     % Preliminary minimum total mission delta-v plot

```

```

51     figure
52     plot(t_start,delta_v_min_prelim);
53     title(designation);
54     xlabel('Launch date [JD]');
55     ylabel('Minimum delta-v [km/s]');
56
57     % Preliminary minimum departure delta-v plot
58     figure
59     plot(t_start,delta_v_dep_opt_prelim);
60     title(designation);
61     xlabel('Launch date [JD]');
62     ylabel('Minimum departure delta-v [km/s]');
63
64     % Preliminary optimal flight time plot
65     figure
66     plot(t_start,t_flight_opt_prelim);
67     title(designation);
68     xlabel('Launch date [JD]');
69     ylabel('Flight time [days]');
70 end

```

D.4 odezero_EARTHSOI

```

1 function [value, isterminal, direction] = odezero_EARTHSOI(T,Y)
2
3 % Integration stop conditions for an escape trajectory from the Earth
4 % -Moon
5 % CR3BP system
6
7 ms = 1.98841695225459e30; %[kg] Sun mass
8 me = 5.97219e24; %[kg] Earth mass
9 mm = 7.34581412062866e22; %[kg] Moon mass
10
11 mu = mm/(me+mm);
12 mu_1 = 1-mu;
13 mu_2 = mu;
14
15 a_em = 384400; %[km] Earth-Moon semi-major axis
16 a_se = 149597871; %[km] Sun-Earth semi-major axis
17
18 R_1 = 6378.14/a_em; %[adim] Earth equatorial radius
19 R_2 = 1737.5/a_em; %[adim] Moon equatorial radius
20
21 P_1 = [-mu_2,0,0]; %[adim] Position of the Earth
22 P_2 = [mu_1,0,0]; %[adim] Position of the Moon
23
24 R_SOI = a_se/a_em*((me/ms)^(2/5)); %[adim] Earth SOI radius
25
26 value = [sqrt((Y(1)-P_2(1))^2+(Y(2)-P_2(2))^2+(Y(3)-P_2(3))^2)<
27         R_2; % Spacecraft crashes against the Moon
28         sqrt((Y(1)-P_1(1))^2+(Y(2)-P_1(2))^2+(Y(3)-P_2(3))^2)<
29         R_1; % Spacecraft crashes against the Earth

```

```

27         sqrt((Y(1)-P_1(1))^2+(Y(2)-P_1(2))^2+(Y(3)-P_2(3))^2)>
           R_SOI]; % Spacecraft leaves the Earth's SOI
28
29 isterminal = [1;1;1]; % Stop the integration
30 direction = [0;0;0];
31
32 end

```

D.5 syn2scECLIPJ2000

```

1 function [t_J2000, y_J2000_sun] = syn2scECLIPJ2000(t_syn, y_syn,
    cr3bp, T_adim, start, bool_J2000, bool_eci)
2 %SYN2J2000 Change of coordinates from adimensionnal synodic frame to
    heliocentric ecliptic J2000
3 %
4 %% Time
5 t_syn_dim = Dimensionalisation_T(t_syn, T_adim);
6 %Time mesured wrt a certain epoch 'start' and translated into
    ephemeris
7 %time
8 t_J2000 = t_syn_dim + start;
9
10 %% Construction of the instantaneous rotating frame
11 %init plot
12 if bool_J2000==true
13     figure
14     scatter3(0, 0,0,'g','o')
15     hold on
16 end
17
18 %Init variables
19 y_syn_dim = ones(6, size(y_syn, 2));
20 y_J2000_sun = ones(6, size(y_syn, 2));
21
22 %Conversion loop on all patch points
23 for i = 1:size(y_syn, 2)
24 %Compute ephemerides of Earth, Moon, and Earth-Moon Barycenter (EMB)
25 eph_date = t_J2000(i);
26 eph_moon_patch = mice_spekr('MOON', eph_date, 'ECLIPJ2000', 'NONE',
    'EARTH');
27 eph_bem_patch = mice_spekr('Earth-Moon barycenter', eph_date, '
    ECLIPJ2000', 'NONE', 'SUN');
28 X_moon = eph_moon_patch.state(1:6);
29 pos_eph_bem_patch = eph_bem_patch.state(1:3);
30 v_eph_bem_patch = eph_bem_patch.state(4:6);
31
32 %Locally dimensionalize synodic state
33 % y_syn_dim(1:3,i) = y_syn(1:3,i)*norm(X_moon(1:3));
34 % y_syn_dim(4:6,i) = y_syn(4:6,i)*norm(X_moon(1:3))/T_adim;
35 y_syn_dim(:,i) = Dimensionalisation_X(y_syn(:,i), norm(X_moon(1:3)),
    T_adim);
36

```

```

37 %Build rotating to inertial position transition matrix
38 etest1 = X_moon(1:3)/norm(X_moon(1:3));
39 etest3 = cross(X_moon(1:3),X_moon(4:6))/norm(cross(X_moon(1:3),X_moon
    (4:6)));
40 etest2 = cross(etest3,etest1)/norm(cross(etest3,etest1));
41 T_test = [etest1, etest2, etest3];
42
43 %Apply rotation matrix to positions and change origin from EMB to Sun
44 y_J2000_sun(1:3,i) = T_test*y_syn_dim(1:3,i) + pos_eph_bem_patch;
45
46 %Transition velocities
47 thetadot_inst = norm(cross(eph_moon_patch.state(1:3), eph_moon_patch.
    state(4:6))) / (norm(eph_moon_patch.state(1:3)))^2;
48 Tv = [[thetadot_inst*T_test(1,2) -thetadot_inst*T_test(1,1) 0 T_test
    (1,1) T_test(1,2) T_test(1,3)]; [thetadot_inst*T_test(2,2) -
    thetadot_inst*T_test(2,1) 0 T_test(2,1) T_test(2,2) T_test(2,3)];
    [thetadot_inst*T_test(3,2) -thetadot_inst*T_test(3,1) 0 T_test
    (3,1) T_test(3,2) T_test(3,3)]];
49 y_J2000_sun(4:6,i) = Tv*y_syn_dim(:,i) + v_eph_bem_patch;
50
51 %Plotting
52 if bool_J2000==true
53     scatter3(X_moon(1), X_moon(2),X_moon(3), 'b', 'o')
54     hold on
55 end
56
57 end
58
59 %% Plot eci comparison
60 if bool_eci==true
61     for i = 1:size(y_syn,2)
62         yeci = cr3bp.L*syn2eci(y_syn(:,i),t_syn(:,i),cr3bp);
63         yeci(4:6) = yeci(4:6)/cr3bp.T*2*pi;
64         yeci_moon = cr3bp.L*syn2eci([1-cr3bp.mu, 0, 0, 0, 0, 0]',
            t_syn(:,i),cr3bp);
65         scatter3(yeci(1),yeci(2),yeci(3), 'm', 'x')
66         hold on
67         scatter3(yeci_moon(1),yeci_moon(2),yeci_moon(3), 'b', 'o')
68         hold on
69     end
70 end
71
72 %% Plot J2000 conversion
73 if bool_J2000==true
74     scatter3(y_J2000_sun(1,:), y_J2000_sun(2,:),y_J2000_sun(3,:), 'r',
        'x')
75     hold off
76 end
77
78 end

```

D.6 load_kernels

```
1 function [params] = load_kernels(params)
2 % Loads all necessary spice Kernels
3
4 if (params.ephemerides.isLoaded == false)
5     cspice_furnsh('C:\Users\JOAN\MUEA\SFE\semat-eb\mice_kernels\
6         de438s.bsp');
7     %cspice_furnsh('C:\Users\JOAN\MUEA\SFE\semat-eb\mice_kernels\
8         de421.bsp');
9     %cspice_furnsh('C:\Users\JOAN\MUEA\SFE\semat-eb\mice_kernels\
10        de405.bsp');
11    cspice_furnsh('C:\Users\JOAN\MUEA\SFE\semat-eb\mice_kernels\
12        naif0012.tls.pc');
13    cspice_furnsh('C:\Users\JOAN\MUEA\SFE\semat-eb\mice_kernels\de
14        -403-masses.tpc');
15    cspice_furnsh('C:\Users\JOAN\MUEA\SFE\semat-eb\mice_kernels\
16        wld86210.15');
17    cspice_furnsh('C:\Users\JOAN\MUEA\SFE\semat-eb\mice_kernels\
18        wld1156302.15');
19    params.ephemerides.isLoaded = true;
20 end
21 end
```

D.7 load_kernels_alt

```
1 function [] = load_kernels_alt()
2 % Loads all necessary spice Kernels
3
4 cspice_furnsh('C:\Users\JOAN\MUEA\SFE\semat-eb\mice_kernels\de438s.
5     bsp');
6 %cspice_furnsh('C:\Users\JOAN\MUEA\SFE\semat-eb\mice_kernels\de421.
7     bsp');
8 %cspice_furnsh('C:\Users\JOAN\MUEA\SFE\semat-eb\mice_kernels\de405.
9     bsp');
10 cspice_furnsh('C:\Users\JOAN\MUEA\SFE\semat-eb\mice_kernels\naif0012.
11     tls.pc');
12 cspice_furnsh('C:\Users\JOAN\MUEA\SFE\semat-eb\mice_kernels\de-403-
13     masses.tpc');
14 cspice_furnsh('C:\Users\JOAN\MUEA\SFE\semat-eb\mice_kernels\wld86210
15     .15');
16 cspice_furnsh('C:\Users\JOAN\MUEA\SFE\semat-eb\mice_kernels\
17     wld1156302.15');
18
19 end
```

D.8 unload_kernels_alt

```
1 function [] = unload_kernels_alt()
2 %UNLOAD_KERNELS Unloads all spice kernels
3
4     cspice_kclear();
```

5

6

7 **end**